UCSF
UC San Francisco Previously Published Works

## Title

Increased CSF drainage by non-invasive manipulation of cervical lymphatics

## Permalink

https://escholarship.org/uc/item/8dz9j27t

## Journal

Nature, 643(8072)

## ISSN

0028-0836

## Authors

Jin, Hokyung
Yoon, Jin-Hui
Hong, Seon Pyo
et al.

## Publication Date

2025-07-17

## DOI

10.1038/s41586-025-09052-5

## Copyright Information

This work is made available under the terms of a Creative Commons Attribution License, available at https://creativecommons.org/licenses/by/4.0/

Peer reviewed

eScholarship.org Powered by the California Digital Library
University of California

Article

# Increased CSF drainage by non-invasive manipulation of cervical lymphatics

https://doi.org/10.1038/s41586-025-09052-5

Received: 24 September 2024

Accepted: 22 April 2025

Published online: 04 June 2025

Open access

Check for updates

Hokyung Jin[1,2,9], Jin-Hui Yoon[1,9], Seon Pyo Hong[1,9], Yu Seok Hwang[3], Myung Jin Yang[1], Jieun Choi[2], Hae Jin Kang[1], Seung Eun Baek[1], Cheolhwa Jin[1,2], Junho Jung[1], Hae Jin Kim[4], Jincheol Seo[5], Jinyoung Won[5], Kyung Seob Lim[6], Chang-Yeop Jeon[5], Youngjeon Lee[5,7], Michael J. Davis[4], Hyung-Soon Park[3], Donald M. McDonald[8] & Gou Young Koh[1,2]✉

Cerebrospinal fluid (CSF) in the subarachnoid space around the brain drains to lymph nodes in the neck, but the connections and regulation have been challenging to identify[1–24]. Here we used fluorescent tracers in *Prox1*–GFP lymphatic reporter mice to map the pathway of CSF outflow through lymphatics to superficial cervical lymph nodes. CSF entered initial lymphatics in the meninges at the skull base and continued through extracranial periorbital, olfactory, nasopharyngeal and hard palate lymphatics, and then through smooth muscle-covered superficial cervical lymphatics to submandibular lymph nodes. Tracer studies in adult mice revealed that a substantial amount of total CSF outflow to the neck drained to superficial cervical lymph nodes. However, aged mice had fewer lymphatics in the nasal mucosa and hard palate and reduced CSF outflow to cervical lymph nodes. Superficial cervical lymphatics in aged mice had increased endothelial cell expression of *Nos3*, encoding endothelial nitric oxide synthase (eNOS), but had less eNOS protein and impaired nitric oxide signalling. Manipulation of superficial cervical lymphatics through intact skin by a force-regulated mechanical device doubled CSF outflow and corrected drainage impairment in aged mice. This manipulation increased CSF outflow by compressing superficial cervical lymphatics while having little effect on their normal spontaneous contractions. Overall, the findings highlight the importance of superficial cervical lymphatics for CSF outflow and the potential for reversing CSF drainage impairment by non-invasive mechanical stimulation.

CSF provides mechanical protection and clears neurotransmitters, metabolites, and amyloid-β, tau and other protein aggregates from the central nervous system[17,19,24]. Claims that diminished secretion or impaired clearance of CSF can contribute to impaired brain function in ageing, Alzheimer disease or other neurodegenerative disorders have promoted interest in gaining a better understanding of factors that regulate CSF outflow[12,25–28], but the underlying pathophysiology and potential approaches for ameliorating these conditions by manipulating CSF drainage[29,30] are at an early stage of understanding.

After the landmark study by Key and Retzius in 1875 (ref. 1), CSF drainage from meningeal lymphatics to lymphatics and lymph nodes in the head and neck was then confirmed in many subsequent studies[2–11,13–18,21,31] by using diverse approaches including injection of carbon particles, Microfil silicone rubber, dyes or other substances into the subarachnoid space (SAS) and then observing the tracers in nasal lymphatics and cervical lymph nodes[4,5,7,8]. Recent studies using *Prox1*–GFP mice[32], immunohistochemistry, confocal microscopy and magnetic resonance imaging have further characterized the connections between the SAS and lymphatics in the dura around the olfactory bulb, cribriform plate, nasal mucosa and nasopharynx[14,20–23].

Findings that CSF clearance can be manipulated by expanding or reducing meningeal lymphatic networks have raised new therapeutic possibilities[15,25,26,29,30,33]. Through vascular endothelial growth factor-C (VEGF-C)–vascular endothelial growth factor receptor 3 (VEGFR3) signalling modulation[15,29,30] or photodynamic destruction[25,26], studies have shown that increasing CSF clearance can reduce the severity of ischaemic or traumatic stroke and other neurological conditions, including migraines[34,35]. Beyond the therapeutic applications, questions remain about how CSF crosses the arachnoid barrier to reach dural lymphatics. Although openings have been reported near olfactory nerves and the cribriform plate[22,23] and along bridging veins near dural venous sinuses[36], further work is needed to understand the cellular nature of these openings and how different conditions affect drainage routes.

In a previous study, we identified the pathway of CSF clearance from the SAS through dural lymphatics to deep cervical lymph nodes[23]. This pathway, through the nasopharyngeal lymphatic plexus to deep

[1]Center for Vascular Research, Institute for Basic Science, Daejeon, Republic of Korea. [2]Graduate School of Medical Science and Engineering, Korea Advanced Institute of Science and Technology, Daejeon, Republic of Korea. [3]Department of Mechanical Engineering, Korea Advanced Institute of Science and Technology, Daejeon, Republic of Korea. [4]Department of Medical Pharmacology and Physiology, University of Missouri, Columbia, MO, USA. [5]National Primate Research Center, Korea Research Institute of Bioscience and Biotechnology (KRIBB), Cheongju, Republic of Korea. [6]Futuristic Animal Resource & Research Center, Korea Research Institute of Bioscience and Biotechnology, Cheongju, Republic of Korea. [7]KRIBB School of Bioscience, Korea National University of Science and Technology, Daejeon, Republic of Korea. [8]Department of Anatomy, Cardiovascular Research Institute and Helen Diller Family Comprehensive Cancer Center, University of California, San Francisco, San Francisco, CA, USA. [9]These authors contributed equally: Hokyung Jin, Jin-Hui Yoon, Seon Pyo Hong. ✉e-mail: gykoh@kaist.ac.kr

cervical lymph nodes, carried about half of the CSF outflow to the neck[23]. With the goal of developing approaches for increasing CSF outflow, we found that local pharmacological manipulation of the lymphatics promoted greater CSF outflow[23]. However, a limitation was that surgical exposure was required to access these lymphatics located deep in the neck, which were inaccessible to non-invasive approaches for increasing CSF transport by mechanical manipulation through the skin.

To address this limitation, in the present study, we found that superficial cervical lymphatics (scLVs) were responsive to non-invasive manipulation. By using fluorescent CSF tracers in *Prox1*–GFP lymphatic reporter mice and in monkeys, we learned that CSF in the SAS drained through scLVs to submandibular lymph nodes after passing through meningeal lymphatics in the frontal and basal region of the skull to extracranial periorbital, nasal and hard palate lymphatics. We then learned that the contractile apparatus of the collecting lymphatics of the scLV pathway remained normal in aged mice, despite the atrophy of upstream lymphatics and impaired CSF outflow. To take advantage of the location and intact contractility of the scLV pathway, we developed a non-invasive approach for correcting the impairment in aged mice by increasing CSF outflow with a force-regulated mechanical stimulator on the intact skin. Experiments with aged mice revealed that the approach largely normalized CSF outflow through scLVs to lymph nodes.

## CSF outflow via scLVs

In the neck of mice, scLVs drain to the submandibular, accessory submandibular and parotid lymph nodes, and deep cervical lymphatics (dcLV) drain to the deep cervical lymph node (Fig. 1a,b). Examination of 77 *Prox1*–GFP mice revealed that the three superficial cervical lymph nodes were consistently present, but the accessory submandibular lymph node had variable locations in relation to the others, as reflected by the classification of type 1 (61.0%; accessory combined with submandibular), type 2 (31.2%; accessory separate from other nodes) or type 3 (7.8%; accessory combined with parotid; Extended Data Fig. 1a–c).

To determine which of these lymph nodes received CSF drainage, we infused 1 µl of 10 kDa tetramethylrhodamine-conjugated dextran (TMR–dextran) in PBS over 1 min into the SAS at the cisterna magna of anaesthetized *Prox1*–GFP mice (Fig. 2a). TMR–dextran fluorescence was examined and measured in scLVs at 30 min and 60 min (Fig. 2b–e) and in the superficial cervical lymph nodes at 15–120 min (Fig. 2f,g). TMR–dextran fluorescence was strong in the submandibular, accessory submandibular and deep cervical lymph nodes and had an unambiguous pattern in types 1 and 2 lymph nodes. No tracer was visible in parotid lymph nodes (Fig. 2f), except in the type 3 group, where the tracer was detected in the accessory submandibular lymph node and the adjacent rostral region of the parotid lymph node at 30 min after intracisternal tracer infusion (Extended Data Fig. 1d–f), indicative of functional coupling of the fused lymph nodes.

The amount of TMR–dextran fluorescence in the submandibular and accessory submandibular lymph nodes combined (53%) was similar to the amount in the deep cervical lymph node (47%), when expressed as the proportion of total fluorescence in these nodes over the period of 15–120 min after intracisternal infusion (Fig. 2g). The measurements revealed that superficial cervical and deep cervical lymph nodes each received about half of the CSF drainage to lymph nodes in the neck of mice.

The amount of CSF drainage to individual cervical lymph nodes changed with the conditions. Ligation of dcLV shifted the drainage from deep to superficial cervical lymph nodes, as reflected by reduction in CSF tracer in the deep node and increase in the accessory submandibular lymph node (Extended Data Fig. 2a–d). By comparison, ligation of scLVs reduced overall CSF drainage to all cervical lymph nodes by only approximately 35%. This modest reduction was the result of a large decrease in CSF drainage to submandibular lymph nodes, but no change in drainage to the accessory submandibular and deep cervical lymph nodes (Extended Data Fig. 2e–h). This was explained by the latter lymph nodes receiving CSF mainly through the nasopharyngeal lymphatic route (Fig. 1b). These effects illustrated the potential for maintaining CSF drainage by increasing outflow through a lymphatic route after obstruction of another route, but the differences showed the importance of selective targeting of the manipulations.

To determine whether CSF drainage to cervical lymph nodes of mice was similar in primates, we infused 2.5 ml of fluorescent 0.5-µm beads (FluoSpheres) in PBS over 10 min into the SAS at the cisterna magna of anaesthetized *Macaca fascicularis* monkeys (Extended Data Fig. 3a). At 180 min, FluoSpheres were abundant in submandibular and retropharyngeal (deep cervical lymph node in mice) lymph nodes, but not in the parotid lymph node (Extended Data Fig. 3b and Supplementary Fig. 1a). FluoSpheres were also abundant near the greater palatine and incisive foramina in the hard palate (Extended Data Fig. 3c and Supplementary Fig. 1b,c).

Submandibular lymph nodes had three afferent lymphatic trunk vessels, designated scLV vessels scLV-1, scLV-2 and scLV-3, in two-thirds of male and female mice (Fig. 2b,d, Supplementary Fig. 2 and Supplementary Video 1). A fourth afferent lymphatic, scLV-4, was found in one-third of the mice. The diameter and length of the lymphatic segment between valves (lymphangion) of scLV-1 and scLV-2 were similarly variable and lacked sex differences (Supplementary Fig. 3a,b).

scLV-1 and scLV-2 had a dense but uneven layer of circular smooth muscle cells that stained for α-smooth muscle actin ($\alpha SMA^{+}$) along their entire length (Supplementary Fig. 3c,d). Smooth muscle coverage was greater in the middle of lymphangions than near the valves in both sexes (Supplementary Fig. 3e). These features of the lymphatics match the features of contractile lymphangions ('lymphangion pumps') that propel CSF outflow unidirectionally[37,38].

TMR–dextran was visible in scLV-1, but rarely in scLV-2, at 30 min after the intracisternal infusion and was visible in both lymphatics at 60 min but was not detected in scLV-3 at either time (Fig. 2b–e). However, when Alexa-647-conjugated ovalbumin was infused into the floor of the mouth while TMR–dextran was infused intracisternally (Supplementary Fig. 4a), strong Alexa-647-conjugated ovalbumin fluorescence was detected in scLV-3 and in the upper portion of the submandibular lymph node (Supplementary Fig. 4b–d). At 60 min after intracisternal infusion, TMR–dextran was found in a branch from the nasopharyngeal lymphatic plexus[23] that drained to the accessory submandibular lymph node (Extended Data Fig. 4). All superficial cervical lymph nodes drained into common efferent lymphatics (Extended Data Fig. 4e).

Together, these observations revealed that the submandibular lymph node received CSF drainage through scLV-1 and scLV-2 but not through scLV-3, which received lymph from the floor of the mouth. By contrast, the accessory submandibular lymph node received CSF drainage from the nasopharyngeal lymphatic plexus (Extended Data Fig. 4e). On the basis of these findings, we focused our attention on scLV-1 and scLV-2 in subsequent studies.

Physiological properties of scLV-1 and scLV-2 were assessed in vivo and ex vivo (Supplementary Figs. 5 and 6), as previously described[39–41]. Similar spontaneous contractions were found in scLV-1 and scLV-2 in anaesthetized adult mice of both sexes (Supplementary Fig. 5b,c), consistent with a recent report[42]. After isolation, scLV-1 and scLV-2 actively contracted ex vivo in response to pressures ranging from 0.5 to 10 $cmH_2O$ (Supplementary Fig. 6), as reported for other lymphatics in mice[39].

## Upstream connections of the scLV

The upstream connections of scLV-1 and scLV-2 were identified by infusing TMR–dextran, FluoSpheres or Qdots into the SAS at the cisterna magna of *Prox1*–GFP mice and then examining the distribution of the tracer in dural lymphatics (intracranial) and head and neck lymphatics

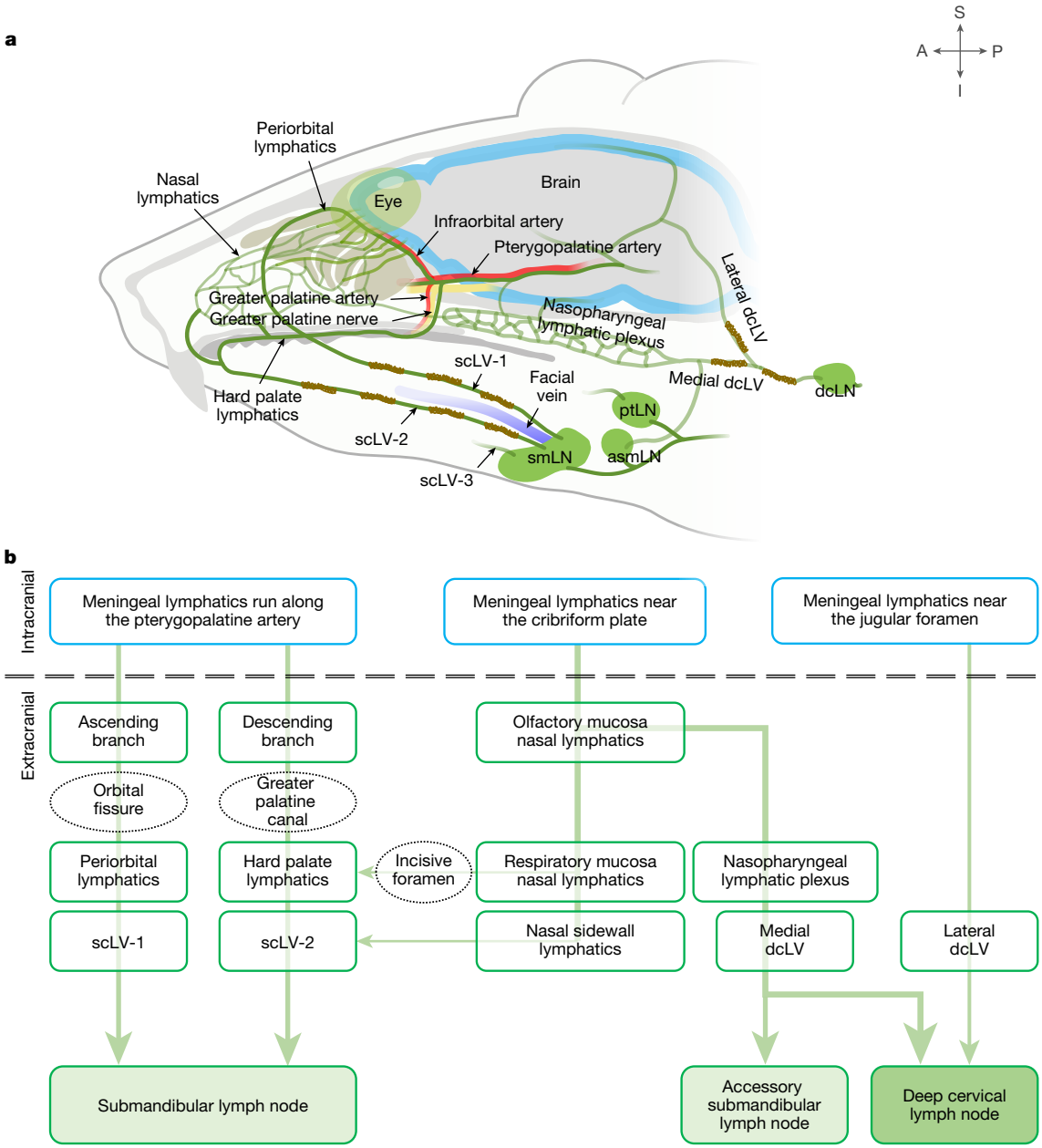


**Fig. 1 | Overview of CSF drainage from meningeal lymphatics to cervical lymphatics and lymph nodes. a**,**b**, Drawing (**a**) and flow chart (**b**) illustrating the complex lymphatic system for CSF drainage from meningeal lymphatics through multiple lymphatic pathways to superficial and deep cervical lymph nodes. (1) Meningeal lymphatics that run along the pterygopalatine and infraorbital arteries traverse the orbital fissure to join periorbital lymphatics that carry CSF through scLV-1 to the submandibular lymph node (smLN). (2) Some meningeal lymphatics that run along the pterygopalatine artery, greater palatine artery and greater palatine nerve traverse the greater palatine canal to join the hard palate lymphatic plexus en route to scLV-2 that drains CSF to the smLN. (3) Meningeal lymphatics near the olfactory bulb traverse the cribriform plate and join lymphatics in the nasal mucosa and nasal sidewall that carry CSF to scLV-2 en route to the smLN. Alternatively, nasal lymphatics traverse the incisive foramen to join the hard palate lymphatic plexus en route to scLV-2 and the smLN. (4) Other meningeal lymphatics near the olfactory bulb traverse the cribriform plate and join nasal lymphatics connected to the nasopharyngeal lymphatic plexus that carries CSF to medial dcLV en route to the accessory submandibular (asmLN) or deep cervical lymph node (dcLN). (5) Meningeal lymphatics at the base of the skull that traverse the jugular foramen join lateral dcLV en route to the dcLN. (6) The parotid lymph node (ptLN) does not receive CSF drainage. Anatomical positions are indicated in the top right corner. A, anterior; I, inferior; P, posterior; S, superior.

(extracranial) at 20, 30 or 60 min (Fig. 3, Extended Data Figs. 5–7 and Supplementary Figs. 7 and 8). Tracer-containing lymphatics upstream to scLV-1 included the ascending branch of dural lymphatics that ran along the pterygopalatine artery intracranially and joined extracranial periorbital lymphatics (Fig. 3a–e and Extended Data Figs. 5e and 6a–c). Two networks of dural lymphatics were upstream to scLV-2. One network was near the olfactory bulb, traversed the cribriform plate and joined extracranial lymphatics of the olfactory mucosa and nasal side wall[23] (Fig. 3f,g, Extended Data Fig. 6a,d–j and Supplementary Fig. 7). The other network accompanied the pterygopalatine artery and joined the descending branch of meningeal lymphatics that ran along the greater palatine artery and greater palatine nerve (Extended Data Figs. 5 and 6b,c). Part of the nasal lymphatics transverses the incisive foramen and joined extracranial lymphatics in the hard palate, without connections to lymphatics in the soft palate (Fig. 1a,b, Extended Data Figs. 5 and 7 and Supplementary Fig. 8).

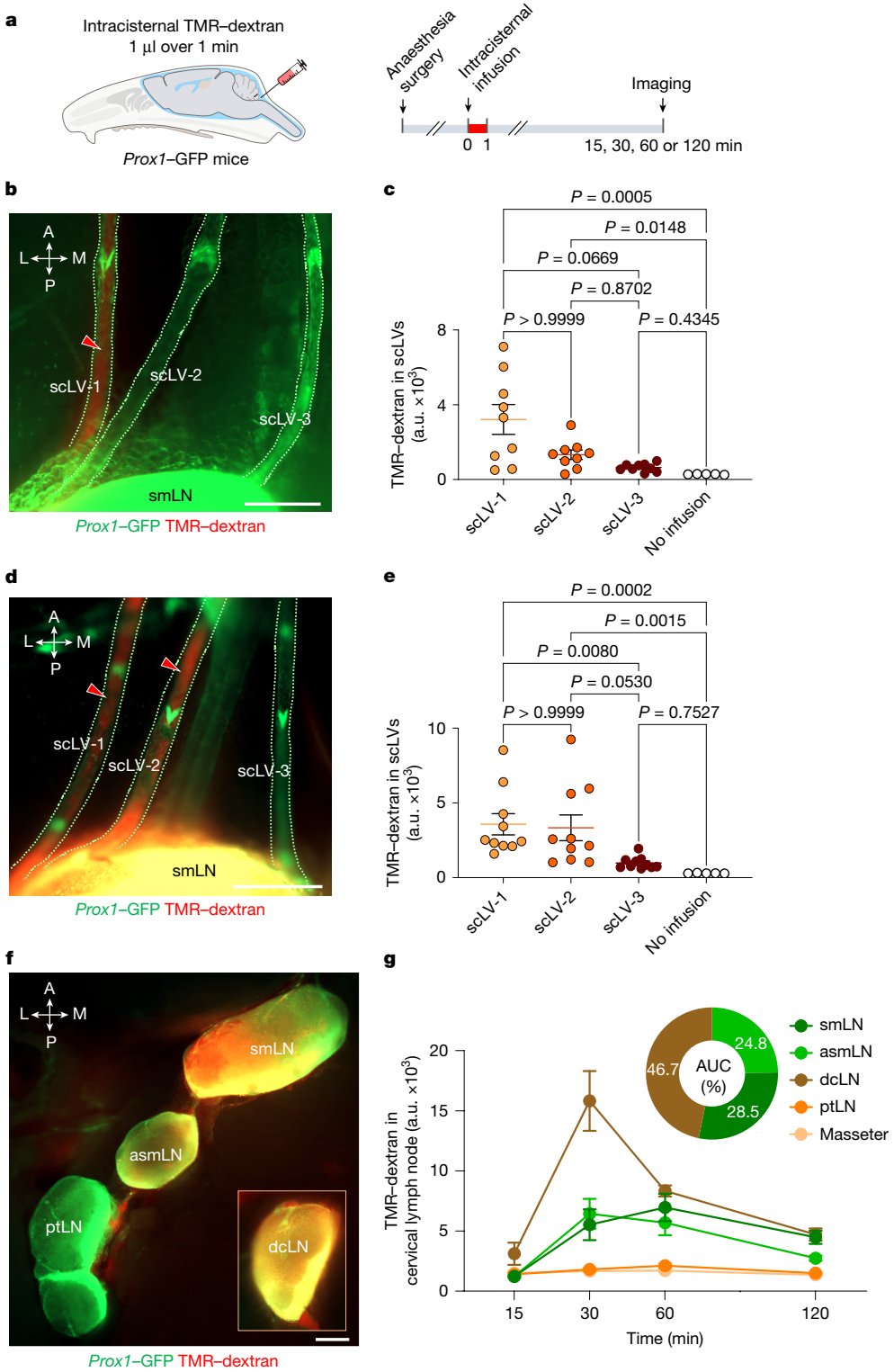


**Fig. 2 | TMR–dextran distribution in scLVs and lymph nodes after intracisternal infusion. a**, Sequence of intracisternal infusion of 1.0 µl TMR–dextran over 1 min into *Prox1*–GFP mice followed 15, 30, 60 or 120 min later by measurement of TMR–dextran fluorescence in scLVs and draining lymph nodes. **b**–**e**, Images (**b**,**d**) and measurements (**c**,**e**) of TMR–dextran fluorescence in three scLVs that join the smLN. At 30 min after intracisternal infusion, TMR–dextran fluorescence (red arrowheads) is strong in scLV-1 (**b**), but at 60 min is strong in scLV-1 and scLV-2 (**d**), yet is essentially absent in scLV-3 at either time point (**b**,**d**); measurements support these findings (**c**,**e**). Scale bars, 200 µm. Each dot represents one mouse ($n = 5$ for no infusion, $n = 9$ for scLV-1, scLV-2 or scLV-3 at 30 min and $n = 10$ for scLV-1, scLV-2 or scLV-3 at 60 min) from three independent experiments. The error bars indicate mean ± s.e.m. *P* values were calculated by Kruskal–Wallis test followed by two-tailed Dunn's multiple comparison post-hoc test. a.u., arbitrary unit. **f**,**g**, Images (**f**) and measurements (**g**) of temporal changes of TMR–dextran fluorescence in type 1 and type 2 superficial cervical lymph nodes, the dcLN (inset) and the masseter muscle. TMR–dextran fluorescence (red) is strong in all lymph nodes but is not evident in the ptLN (**f**). Scale bar, 500 µm. The curves show the tracer fluorescence intensity at the four time points. Each dot is the mean value for $n = 4$–12 mice per group from three independent experiments. The pie chart compares the amounts of tracer fluorescence in the smLN, asmLN and dcLN expressed as the percent of their area under the time-course curve (AUC; **g**). The error bars indicate mean ± s.e.m. Anatomical positions are indicated in the top left corner. L, lateral; M, medial.

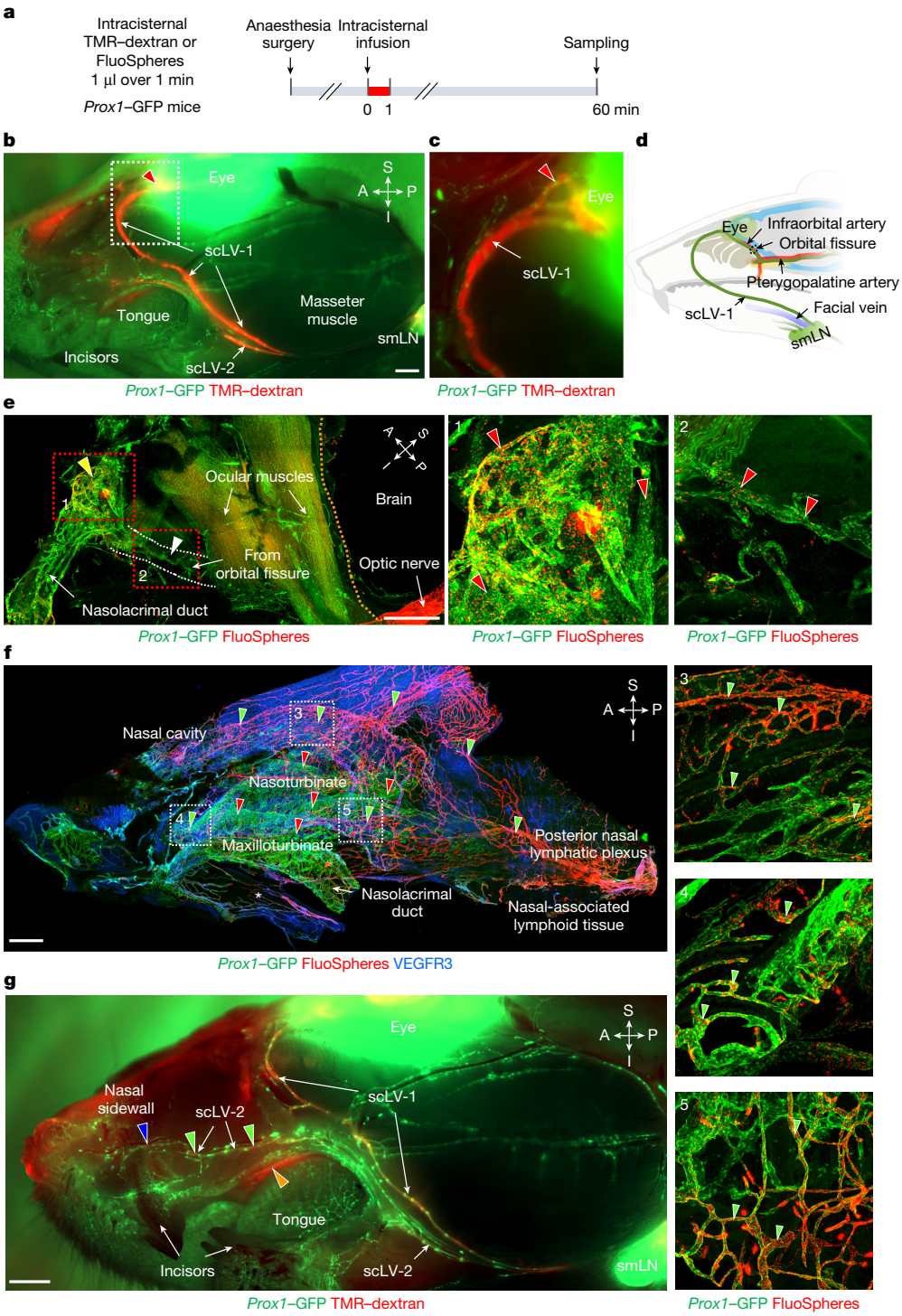


**Fig. 3 | CSF drainage through periorbital, nasal and hard palate lymphatics to the submandibular lymph node. a**, Sequence of intracisternal infusion of 1.0 µl TMR–dextran or FluoSpheres over 1 min into *Prox1*–GFP mice with analysis at 60 min. **b**,**c**, Fluorescence images of TMR–dextran (red) in head and neck lymphatics after removal of facial skin. The TMR–dextran signal is strong in scLV-1, scLV-2 and the periorbital region (red arrowhead). The white dashed line box marks the region enlarged in panel **c**. Scale bar, 1 mm. Representative of $n = 4$ mice from three independent experiments. **d**, Drawing showing the CSF drainage route from meningeal lymphatics near the orbit to the submandibular lymph node. **e**, Immunofluorescence images of FluoSpheres in periorbital (yellow arrowhead) and orbital fissure (white arrowhead) lymphatics. The white dashed lines indicate the lymphatic pathway from the orbital fissure. The orange dashed line marks the intracranial–extracranial boundary. The red dashed line boxes mark regions enlarged in panels showing that FluoSpheres (red) are abundant in periorbital (panel 1) and orbital fissure (panel 2) lymphatics (red arrowheads). Scale bar, 1 mm. Representative of $n = 4$ mice from three independent experiments. **f**, Immunofluorescence images of FluoSpheres in nasal lymphatics at 60 min after intracisternal infusion. In the nasal mucosa, FluoSpheres (red) are abundant in lymphatics (green arrowheads) but not in venous sinusoids (red arrowheads; also PROX1$^+$). The white boxes in panel **f** are enlarged in panels 3–5. The white asterisk in panel **f** marks the junction of the nasal mucosa and hard palate. Scale bar, 500 µm. Representative of $n = 5$ mice from three independent experiments. **g**, Fluorescence image showing TMR–dextran (red) in nasal sidewall lymphatics (blue arrowhead), hard palate (orange arrowhead), and scLV-1 and scLV-2 (green arrowheads). Scale bar, 1 mm. Representative of $n = 4$ mice from three independent experiments. Anatomical positions are indicated in the top right corner.

Lymphatics of the hard palate plexus upstream to scLV-2 had short lymphangions, a mixture of typical semilunar valves and atypical irregularly shaped valves that stained for *Prox1*–GFP and laminin-α5, but they had no smooth muscle coverage (Supplementary Fig. 9). These features resemble lymphatics of the nasopharyngeal lymphatic plexus[23] and differ both from initial lymphatics, which have oak leaf-shaped endothelial cells, and from collecting lymphatics, which have semilunar valves, longer lymphangions and smooth muscle coverage.

FluoSpheres infused into the SAS of monkeys revealed CSF drainage routes through lymphatics like those in mice (Extended Data Fig. 3 and Supplementary Fig. 1). Similarly, indocyanine green infused into the SAS of monkeys revealed CSF drainage routes through lymphatics in the periorbital, nasal sidewall, hard palatal and superficial cervical regions of the face and neck (Fig. 4), similar to those shown by TMR–dextran or FluoSphere infusion in mice.

To determine whether the lymphatics upstream to the superficial cervical lymph node can be expanded, mouse *Vegfc* (m*Vegfc*) was overexpressed in *Prox1*–GFP mice by intracisternal delivery of $1 \times 10^{13}$ gene copies of adeno-associated virus serotype 9 encoding mVEGF-C–mCherry (AAV9–mVEGF-C–mCherry) or control AAV9–mCherry (Supplementary Fig. 10a). Four weeks after viral delivery, mCherry fluorescence reflecting mVEGF-C expression was present around lymphatics of the nasal cavity, hard palate and transverse sinus, but not around the scLVs (Supplementary Fig. 10b,c). In the AAV9–mVEGF-C–mCherry group, lymphatics were expanded in the nasal mucosa (1.30-fold), inferior nasal mucosa (1.56-fold), hard palate (1.42-fold) and along the transverse sinus of dorsal meninges (4.57-fold) over corresponding regions in the AAV9–mCherry control group, but no change was found in the scLVs (Supplementary Fig. 10). These findings indicate that lymphatics upstream to the superficial cervical lymph node can be expanded by activating VEGF-C–VEGFR3 signalling, but scLV trunks do not change under these conditions.

As the parotid lymph node did not receive drainage from the SAS, we determined the afferent drainage routes by infusing TMR–dextran into the facial dermis (0.5 µl over 1 min) of anaesthetized *Prox1*–GFP mice (Fig. 1a,b and Supplementary Fig. 11a,b). At 15 min after injection into each of three facial compartments, TMR–dextran fluorescence was found in the parotid lymph node, but not in the submandibular or accessory submandibular lymph node (Supplementary Fig. 11c–e). These findings provide evidence that the parotid lymph node receives lymph from facial skin and not from the SAS.

## Ageing reduces CSF drainage via the scLV

CSF outflow through lymphatics decreases with age[20,23,43,44]. The reduction in CSF drainage to deep cervical lymph nodes has been documented in multiple studies of aged mice[14,16,20,23,25]. In the present study, we found that TMR–dextran fluorescence in the submandibular lymph node at 60 min after infusion into the SAS was approximately 30% less in aged mice (80–95 weeks) than in younger adults (8–12 weeks; Supplementary Fig. 12).

To learn the reason for the reduction in aged mice, we compared the abundance and size of lymphatics in the scLV pathway of aged mice to younger adults. The extent (area) of the VEGFR3$^+$ lymphatic network upstream to scLV-2 of aged mice was approximately 80% less in the nasal mucosa and 9–17% less in the hard palate plexus than in younger adults (Fig. 5). Lymphatics in the nasal mucosa were about the same size in the two age groups, but in the hard palate plexus were 11–12% larger in aged mice (Fig. 5). Lymphatic valves in the hard palate plexus were 43–71% less numerous in aged mice (Fig. 5a,b). LYVE1 staining intensity of the hard palate lymphatic plexus was similar in the two age groups (Fig. 5a,b), which could reflect resistance of LYVE1$^+$ lymphatics to regression during ageing.

These differences in upstream lymphatics examined ex vivo were not accompanied by corresponding changes in scLV-1 or scLV-2, where the

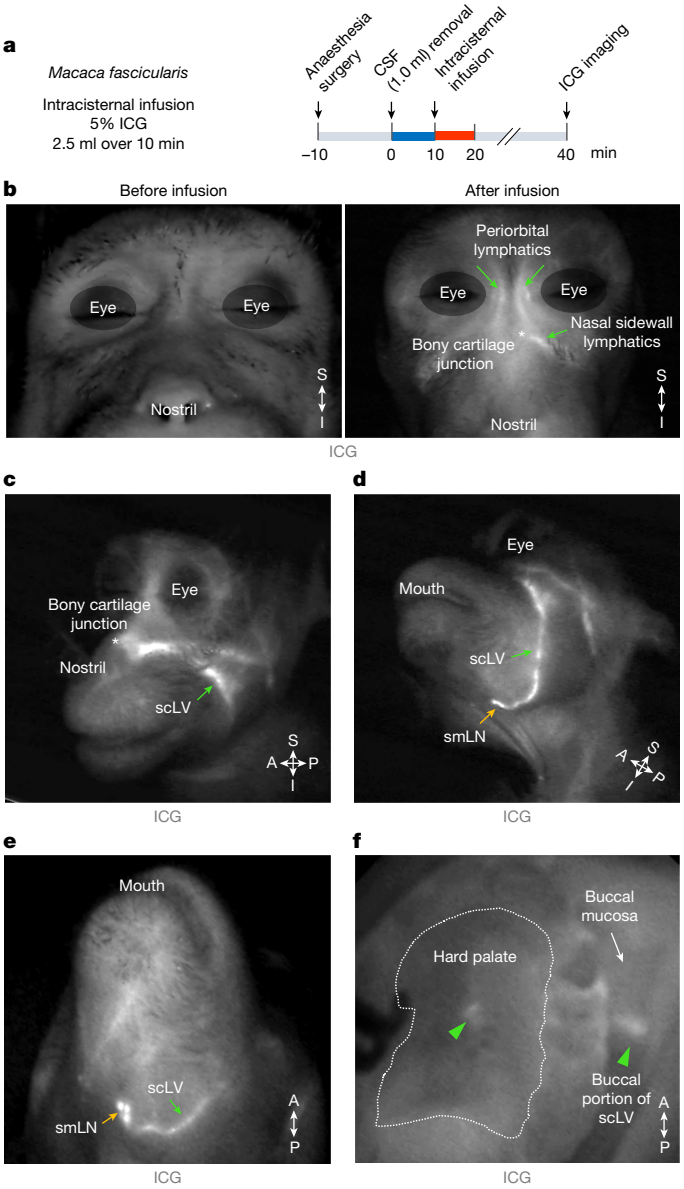


**Fig. 4 | CSF tracer in lymphatics around the eye and in the nasal sidewall, hard palate and superficial cervical regions of the monkey. a**, Sequence of intracisternal infusion of 2.5 ml indocyanine green (ICG) into *M. fascicularis* monkeys over 10 min followed at 30 min by imaging of ICG in the face and neck. Before infusion, 1.0 ml of CSF was removed at the cisterna magna over 10 min. **b**–**e**, Images of the face of monkeys before and after the intracisternal infusion showing ICG fluorescence (white) in lymphatics. The white asterisk (bone–cartilage junction) marks the lymphatic connection between the nasal mucosa and nasal sidewall. The green arrows indicate ICG in lymphatics in the periorbital and nasal sidewall regions and in scLVs. The yellow arrows indicate ICG in the smLN. Representatives of $n = 3$ monkeys from three independent experiments. **f**, Image showing ICG fluorescence (white) in hard palate and buccal lymphatics and scLVs (green arrowheads) of a monkey after intracisternal infusion. The white dashed line marks the boundary of the hard palate. Representatives of $n = 3$ monkeys from three independent experiments. Anatomical positions are indicated in the bottom right corner.

diameter, lymphangion length and αSMA$^+$ smooth muscle coverage of the mid-lymphangion region were similar in aged and younger adult mice. However, a small reduction (5.7%) was found in αSMA$^+$ smooth muscle coverage of the perivalvular region of scLV-1 and scLV-2 in aged mice (Extended Data Fig. 8a,b).

Spontaneous contractions and relaxations of scLV-1 were similar in aged and younger adult mice. Intravital imaging of scLV-1 revealed

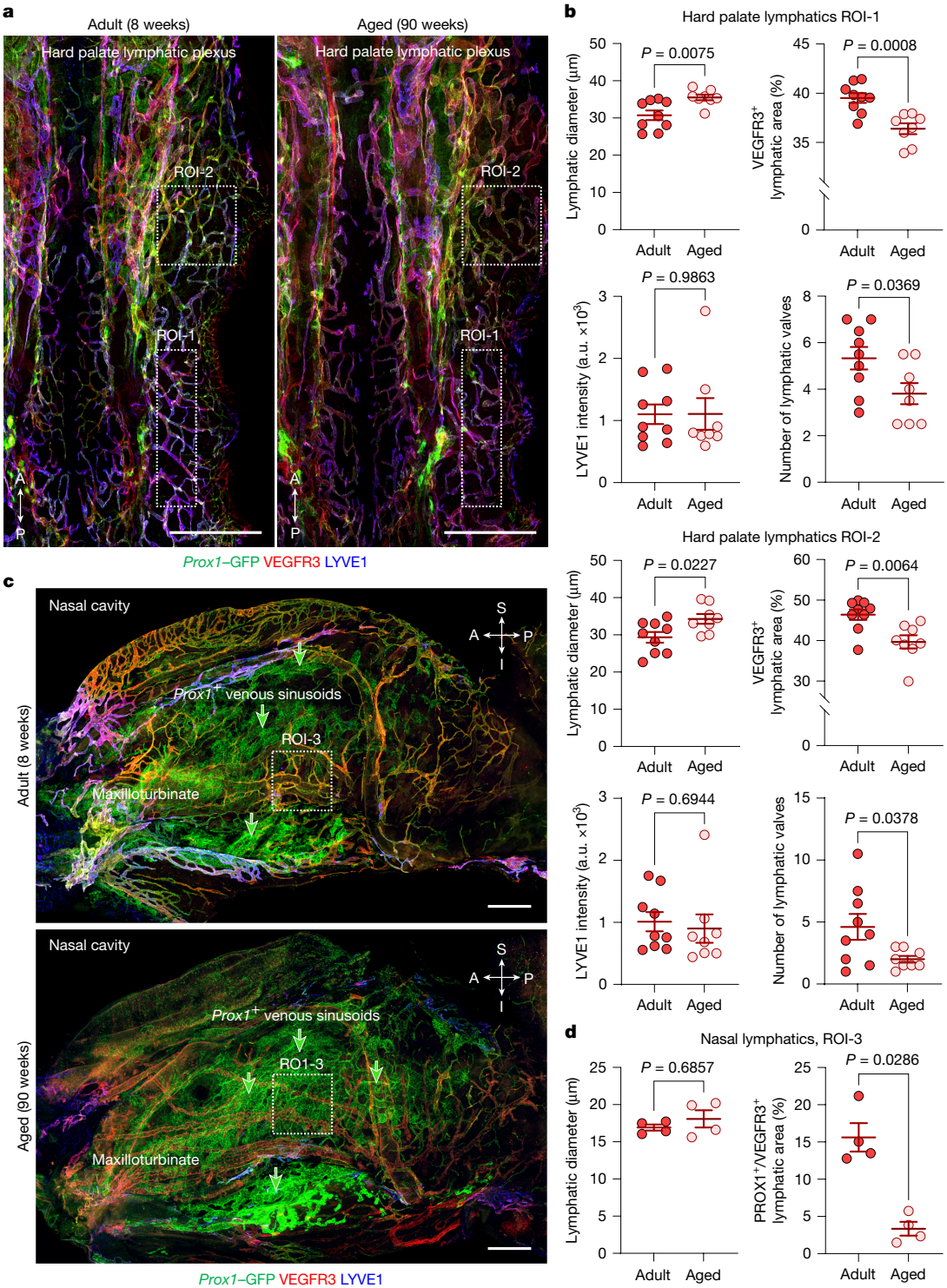


**Fig. 5 | Ageing-related changes in lymphatics of the nasal mucosa and hard palate. a**, Immunofluorescence images of whole mounts comparing hard palate lymphatics in adult (8 weeks of age) and aged (90 weeks of age) *Prox1*–GFP mice. Like lymphatics, venous sinusoids are PROX1$^+$. Ageing-related reductions in the lymphatic plexus are outlined by white dashed line boxes that mark regions of interest (ROIs) near the greater palatine nerve (ROI-1) and incisive foramen (ROI-2). Scale bars, 500 μm. Representative of $n = 9$ mice (adult) and $n = 8$ mice (aged) from three independent experiments. **b**, Comparison of lymphatic diameter, VEGFR3$^+$ lymphatic area, LYVE1 intensity and number of lymphatic valves in ROI-1 and ROI-2 in adult (8–10 weeks of age; $n = 9$) and aged (86–95 weeks of age; $n = 8$) *Prox1*–GFP mice. Each dot is the value for one mouse. The error bars indicate mean ± s.e.m. *P* values were calculated by two-tailed Welch's *t*-test. **c**, Immunofluorescence images of whole mounts comparing nasal lymphatics in adult (8 weeks of age) and aged (90 weeks of age) *Prox1*–GFP mice. Staining as in panel **a**. ROI-3 marks the measured region of PROX1$^+$/VEGFR3$^+$ nasal lymphatics (red) for data in panel **d**. Unlike PROX1$^+$/VEGFR3$^+$ nasal lymphatics, which are abundant in young adults but less in aged mice, PROX1$^+$ venous sinusoids (green; marked by green arrows) are more abundant in aged mice, as previously described[50]. Scale bars, 500 μm. Representative of $n = 4$ mice (adult) and $n = 4$ mice (aged) from three independent experiments. **d**, Comparison of lymphatic diameter and PROX1$^+$/VEGFR3$^+$ lymphatic area in nasal lymphatics of adult (8–10 weeks of age; $n = 4$) and aged (86–95 weeks of age; $n = 4$) *Prox1*–GFP mice. Each dot is the value for one mouse. The error bars indicate mean ± s.e.m. *P* values were calculated by two-tailed Mann–Whitney *U*-tests. Anatomical positions are indicated in the bottom left or top right corner.

no differences in diameter, contraction amplitude, frequency of spontaneous contraction, ejection fraction or fractional pump flow between aged and younger adults (Extended Data Fig. 8c–e). In addition, spontaneous contractions and relaxations within individual lymphangions of scLV-1 were comparably synchronized, as reflected by cross-correlations of synchronizing indices (Extended Data Fig. 8f). Similarly, scLV-1 examined ex vivo after removal from aged and younger adults had equivalent responses to pressures between 0.5 and 10 $cmH_2O$ and to the α1-adrenergic agonist phenylephrine in a range of $10^{-9}$ to $10^{-5}$ M (Extended Data Fig. 9a,b and Supplementary Fig. 13a,b).

Despite the similarities, the changes of end-diastolic diameter and normalized frequency to nitric oxide donor NONOate ($10^{-7}$ to $3 \times 10^{-6}$ M) of scLV-1 were smaller in aged mice (Extended Data Fig. 9c), which was evidence of dysfunctional nitric oxide synthesis and signalling in cervical lymphatics in aged mice. Despite the apparent nitric oxide insensitivity, no differences were found in spontaneous contraction parameters of scLV-1 in aged mice compared with younger adults (Extended Data Fig. 8c–e), implying that the CSF pumping function of cervical lymphatics is maintained during ageing.

Together, these findings revealed a mixture of ageing-related changes in lymphatic networks that drain through scLV-1 and scLV-2 to submandibular lymph nodes. Most conspicuous was the reduction in nasal mucosal lymphatics. Although scLV-1 and scLV-2 manifested few ageing-related structural changes, responses of these vessels to nitric oxide were impaired in aged mice.

## Transcriptomic changes in the scLV with ageing

To gain further insight into the nature of ageing-related changes in endothelial cells of scLV-1 and scLV-2, we performed single-cell RNA sequencing (scRNA-seq) analysis of pooled samples of cells isolated from cervical subcutaneous tissues that contained lymphatics proximal to and around the submandibular lymph nodes from six adult mice (three males and three females) and six aged mice (three males and three females; see Methods for details).

Unsupervised clustering analysis of 21,170 cells from the 12 mice revealed four distinct clusters of lymphatic vessel endothelial cells (LECs; 1,604 cells), blood vessel endothelial cells (640 cells), vascular mural cells (850 cells) and fibroblasts (18,076 cells; Supplementary Fig. 14a). These clusters were further divided into six subclusters of LECs, four subclusters of mural cells and five subclusters of fibroblasts, each distinguished by differential gene expression and annotated by subtype marker genes[23,45–51] (Supplementary Fig. 14b–e).

The identity of the six subclusters of LECs was characterized and validated by gene expression profiles, in situ hybridization and immunofluorescence staining. All LEC clusters had high expression of *Pecam1*, a pan-endothelial cell marker, and *Prox1*, a pan-LEC marker (Supplementary Fig. 14e). LEC subcluster gene expression profiles were annotated as collecting LEC (*Apoe*$^+$*Eng*$^+$*Bgn*$^+$), *Nos3*$^{high}$ collecting LEC (*Nos3*$^+$*Sparc*$^+$ *Igfbp*$^+$), *Foxp2*$^{high}$ LEC (*Foxp2*$^+$*Apoe*$^+$)[47,49], initial and pre-collecting (regional) cervical lymphatic LEC (*Lyve1*$^+$*Reln*$^+$*Piezo2*$^+$), upstream valve LEC (*Cldn11*$^+$*Neo1*$^+$) and downstream valve LEC (*Cldn11*$^+$*Adm*$^+$)[23,46,48,50] (Extended Data Fig. 10a and Supplementary Fig. 14b,e). Heatmaps revealed distinctive differences in the gene expression profiles of the six LEC clusters (Supplementary Fig. 15).

The proportion of cells in the *Nos3*$^{high}$ collecting LEC subcluster in aged mice (30.3% of 968 LECs) was 15-fold the value in younger adults (2.0% of 635 LECs; Extended Data Fig. 10b). The 10 genes in the *Nos3*$^{high}$ cluster from aged mice with the greatest expression (3.4–6.6-fold) compared with the other LEC clusters were *Dcpp1*, *Cyp1b1*, *Gm14636*, *Adipor2*, *Fam20a*, *Tead4*, *Fam135a*, *Sparc*, *Igfbp6* and *Klf3* (Supplementary Fig. 15). Previous reports[52–55] have shown that four of these genes (*Adipor2*, *Tead4*, *Sparc* and *Igfbp6*) are associated with ageing in multiple cell types. In the *Nos3*$^{high}$ collecting LEC cluster, *Adipor2*, *Sparc* and *Igfbp6* were found by volcano plot analysis to be upregulated 1.6–2.0-fold in aged mice (Extended Data Fig. 10c).

Analysis by Gene Ontology revealed that expression of multiple genes related to nitric oxide biosynthetic and metabolic processes was greater in the *Nos3*$^{high}$ collecting LEC subcluster of aged mice (Extended Data Fig. 10d). In addition to *Nos3*, aged mice had greater expression of *Sod2*, encoding superoxide dismutase 2, which reduces the burden of reactive oxygen species created when eNOS is uncoupled and produces superoxide instead of nitric oxide[56] (Extended Data Fig. 10e). Also having greater expression in the LECs of aged mice was *Gch1*, which encodes GTP cyclohydrolase, a rate-limiting enzyme in the production of a key NOS cofactor (tetrahydrobiopterin; Extended Data Fig. 10e). Unlike *Nos3*, expression of *Nos1*, encoding neuronal NOS, and *Nos2*, encoding inducible NOS, was not detected in the LECs of younger or aged mice (Extended Data Fig. 10e).

Greater *Nos3* expression in superficial cervical LECs was confirmed by RNA in situ hybridization for *Nos3* mRNA (Extended Data Fig. 11a–c). However, immunofluorescence staining revealed lower staining for eNOS protein and phosphorylated (Ser1177)-eNOS in these LECs of aged mice than in younger adults (Extended Data Fig. 11d,e). This discrepancy could be explained by dysregulated translational activity, protein stability or functional activity of eNOS in the LECs of aged mice[57,58].

Further validation studies revealed variable but clear FOXP2 immunoreactivity in the LECs of scLVs and uniformly strong in LECs of valves (Extended Data Fig. 11f,g). The combination of *Prox1*–GFP and LYVE1-marked regional lymphatics, consisting of initial lymphatics (with blunt ends) and pre-collecting lymphatics (with valves; Extended Data Fig. 11h–k). By comparison, αSMA$^+$ marked collecting lymphatics, which had smooth muscle cell envelopment but lacked LYVE1 (Extended Data Fig. 11i). Large veins were marked by αSMA$^+$ but not *Prox1*–GFP (Extended Data Fig. 11i).

Mural cell subclusters were annotated according to previous work[45,51] as lymphatic smooth muscle cells (*Acta2*$^+$*Myh11*$^+$*Nr4a2*$^{high}$*Scn3a*$^{high}$)[51], blood vessel smooth muscle cells (*Acta2*$^+$*Myh11*$^+$*Nr4a2*$^{low}$*Scn3a*$^{low}$)[51], *Dcn*$^{high}$ pericytes (*Vtn*$^+$*Dcn*$^{high}$)[45] and *Dcn*$^{low}$ pericytes (*Vtn*$^+$*Dcn*$^{low}$; Extended Data Fig. 10f and Supplementary Figs. 14c,e and 16). *Pdgfrb*, a pan-mural cell marker, was expressed in all mural cell clusters (Supplementary Fig. 14e).

Fibroblast subclusters were annotated as *Dpp4*$^{high}$ fibroblasts (*Dpp4*$^+$), *Postn*$^{high}$ fibroblasts (*Postn*$^+$; encoding periostin), *Cxcl14*$^{high}$ fibroblasts (*Cxcl14*$^+$*Cxcl12*$^+$), *Ptgfr*$^{high}$ fibroblasts (*Ptgfr*$^+$) and *Fmod*$^{high}$ fibroblasts (*Fmod*$^+$)[59,60] (Extended Data Fig. 12 and Supplementary Figs. 14d,e and 17). The pan-fibroblast markers *Pdgfra* and *Col1a2* were highly expressed in all fibroblast subclusters (Supplementary Fig. 14e).

Transcriptomes of lymphatic mural cell subclusters had few differences (Extended Data Fig. 10f), unlike the ageing-related changes in LECs. Both aged mice and younger adults had similar proportions and number of smooth muscle cells per LEC in collecting lymphatics, consistent with little or no change in these cells with ageing (Extended Data Fig. 10f–h). In addition, lymphatic smooth muscle cells, blood vessel smooth muscle cells and pericytes of aged mice had few differentially expressed genes than younger adults (Extended Data Fig. 10i). Mural cells in aged and younger adult mice had similar expression of canonical smooth muscle cell genes *Acta2*, *Myh11* and *Tagln* and nitric oxide-mediated activating enzymes *Gucy1a1* (encoding guanylate cyclase 1 soluble, α1) and *Gucy1a2* (encoding guanylate cyclase 1 soluble, α2; Extended Data Fig. 10j).

In comparison, two of the five fibroblast subclusters were 18 times as numerous in aged mice as in younger adults: *Postn*$^{high}$ cells represented 10.17% compared with 0.55%, and *Ptgfr*$^{high}$ cells represented 1.29% compared with 0.07% of total cells (Extended Data Fig. 12a,b). Similarly, Gene Ontology analysis revealed greater expression of fibrosis-related genes in the fibroblast clusters of aged mice (Extended Data Fig. 12c). As examples, *Postn*, *Tgfbi*, *Col1a1* and *Nfkb1* had greater expression in the fibroblasts of aged mice (Extended Data Fig. 12d). Cells with *Postn* mRNA

localized by RNA in situ hybridization were more abundant around scLVs of aged mice than of younger adults (Extended Data Fig. 12e–g). However, *Col1a1* expression, assessed by immunofluorescence staining for type 1 collagen, was greater around larger veins than around lymphatics (Extended Data Fig. 12h,i).

Together, these findings provide evidence for increased expression of *Nos3* and related genes in scLV LECs of aged mice; however, immunoreactivity for eNOS protein was reduced, indicating that nitric oxide signalling in these lymphatics could be impaired in ageing. Corresponding changes were not found in genes directly linked to contraction of lymphatic smooth muscle cells. Although periostin expression was greater in fibroblasts around lymphatics of aged mice, the increase in type I collagen was not restricted to lymphatics.

## Mechanical manipulation increases CSF outflow

We next determined whether CSF drainage could be increased by manipulating scLV-1 and scLV-2 through the intact skin, with the goal of reversing the CSF drainage impairment in aged mice. These vessels were chosen because of their accessibility due to their superficial location in the head and neck, unlike dcLV[23]. Another feature of scLV-1 and scLV-2 was the innervation of their smooth muscle cell envelopment by adrenergic sympathetic axons, which were identified by staining for tyrosine hydroxylase, but not by cholinergic parasympathetic axons stained for vesicular acetylcholine transporter (Supplementary Fig. 18).

To determine whether CSF outflow could be increased by non-invasive mechanical manipulation through the skin, we developed a force-regulated mechanical stimulator (see Methods for details) and compared low (0.01–0.02 kilogram-force (kgf)) and high (0.04–0.08 kgf) magnitude forces (Extended Data Fig. 13a,b and Supplementary Video 2). Using this device on urethane anaesthetized mice, we compared the effects of downward strokes in three regions of intact skin: (1) from the periorbital area to the mandible; (2) from the nasal sidewall to the mandible; and (3) from rostral to caudal along the path of scLV-1 and scLV-2 en route to the submandibular lymph node (Extended Data Fig. 13c). Each session consisted of two cycles of 10 strokes each of 2-s duration (4 strokes to region 1, 4 strokes to region 2 and 2 strokes to region 3). Two 10-stroke cycles over 40 s were followed by a 20-s rest period (Extended Data Fig. 13c and Supplementary Video 2).

Treatments consisted of five 1-min sessions of mechanical stimulation for tracer studies from the SAS to scLV-1 and scLV-2 (Fig. 6a). The TMR–dextran tracer was infused intracisternally 30 min before the onset of mechanical stimulation (Fig. 6a). CSF drainage was assessed by measuring tracer fluorescence in scLV-1 and scLV-2 at the end of the stimulation (Fig. 6a). TMR–dextran fluorescence more than doubled (2.29-fold mean increase) in scLV-1 and scLV-2 after low-magnitude stimulation over 5 min (Fig. 6b,c). By comparison, after high-magnitude stimulation over 5 min, scLV-1 and scLV-2 were constricted in some places and had 89% less TMR–dextran fluorescence than the sham (no stimulation; Fig. 6b,c).

For tracer studies from the SAS to cervical lymph nodes, treatments consisted of 20 1-min sessions of mechanical stimulation (Fig. 6d). The TMR–dextran tracer was infused at the cisterna magna 10 min before the onset of mechanical stimulation, and CSF drainage was assessed by measuring tracer fluorescence in submandibular lymph nodes at the end of the stimulation (Fig. 6d–f). TMR–dextran fluorescence tripled (3.01-fold mean increase) in the ipsilateral lymph node after low-magnitude mechanical stimulation over 20 min but not after high-magnitude stimulation (Fig. 6d–f), where values were less in the ipsilateral lymph nodes (Fig. 6d–f). In comparison, no differences among the three groups were found in the contralateral lymph nodes (Fig. 6d–f).

To determine whether mechanical stimulation of facial and neck skin increased CSF clearance from the SAS, instead of just pushing lymph in scLV-1 and scLV-2 into cervical lymph nodes, we injected TMR–dextran into a lateral ventricle and applied 10 1-min sessions of low-magnitude mechanical stimulation (Fig. 6g). Measurements of CSF removed at the cisterna magna revealed a 23% lower concentration of TMR–dextran in the stimulation group than in the sham group ($P = 0.03$; Fig. 6h and Supplementary Fig. 19), consistent with increased CSF clearance from the SAS.

We next determined the magnitude and duration of the increase in CSF outflow after a 1-min session of low-magnitude mechanical stimulation by using TMR–dextran fluorescence in scLVs as a readout (Extended Data Fig. 14a,b). TMR–dextran fluorescence measured by intravital imaging was more than doubled at 1 min after stimulation, and the increase was sustained throughout the 5-min monitoring period (Extended Data Fig. 14c,d). Mechanical stimulation was also accompanied by a small increase in the diameter of scLVs and a transient increase in the amplitude of spontaneous contractions, but no consistent change in spontaneous contraction ejection fraction, frequency or fractional pump flow (Extended Data Fig. 14d).

Repeated low-magnitude mechanical stimulation (20 1-min sessions daily) for 4 days did not change the spontaneous contraction parameters (Extended Data Fig. 14e,f) or impair the stimulation-mediated increase in CSF outflow through scLV-1 (Extended Data Fig. 14g,h). These findings provide promising evidence that prolonged mechanical stimulation of lymphatics in the face and neck can promote a sustained increase in CSF outflow.

We then tested the contribution of nitric oxide signalling to spontaneous cycles of contraction and relaxation of scLV-1 and to the effect of mechanical stimulation on CSF drainage to cervical lymph nodes (Extended Data Fig. 15). Adult mice (8–12 weeks) were given *N*(ω)-nitro L-arginine methyl ester (L-NAME; 1.0 mg $kg^{-1}$ body weight) by intraperitoneal injection to block nitric oxide synthesis 90 min before intracisternal infusion of TMR–dextran (Extended Data Fig. 15a,d). Analysis of spontaneous contraction–relaxation cycles of scLV-1 revealed that L-NAME decreased mean vessel diameter, contraction amplitude, ejection fraction and fractional pump flow (Extended Data Fig. 15b,c and Supplementary Video 3). L-NAME also reduced the accumulation of TMR–dextran by 31% in the submandibular lymph node after 20 1-min sessions of low-magnitude stimulation (Extended Data Fig. 15d–f), consistent with the contribution of nitric oxide signalling to spontaneous contractility of scLV-1 and scLV-2 and to increased CSF drainage to superficial cervical lymph nodes after mechanical stimulation of the skin of young adult mice.

To test the efficacy of the approach in correcting CSF drainage impairment, we asked whether mechanical stimulation of facial and neck skin increased CSF outflow to cervical lymph nodes in aged mice (Fig. 7a), where TMR–dextran drainage was approximately 30% less than in younger adults (Supplementary Fig. 12). Using the same stimulation protocols in aged mice (87–105 weeks), we found that TMR–dextran accumulation was increased 2.81-fold in the submandibular lymph node after 20 1-min low-magnitude stimulation sessions (Fig. 7a–c) and increased 4.7-fold in scLV-1 and scLV-2 after 5 1-min sessions (Fig. 7d–f). These increases were similar in magnitude to those in younger adult mice (Extended Data Fig. 15d–f). The doubling of CSF tracer drainage to superficial cervical lymph nodes more than offset the reduction in baseline drainage in aged mice (Supplementary Fig. 12).

These findings show the feasibility of doubling CSF drainage to superficial cervical lymph nodes by non-invasive, force-regulated, mechanical stimulation of the skin of the face and neck for 20 min. The results also show that the reduction in CSF drainage to cervical lymph nodes in aged mice can be reversed by mechanical stimulation of the skin. This reversal points to the potential feasibility of adapting the non-invasive approach for the treatment of patients with neurological conditions accompanied by impaired CSF drainage.

## Discussion

Evidence for reduced or insufficient CSF outflow from the SAS in ageing and some neurological conditions has stimulated interest in developing

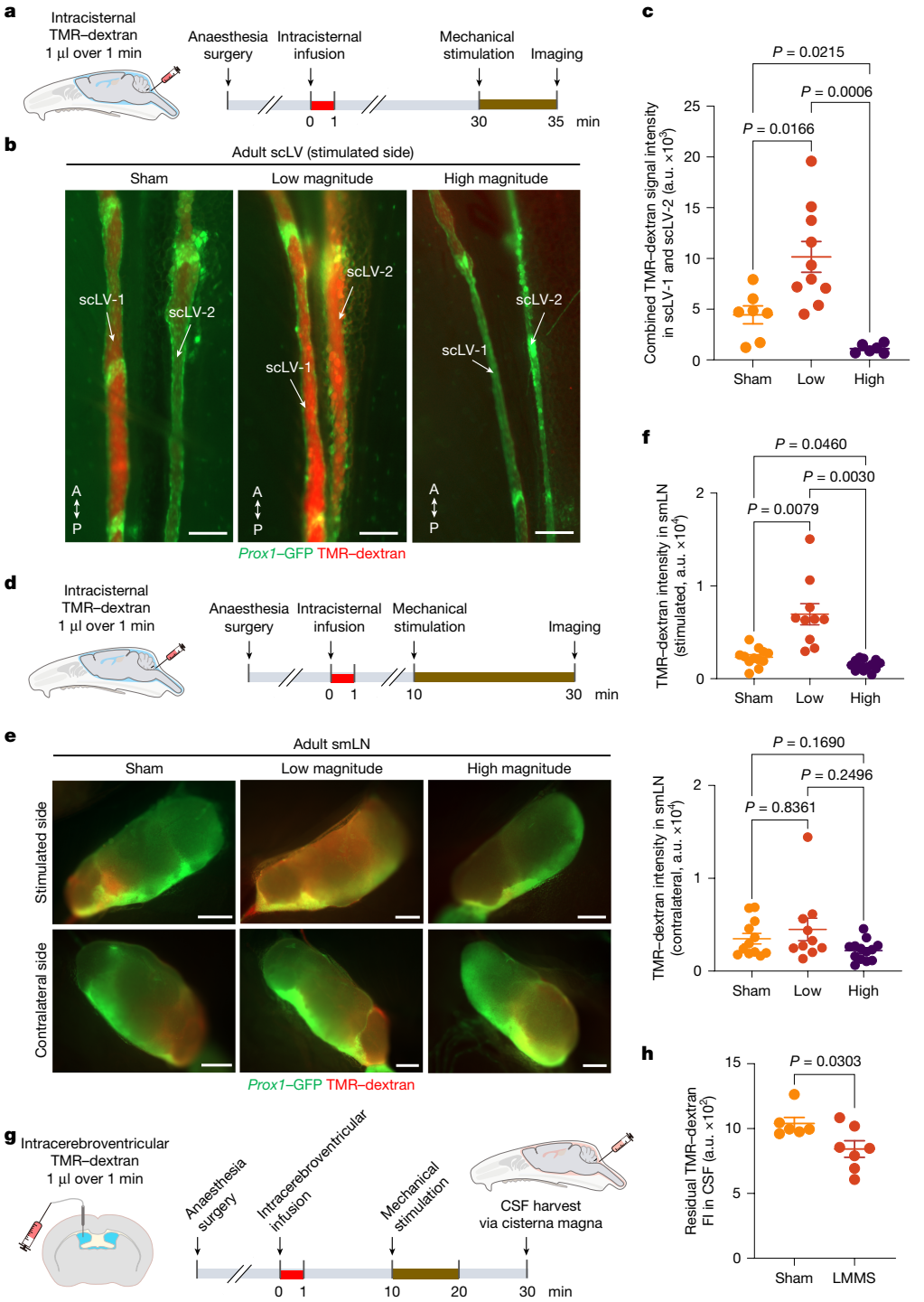


**Fig. 6 | Increased CSF drainage by non-invasive mechanical stimulation of scLVs. a**, Sequence of intracisternal infusion of TMR–dextran into *Prox1*–GFP mice followed by mechanical stimulation at 30 min for 5 min, then imaging of TMR–dextran in scLV-1 and scLV-2 at 35 min. **b**,**c**, Fluorescence images and measurements of TMR–dextran in scLV-1 and scLV-2. Sham compared with mechanical stimulation (**b**). Anatomical positions are indicated. Scale bars, 200 µm. Each dot represents combined TMR–dextran fluorescence intensity in scLV-1 and scLV-2 from one mouse (**c**). $n = 7$ (sham), $n = 10$ (low magnitude) and $n = 6$ (high magnitude) from three independent experiments. The error bars indicate mean ± s.e.m. *P* values were calculated by Brown–Forsythe analysis of variance (ANOVA) test followed by two-tailed Dunnett's T3 multiple comparison post-hoc test. **d**, Sequence of intracisternal infusion of TMR–dextran into *Prox1*–GFP mice followed by mechanical stimulation at 10 min for 20 min, then imaging of TMR–dextran in the smLN at 30 min. **e**,**f**, Fluorescence images (**e**) and measurements (**f**) of TMR–dextran in the smLN of the stimulated side (top) versus unstimulated side (bottom). Scale bars, 500 µm. Each dot is the value for one mouse. $n = 12$ (sham), $n = 10$ (low magnitude) and $n = 13$ (high magnitude) from three independent experiments. The error bars indicate mean ± s.e.m. *P* values were calculated by Brown–Forsythe ANOVA test followed by two-tailed Dunnett's T3 multiple comparison post-hoc test. **g**,**h**, Sequence of intracerebroventricular infusion of TMR–dextran into *Prox1*–GFP mice followed by low-magnitude mechanical stimulation (LMMS) at 10 min for 10 min and removal of CSF at 30 min (**g**). Fluorescence in CSF after LMMS or sham is also shown (**h**). Each dot is the value for one mouse. $n = 6$ (sham) and $n = 7$ (LMMS) from three independent experiments. The error bars indicate mean ± s.e.m. *P* values were calculated by two-tailed unpaired *t*-test with Welch's correction. FI, fluorescence intensity.

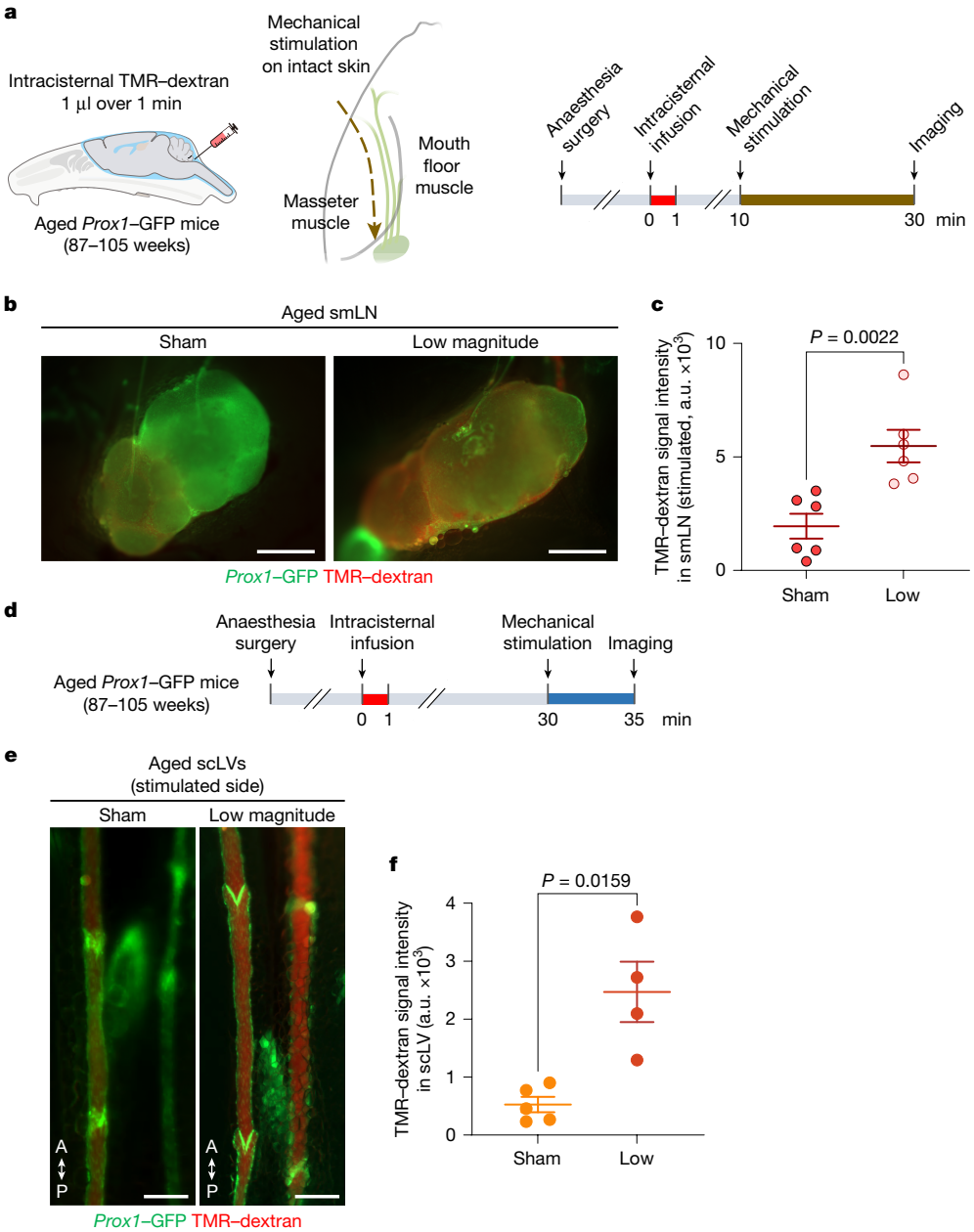


**Fig. 7 | Increased CSF drainage in aged mice by mechanical stimulation of scLVs. a**, Sequence of intracisternal infusion of 1.0 µl TMR–dextran over 1 min into aged *Prox1*–GFP mice (87–105 weeks of age) followed 10 min later by sham or low-magnitude mechanical stimulation of intact skin over 20 min beginning 10 min after TMR–dextran infusion. TMR–dextran fluorescence was imaged and measured in the ipsilateral smLN at 30 min. **b**,**c**, Fluorescence images (**b**) and measurements (**c**) of TMR–dextran fluorescence in the smLN after ipsilateral low-magnitude mechanical stimulation of the skin or no stimulation (sham) over 20 min. Scale bars, 500 µm. Each dot is the TMR–dextran fluorescence intensity of the smLN in one mouse. $n = 6$ mice per group from three independent experiments. The error bars indicate mean ± s.e.m. *P* values were calculated by two-tailed Mann–Whitney *U*-test. **d**, Sequence of intracisternal infusion of 1.0 µl TMR–dextran over 1 min into aged *Prox1*–GFP mice (87–105 weeks of age) followed by sham or low-magnitude mechanical stimulation of intact skin over 5 min beginning 30 min after TMR–dextran infusion. TMR–dextran fluorescence was imaged and measured in ipsilateral scLV-1 and scLV-2 at 35 min. **e**,**f**, Fluorescence images and measurements of TMR–dextran fluorescence in scLV-1 and scLV-2 at 35 min after ipsilateral low-magnitude mechanical stimulation of the skin or no stimulation (sham) over 5 min. Anatomical positions are shown in the bottom left corner. Scale bars, 200 µm. Each dot is the value of the combined TMR–dextran fluorescence intensity of scLV-1 and scLV-2 from one mouse. $n = 5$ (sham) and $n = 4$ (low-magnitude mechanical stimulation) mice per group from three independent experiments. The error bars indicate mean ± s.e.m. *P* values were calculated by two-tailed Mann–Whitney *U*-test.

methods for increasing CSF drainage through lymphatics. The present study documented the feasibility of using a non-invasive mechanical approach for reversing the reduction in CSF drainage during ageing by increasing CSF outflow through the superficial lymphatic pathway to cervical lymph nodes of mice. Tracer studies revealed that a substantial amount of CSF outflow to cervical lymph nodes normally traversed this pathway. Although CSF outflow in this pathway was reduced by approximately 30% in aged mice, the reduction could be largely corrected by tightly regulated mechanical stimulation of these lymphatics through the skin.

Mechanistic studies revealed that smooth muscle and valves of scLVs continue to function during ageing and promote spontaneous,

unidirectional pumping of CSF to cervical lymph nodes. Transdermal mechanical stimulation of the facial and neck skin increased CSF outflow from the SAS by repeatedly compressing the superficial lymphatics, whereas it had little or no effect on spontaneous lymphatic contractility during or after the procedure.

The finding that diminished CSF flow to deep cervical lymph nodes after ligation of dcLV was compensated by greater CSF flow to superficial cervical lymph nodes illustrated the plasticity of this CSF clearance pathway. However, overall CSF outflow can decrease during ageing, which is reported to result from reduced CSF production, changes in intracranial CSF circulation or impaired lymphatic CSF efflux[12,20,24,25,61–63]. The present study revealed prominent alterations that could contribute to reduced CSF outflow in ageing. Among these were marked reduction of nasal lymphatics, blunted relaxation responses to nitric oxide despite expansion of the *Nos3*$^{high}$ collecting LEC subpopulation, and fibrosis in cervical tissues.

Dysregulation of CSF clearance can also exaggerate the severity and consequences of traumatic brain injury, neurodegenerative diseases, neuroimmune conditions and certain other neurological disorders[26,33,34,64,65]. However, claims of the therapeutic benefit of increasing CSF outflow by expanding dural lymphatic networks[29,30] are premature because of the incomplete understanding of the function and regulation of intracranial lymphatics and their contributions to CSF drainage. In addition, experimental approaches used in mice in published reports are unlikely to be amenable to translation into clinical use. In addition to ageing effects on CSF, including reduced production, changes in intracranial circulation and impaired lymphatic efflux[12,20,24,25,61–63], brain oedema after head concussion can lead to suppression of CSF outflow resulting from noradrenaline release in a mouse model[34].

Experimental strategies for correcting impaired CSF clearance have included promoting CSF production or augmenting CSF outflow[23,25,34,66–69]. Both intracranial and extracranial approaches have been used to increase CSF outflow[23,25,34,66]. VEGF-C, delivered by viral vector-mediated gene transfer[15,23,25,30] or intracranial delivery of hydrogel-encapsulated VEGF-C or VEGF-C156S[25], can expand the networks of meningeal and nasopharyngeal lymphatics by promoting lymphangiogenesis in adult mice. Complementing the published work, the present study showed that VEGF-C overexpression can expand upstream lymphatics of the scLV pathway. All of these approaches can increase CSF drainage to cervical lymph nodes of mice[15,23,25,30].

CSF drainage can also be increased by using cervical lymphatics as targets of local or systemic pharmacological agents by exploiting their accessibility in the neck, smooth muscle coverage and valves that prevent backflow. CSF drainage through cervical lymphatics can be increased by direct application of the α1-adrenergic agonist phenylephrine, nitric oxide donor sodium nitroprusside or prostaglandin $F_{2\alpha}$ after surgical exposure[23,69]. Alternatively, systemic treatment with the mechanosensor Piezo1 agonist Yoda1 can reverse meningeal lymphatic defects and CSF outflow impairment in *Twist1*-haploinsufficient mice[67]. Piezo1 agonists can also increase CSF outflow and reduce abnormal CSF accumulation in mouse models of hydrocephalus and Down syndrome[68].

Studies of pharmacological approaches for increasing CSF outflow have the attribute of showing feasibility, but they have the limitation of involving invasive procedures and/or risks of systemic adverse effects that could jeopardize or prevent clinical use. To circumvent these limitations, we explored the feasibility of increasing CSF outflow by non-invasive mechanical stimulation of scLVs through the skin.

As the first step, we identified the outflow routes taken by CSF from the SAS to scLV-1 or scLV-2 en route to cervical lymph nodes. scLV-1 carried CSF that flowed from meningeal lymphatics that exited the skull through the orbital fissure and joined periorbital lymphatics en route to scLV-1 and the submandibular lymph node. By contrast, scLV-2 carried CSF from meningeal lymphatics near the olfactory bulb that traversed the cribriform plate and joined nasal mucosal lymphatics en route to scLV-2 and the submandibular lymph node. In addition, scLV-2 received CSF from meningeal lymphatics that exited the greater palatine canal and from nasal lymphatics that traversed the incisive foramen en route to the hard palate lymphatic plexus and onwards to scLV-2 and the submandibular lymph node. The involvement of the hard palate lymphatic plexus in CSF outflow is provocative because its continuous motion during chewing, mastication, suckling and speech would be expected to promote CSF drainage through the lymphatic plexus to scLV-2.

Next, we determined whether CSF drainage could be increased by mechanical stimulation of the intact facial and neck skin along the CSF outflow route through superficial lymphatics. Experiments established feasibility but showed that repeated, low-magnitude mechanical stimulation was necessary to increase CSF outflow to cervical lymph nodes. Further studies revealed that the augmented CSF outflow by transdermal stimulation of cervical lymphatics largely reversed the impaired clearance of CSF in aged mice.

Multiple questions would need to be addressed before clinical studies of low-magnitude mechanical transdermal stimulation could be considered. Among these is why CSF clearance through lymphatics is impaired in ageing, traumatic brain injury and other neurological conditions. Another remaining question is how dysregulated nitric oxide signalling in lymphatics contributes to reduced CSF outflow after brain injury and in other conditions. Mechanical stimulation is efficacious in aged mice despite cervical lymphatics having less eNOS protein and relative insensitivity to nitric oxide from NONOate. Also to be determined is whether mechanical stimulation of the facial and neck skin daily over more than 4 days can sustain the increase in CSF outflow in ageing and chronic neurodegenerative conditions. Although gentle stimulation of the skin in humans would not require the anaesthesia used in mice, translation to clinical use will require practical approaches for assessing CSF drainage.

Overall, the present study revealed the previously unrecognized importance of scLVs as a route for CSF outflow and highlighted the potential for increasing CSF drainage during ageing and under pathological conditions by non-invasive, regulated mechanical stimulation of these lymphatics through the skin.

## Online content

Any methods, additional references, Nature Portfolio reporting summaries, source data, extended data, supplementary information, acknowledgements, peer review information; details of author contributions and competing interests; and statements of data and code availability are available at https://doi.org/10.1038/s41586-025-09052-5.


1. Key, A. & Retzius, G. *Studien in der Anatomie des Nervensystems und des Bindegewebes: 1. Hälfte* Vol. 1 (Samson & Wallin, 1875).
2. Bradbury, M. W. B. & Cserr, H. F. Drainage of cerebral interstitial fluid and of cerebrospinal fluid into lymphatics. *Exp. Biol. Lymph. Circ.* **9**, 355–394 (1985).
3. Cserr, H. F., Harling-Berg, C. J. & Knopf, P. M. Drainage of brain extracellular fluid into blood and deep cervical lymph and its immunological significance. *Brain Pathol.* **2**, 269–276 (1992).
4. Kida, S., Pantazis, A. & Weller, R. O. CSF drains directly from the subarachnoid space into nasal lymphatics in the rat. Anatomy, histology and immunological significance. *Neuropathol. Appl. Neurobiol.* **19**, 480–488 (1993).
5. Zakharov, A., Papaiconomou, C., Djenic, J., Midha, R. & Johnston, M. Lymphatic cerebrospinal fluid absorption pathways in neonatal sheep revealed by subarachnoid injection of Microfil. *Neuropathol. Appl. Neurobiol.* **29**, 563–573 (2003).
6. Koh, L., Zakharov, A. & Johnston, M. Integration of the subarachnoid space and lymphatics: is it time to embrace a new concept of cerebrospinal fluid absorption? *Cerebrospinal Fluid Res.* **2**, 6 (2005).
7. Johnston, M., Zakharov, A., Koh, L. & Armstrong, D. Subarachnoid injection of Microfil reveals connections between cerebrospinal fluid and nasal lymphatics in the non-human primate. *Neuropathol. Appl. Neurobiol.* **31**, 632–640 (2005).
8. Koh, L. et al. Development of cerebrospinal fluid absorption sites in the pig and rat: connections between the subarachnoid space and lymphatic vessels in the olfactory turbinates. *Anat. Embryol.* **211**, 335–344 (2006).
9. Nagra, G., Koh, L., Zakharov, A., Armstrong, D. & Johnston, M. Quantification of cerebrospinal fluid transport across the cribriform plate into lymphatics in rats. *Am. J. Physiol. Regul. Integr. Comp. Physiol.* **291**, R1383–R1389 (2006).
10. Aspelund, A. et al. A dural lymphatic vascular system that drains brain interstitial fluid and macromolecules. *J. Exp. Med.* **212**, 991–999 (2015).

11. Louveau, A. et al. Structural and functional features of central nervous system lymphatic vessels. *Nature* **523**, 337–341 (2015).
12. Tarasoff-Conway, J. M. et al. Clearance systems in the brain-implications for Alzheimer disease. *Nat. Rev. Neurol.* **11**, 457–470 (2015).
13. Absinta, M. et al. Human and nonhuman primate meninges harbor lymphatic vessels that can be visualized noninvasively by MRI. *eLife* **6**, e29738 (2017).
14. Ma, Q., Ineichen, B. V., Detmar, M. & Proulx, S. T. Outflow of cerebrospinal fluid is predominantly through lymphatic vessels and is reduced in aged mice. *Nat. Commun.* **8**, 1434 (2017).
15. Antila, S. et al. Development and plasticity of meningeal lymphatic vessels. *J. Exp. Med.* **214**, 3645–3667 (2017).
16. Ahn, J. H. et al. Meningeal lymphatic vessels at the skull base drain cerebrospinal fluid. *Nature* **572**, 62–66 (2019).
17. Proulx, S. T. Cerebrospinal fluid outflow: a review of the historical and contemporary evidence for arachnoid villi, perineural routes, and dural lymphatics. *Cell. Mol. Life Sci.* **78**, 2429–2457 (2021).
18. das Neves, S. P., Delivanoglou, N. & Da Mesquita, S. CNS-draining meningeal lymphatic vasculature: roles, conundrums and future challenges. *Front. Pharmacol.* **12**, 655052 (2021).
19. Wichmann, T. O., Damkier, H. H. & Pedersen, M. A brief overview of the cerebrospinal fluid system and its implications for brain and spinal cord diseases. *Front. Hum. Neurosci.* **15**, 737217 (2022).
20. Decker, Y. et al. Magnetic resonance imaging of cerebrospinal fluid outflow after low-rate lateral ventricle infusion in mice. *JCI Insight* **7**, e150881 (2022).
21. Jacob, L. et al. Conserved meningeal lymphatic drainage circuits in mice and humans. *J. Exp. Med.* **219**, e20220035 (2022).
22. Spera, I. et al. Open pathways for cerebrospinal fluid outflow at the cribriform plate along the olfactory nerves. *eBioMedicine* **91**, 104558 (2023).
23. Yoon, J.-H. et al. Nasopharyngeal lymphatic plexus is a hub for cerebrospinal fluid drainage. *Nature* **625**, 768–777 (2024).
24. Smyth, L. C. D., Beschorner, N., Nedergaard, M. & Kipnis, J. Cellular contributions to glymphatic and lymphatic waste clearance in the brain. *Cold Spring Harb. Perspect. Biol.* https://doi.org/10.1101/cshperspect.a041370 (2024).
25. Da Mesquita, S. et al. Functional aspects of meningeal lymphatics in ageing and Alzheimer's disease. *Nature* **560**, 185–191 (2018).
26. Louveau, A. et al. CNS lymphatic drainage and neuroinflammation are regulated by meningeal lymphatic vasculature. *Nat. Neurosci.* **21**, 1380–1391 (2018).
27. Patel, T. K. et al. Dural lymphatics regulate clearance of extracellular tau from the CNS. *Mol. Neurodegener.* **14**, 11 (2019).
28. Betsholtz, C. et al. Advances and controversies in meningeal biology. *Nat. Neurosci.* **27**, 2056–2072 (2024).
29. Li, Z. et al. Blockade of VEGFR3 signaling leads to functional impairment of dural lymphatic vessels without affecting autoimmune neuroinflammation. *Sci. Immunol.* **8**, eabq0375 (2023).
30. Antila, S. et al. Sustained meningeal lymphatic vessel atrophy or expansion does not alter Alzheimer's disease-related amyloid pathology. *Nat. Cardiovasc. Res.* **3**, 474–491 (2024).
31. Jacob, L. et al. Anatomy and function of the vertebral column lymphatic network in mice. *Nat. Commun.* **10**, 4594 (2019).
32. Choi, I. et al. Visualization of lymphatic vessels by Prox1-promoter directed GFP reporter in a bacterial artificial chromosome-based transgenic mouse. *Blood* **117**, 362–365 (2011).
33. Bolte, A. C. et al. Meningeal lymphatic dysfunction exacerbates traumatic brain injury pathogenesis. *Nat. Commun.* **11**, 4524 (2020).
34. Hussain, R. et al. Potentiating glymphatic drainage minimizes post-traumatic cerebral oedema. *Nature* **623**, 992–1000 (2023).
35. Nelson-Maney, N. P. et al. Meningeal lymphatic CGRP signaling governs pain via cerebrospinal fluid efflux and neuroinflammation in migraine models. *J. Clin. Invest.* **134**, e175616 (2024).
36. Smyth, L. C. D. et al. Identification of direct connections between the dura and the brain. *Nature* **627**, 165–173 (2024).
37. Scallan, J. P., Zawieja, S. D., Castorena-Gonzalez, J. A. & Davis, M. J. Lymphatic pumping: mechanics, mechanisms and malfunction. *J. Physiol.* **594**, 5749–5768 (2016).
38. Petrova, T. V. & Koh, G. Y. Biological functions of lymphatic vessels. *Science* **369**, eaax4063 (2020).
39. Zawieja, S. D., Castorena-Gonzalez, J. A., Scallan, J. P. & Davis, M. J. Differences in L-type $Ca^{2+}$ channel activity partially underlie the regional dichotomy in pumping behavior by murine peripheral and visceral lymphatic vessels. *Am. J. Physiol. Heart Circ. Physiol.* **314**, H991–H1010 (2018).
40. Davis, M. J. et al. Kir6.1-dependent KATP channels in lymphatic smooth muscle and vessel dysfunction in mice with Kir6.1 gain-of-function. *J. Physiol.* **598**, 3107–3127 (2020).
41. Kim, H. J., Li, M., Nichols, C. G. & Davis, M. J. Large-conductance calcium-activated $K^+$ channels, rather than KATP channels, mediate the inhibitory effects of nitric oxide on mouse lymphatic pumping. *Br. J. Pharmacol.* **178**, 4119–4136 (2021).
42. Papadopoulos, Z. et al. Differential impact of lymphatic outflow pathways on cerebrospinal fluid homeostasis. *J. Exp. Med.* **222**, e20241752 (2025).
43. Nagai, T., Bridenbaugh, E. A. & Gashev, A. A. Aging-associated alterations in contractility of rat mesenteric lymphatic vessels. *Microcirculation* **18**, 463–473 (2011).
44. Zolla, V. et al. Aging-related anatomical and biochemical changes in lymphatic collectors impair lymph transport, fluid homeostasis, and pathogen clearance. *Aging Cell* **14**, 582–594 (2015).
45. Wong, A. P., Nili, N. & Strauss, B. H. In vitro differences between venous and arterial-derived smooth muscle cells: potential modulatory role of decorin. *Cardiovasc. Res.* **65**, 702–710 (2005).
46. González-Loyola, A. et al. FOXC2 controls adult lymphatic endothelial specialization, function, and gut lymphatic barrier preventing multiorgan failure. *Sci. Adv.* **7**, eabf4335 (2021).
47. Hernández Vásquez, M. N. et al. Transcription factor FOXP2 is a flow-induced regulator of collecting lymphatic vessels. *EMBO J.* **40**, e107192 (2021).
48. Abe, Y. et al. A single-cell atlas of non-haematopoietic cells in human lymph nodes and lymphoma reveals a landscape of stromal remodelling. *Nat. Cell Biol.* **24**, 565–578 (2022).
49. Petkova, M. et al. Immune-interacting lymphatic endothelial subtype at capillary terminals drives lymphatic malformation. *J. Exp. Med.* **220**, e20220741 (2023).
50. Hong, S. P. et al. Three-dimensional morphologic and molecular atlases of nasal vasculature. *Nat. Cardiovasc. Res.* https://doi.org/10.1038/s44161-023-00257-3 (2023).
51. Lei, P.-J. et al. Aging-induced changes in lymphatic muscle cell transcriptomes are associated with reduced pumping of peripheral collecting lymphatic vessels in mice. *Dev. Cell* https://doi.org/10.1016/j.devcel.2024.12.010 (2024).
52. Ryu, S. et al. The matricellular protein SPARC induces inflammatory interferon-response in macrophages during aging. *Immunity* **55**, 1609–1626.e1607 (2022).
53. Zhang, D. et al. TEAD4 antagonizes cellular senescence by remodeling chromatin accessibility at enhancer regions. *Cell. Mol. Life Sci.* **80**, 330 (2023).
54. López-Otín, C., Blasco, M. A., Partridge, L., Serrano, M. & Kroemer, G. Hallmarks of aging: an expanding universe. *Cell* **186**, 243–278 (2023).
55. Ruiz, M. et al. Aging AdipoR2-deficient mice are hyperactive with enlarged brains excessively rich in saturated fatty acids. *FASEB J.* **38**, e23815 (2024).
56. Förstermann, U., Xia, N. & Li, H. Roles of vascular oxidative stress and nitric oxide in the pathogenesis of atherosclerosis. *Circ. Res.* **120**, 713–735 (2017).
57. Kalinowski, L. et al. Posttranscriptional and transcriptional regulation of endothelial nitric-oxide synthase during hypoxia: the role of microRNAs. *Cell. Mol. Biol. Lett.* **21**, 16 (2016).
58. Janaszak-Jasiecka, A. et al. eNOS expression and NO release during hypoxia is inhibited by miR-200b in human endothelial cells. *Angiogenesis* **21**, 711–724 (2018).
59. Hong, S. P. et al. Distinct fibroblast subsets regulate lacteal integrity through YAP/TAZ-induced VEGF-C in intestinal villi. *Nat. Commun.* **11**, 4102 (2020).
60. Muhl, L. et al. Single-cell analysis uncovers fibroblast heterogeneity and criteria for fibroblast and mural cell identification and discrimination. *Nat. Commun.* **11**, 3953 (2020).
61. Chiu, C. et al. Temporal course of cerebrospinal fluid dynamics and amyloid accumulation in the aging rat brain from three to thirty months. *Fluids Barriers CNS* **9**, 3 (2012).
62. Liu, G. et al. Direct measurement of cerebrospinal fluid production in mice. *Cell Rep.* **33**, 108524 (2020).
63. Mestre, H. et al. Periarteriolar spaces modulate cerebrospinal fluid transport into brain and demonstrate altered morphology in aging and Alzheimer's disease. *Nat. Commun.* **13**, 3897 (2022).
64. Yanev, P. et al. Impaired meningeal lymphatic vessel development worsens stroke outcome. *J. Cereb. Blood Flow Metab.* **40**, 263–275 (2020).
65. Merlini, A. et al. Distinct roles of the meningeal layers in CNS autoimmunity. *Nat. Neurosci.* **25**, 887–899 (2022).
66. Boisserand, L. S. B. et al. VEGF-C prophylaxis favors lymphatic drainage and modulates neuroinflammation in a stroke model. *J. Exp. Med.* **221**, e20221983 (2024).
67. Matrongolo, M. J. et al. Piezo1 agonist restores meningeal lymphatic vessels, drainage, and brain-CSF perfusion in craniosynostosis and aged mice. *J. Clin. Invest.* **134**, e171468 (2024).
68. Choi, D. et al. Piezo1 regulates meningeal lymphatic vessel drainage and alleviates excessive CSF accumulation. *Nat. Neurosci.* **27**, 913–926 (2024).
69. Du, T. et al. Restoration of cervical lymphatic vessel function in aging rescues cerebrospinal fluid drainage. *Nat. Aging* https://doi.org/10.1038/s43587-024-00691-3 (2024).



**Publisher's note** Springer Nature remains neutral with regard to jurisdictional claims in published maps and institutional affiliations.

**Open Access** This article is licensed under a Creative Commons Attribution-NonCommercial-NoDerivatives 4.0 International License, which permits any non-commercial use, sharing, distribution and reproduction in any medium or format, as long as you give appropriate credit to the original author(s) and the source, provide a link to the Creative Commons licence, and indicate if you modified the licensed material. You do not have permission under this licence to share adapted material derived from this article or parts of it. The images or other third party material in this article are included in the article's Creative Commons licence, unless indicated otherwise in a credit line to the material. If material is not included in the article's Creative Commons licence and your intended use is not permitted by statutory regulation or exceeds the permitted use, you will need to obtain permission directly from the copyright holder. To view a copy of this licence, visit http://creativecommons.org/licenses/by-nc-nd/4.0/.

© The Author(s) 2025

# Methods

### Study approval

All animal care and experimental procedures were approved for mice by the Institutional Animal Care and Use Committees of the Korea Advanced Institute of Science and Technology (KAIST; KA2024-122-v1) and the University of Missouri (9797), and for *M. fascicularis* monkeys by the Korea Research Institute of Bioscience and Biotechnology (KRIBB-AEC-24079).

### Animals

*Prox1*–GFP mice[32] (FVB background, 8–12 weeks of age for adults and 80–105 weeks of age for aged mice) were bred and maintained under specific pathogen-free conditions at KAIST. Adult (8–12 weeks of age) and aged (80–95 weeks of age) C57BL/6J mice were purchased from JAX (USA) or the Animal Center of Aging Science of Korea Basic Science Institute. Mice received ad libitum access to a standard diet and water and were exposed to 12-h light–dark cycles at 23–24 °C and 40–60% humidity. Experiments were performed during the light period. Mice of both sexes were used for all experiments and were anaesthetized by intraperitoneal injection of urethane (1.5 mg $kg^{-1}$) or a mixture of urethane (1.5 mg $kg^{-1}$), ketamine (0.75 mg $kg^{-1}$) and xylazine (0.3 mg $kg^{-1}$) before procedures. Supplemental anaesthesia was given as necessary during procedures. Body temperature was maintained at 36.5–37.5 °C during surgical and imaging procedures.

*M. fascicularis* monkeys (7–14 years of age), maintained at the National Primate Research Center of the Korea Research Institute of Bioscience and Biotechnology, were housed individually to prevent physical contact and minimize potential harm during the experiment but had visual and auditory interactions with neighbouring monkeys. Cage dimensions (60 cm × 80 cm × 80 cm) followed the guidelines of the US National Institutes of Health. Monkeys were housed with 12-h light–dark cycles at 22–26 °C and 45–55% humidity and provided a commercial monkey diet (Teklad 2050, Envigo), assorted fruits, ad libitum water, and rubber and plastic toys for environmental enrichment. Monkeys were anaesthetized by intramuscular injection of ketamine (5 mg $kg^{-1}$) and atropine (0.02 mg $kg^{-1}$) before the procedures and supplemented as necessary during procedures. Veterinary monitoring adhered to the non-human primates research guidelines[70].

### Imaging of CSF outflow to scLVs

To assess CSF outflow through periorbital, nasal and hard palate lymphatics to scLVs and lymph nodes, 1 µl of phosphate-buffered saline (PBS) containing TMR–dextran (10 kDa, 50 mg $ml^{-1}$; D1816, Invitrogen) was infused over 1 min into the SAS at the cisterna magna of *Prox1*–GFP mice[23]. Anaesthetized mice in the prone position were placed on a stereotaxic frame under a surgical microscope. The head was adjusted to a 90° angle to the body axis with the help of a mouthpiece to facilitate access to the cisterna magna. After the skin was incised in the midline of the posterior neck, the muscle layers were carefully separated with microscissors. The atlanto-occipital membrane overlying the cisterna magna was superficially penetrated using a 33-gauge NanoFil needle (World Precision Instruments). Then, 1 µl of PBS containing TMR–dextran was infused into the SAS over 1 min using a microsyringe (88000, Hamilton) and a micro-infusion machine (Fusion 100, Chemyx Inc.). The needle was left in position for 7 min and then slowly removed to prevent CSF leakage. The muscle layers and neck skin were then sutured with 6-0 black silk (SK617, Ailee). The abdominal aorta was cut to remove blood 15–120 min after the infusion, and the neck skin above the submandibular lymph node was removed under a fluorescence surgical microscope (SZX16, Olympus). Although the direction of TMR–dextran in lymphatics scLV-1 and scLV-2 that drained to the submandibular lymph node was observed, the skin overlying the nasal sidewall, medial cantus, cheek, chin and anterior auricular regions, including lateral canthus was carefully removed without damaging the lymphatics. Superficial cervical lymph nodes were exposed by dissecting the fascial layer and surrounding adipose tissue in the direction of lymphatics that drained from the submandibular lymph node to the parotid lymph node. Then, images of the lateral and ventral sides of the head and neck were obtained to record TMR–dextran in periorbital, nasal or hard palate lymphatics connected to cervical lymphatics. Images were captured with a fluorescence stereo zoom microscope (AxioZoom V16, ZEN 2.3 (blue) v2.3.64.0, Carl Zeiss) with a Plan-Neofluar Z ×1.0 objective lens and HE-GFP or Cy3 filter (Carl Zeiss). PBS was used to prevent tissue drying during dissection and imaging.

### Infusion of fluorescent tracers in mice

One microlitre of FluoSpheres (diameter of 0.5 µm, polystyrene microbeads, carboxylate-modified surface, red fluorescent (580/605), 2% solids 98% DW; F8887, Thermo Fisher Scientific) or 1 µl of Qdot 705 (Q21361MP, Invitrogen) was infused over 1 min into the SAS of *Prox1*–GFP mice at the cisterna magna[16,23,33]. Subsequently, the head was removed for the histological analysis as described in section 'Tissue preparation and immunohistochemistry'. One microlitre of Alexa-647-conjugated ovalbumin (O34784, Invitrogen) was infused into the mouth floor over 1 min to identify the initial region of the lymph drainage through scLV-3 to the submandibular lymph node. TMR–dextran (0.5 µl) was infused intradermally over 1 min into each of three facial regions: (1) nasal and medial canthus; (2) lateral canthus and anterior auricular; and (3) cheek and chin.

### Ligation of cervical LVs

To determine the effect of blocking flow through dcLV or scLVs on CSF outflow to cervical lymph nodes, either the medial and lateral dcLV or scLVs were ligated bilaterally with 10-0 polypropylene suture (W2794, Ethicon) after the neck muscles were retracted in *Prox1*–GFP mice[23]. Sham controls underwent the same operation without the ligation. Two weeks later, TMR–dextran fluorescence in cervical lymph nodes and the nasopharyngeal route was measured 60 min after intracisternal infusion of TMR–dextran (1.0 µl).

### Tracer infusion and intravital imaging in monkeys

The monkeys were positioned in the sphinx posture using a custom-built stereotaxic frame, and then FluoSpheres or indocyanine green[71] were delivered by image-guided cisterna magna infusion under isoflurane anaesthesia (1.5% in 2 l $min^{-1}$ oxygen). Placement of the needle tip within the cisterna magna was confirmed using XperCT imaging (Philips), and then the correct position was verified by CSF discharge. Oxygen saturation, heart rate, respiration rate and body temperature were monitored and maintained within normal ranges[72]. Ten minutes before infusion of the tracers, 1 ml of CSF was removed with a 23-gauge needle connected to a 1-ml Hamilton syringe via a Dual Removable Needle Coupler (Hamilton). After CSF removal, FluoSpheres or indocyanine green (5% in PBS; 1340009, Merck) were infused into the SAS at 250 µl $min^{-1}$ over 10 min using a micro-infusion device (World Precision Instruments). The needle was left in position for 20 min and slowly removed to prevent CSF regurgitation. After the FluoSpheres infusion, monkeys emerged from anaesthesia and were awake under vital monitoring. Thirty minutes after infusion of indocyanine green into the cisterna magna, lymphatics and lymph nodes in the head and neck were imaged with an infrared detector (FLUOBEAM FB800, FLUOPTICS) under isoflurane (1.5% in 2 l $min^{-1}$ oxygen) anaesthesia with vital monitoring.

### Intracisternal delivery of AAV9–VEGF-C

*Prox1*–GFP mice were anaesthetized by intraperitoneal injection of a mixture of ketamine (10 mg $kg^{-1}$) and xylazine (1 mg $kg^{-1}$). Five minutes before intracisternal injection, atipamezole (1 mg $kg^{-1}$; A9611, Sigma) was administered intraperitoneally. One microlitre of AAV9–VEGF-C–mCherry (AAV9-275994-mCherry, Vector Biolabs) or AAV9–mCherry (7107, Vector Biolabs), with a concentration of $1 \times 10^{13}$ gene copies per

millilitre in PBS was infused into the SAS at the cisterna magna at 1 µl over 1 min. At 4 weeks after infusion, the nasal mucosa, hard palate, dorsal meninges and scLVs were removed for the histological analysis as described in 'Tissue preparation and immunohistochemistry'.

### Intravital imaging of scLVs

*Prox1*–GFP mice were anaesthetized and laid in a supine position. An imaging window for scLV-1, scLV-2 and scLV-3 was created by incising the skin overlying the lymphatics in a location 6 mm proximal and 6 mm distal to the submandibular lymph node and 5 mm from the midline to the masseter muscle. Then, the exposed lymphatics were imaged with a high-speed confocal microscope (IVIM-CM3, IVIM Engine 3.10.10, pinhole size was 2 mm, IVIM Technology) while body temperature was maintained at 37 °C with a heating pad. A GFP filter (band-pass filter for 503–558 nm) was used. After a 20–30-min period for the lymphatics to stabilize, images were acquired at 20 frames per second for 5–10 min with a Plan-Apochromat ×10/0.45 lens (Nikon). Images had a resolution of 768 × 768 pixels (0.71 µm per pixel). Lymphatics were immersed in PBS during the intravital imaging to prevent drying.

### Mechanical stimulation for increasing CSF drainage

We developed a precision force-regulated mechanostimulator designed to increase CSF outflow by applying mechanical stimulation to periorbital, nasal sidewall and scLVs without surgery (Extended Data Fig. 13a). The stimulator weighing 91.3 g consisted of a replaceable tip, handle, force sensor, shaft connecting the tip and the force sensor, and amplifier. The housing of the stimulator was created with a 3D printer (Single Plus-320C, CUBICON) having a acrylonitrile butadiene styrene filament (ABS-A100, CUBICON). The replaceable tip was a 1 cm × 0.5 cm oval cotton ball attached to a 1-cm long rod that fit securely into the shaft. The length of the handle was 9 cm, preventing interference by keeping the sensor away from the hand. The force sensor made of silicone (Ecoflex 00-10, Dragonskin10, Smooth-On Inc.) and conductive fabric (Stretch conductive fabric 4800, Holland Shielding Systems) was connected to the replaceable tip through the shaft, enabling precise measurement of the force at the tip (Extended Data Fig. 13a). The measured force was transmitted to an amplifier, which relayed the data to a personal computer via a universal serial bus connector.

Transmitted data were processed with custom LabView codes (v2017, National Instruments Inc.). The device was calibrated by setting the measurements for the state when no force was applied and when a force of 0.05 kgf was applied on an electronic scale (Supplementary Video 4). The magnitude of the stimulation was optimized using this precision force-regulated stimulator. The force of mechanical stimulation was set at two levels: low magnitude (0.01–0.02 kgf) and high magnitude (0.04–0.08 kgf; Extended Data Fig. 13b).

Each 20-stroke session of mechanical stimulation lasted 1 min and consisted of a cycle of 10 downward sweeping-strokes, with each stroke lasting 2 s, followed by a second cycle of 10 strokes and then a 20-s rest period (Extended Data Fig. 13c). Three regions of intact skin were stimulated during each cycle: (1) from the periorbital area to the mandible (four strokes); (2) from the nasal sidewall to the mandible (four strokes); and (3) along the rostral to caudal path of scLV-1 and scLV-2 to the submandibular lymph node (two strokes; Extended Data Fig. 13c).

### Measurement of the effects of mechanical stimulation

*Prox1*–GFP mice at age 8–12 weeks of age (adult) or age 80–105 weeks of age (aged) were anaesthetized exclusively by intraperitoneal injection of urethane (1.5 mg $kg^{-1}$) and then received 5 or 20 1-min sessions of mechanical stimulation on one side of the face and neck. Ketamine and xylazine anaesthesia were not used because of their variable effects on CSF outflow. Corresponding sham control mice received no stimulation. Before stimulation, TMR–dextran (1 µl) was infused into the cisterna magna and then the head was immobilized with a polydimethylsiloxane head frame. After the stimulation, mice were euthanized, and TMR–dextran fluorescence in scLV-1 and scLV-2 (after 5 sessions; Fig. 6a) or the submandibular lymph node (after 20 sessions; Fig. 6d) was measured with a fluorescence stereo zoom microscope (AxioZoom V16, ZEN 2.3 (blue) v2.3.64.0, Plan-Neofluar Z ×1.0 objective lens, Carl Zeiss) and HE-GFP or Cy3 filter (Carl Zeiss).

The involvement of nitric oxide synthesis in the response to the mechanical stimulation was tested by administering the NOS inhibitor L-NAME (1.0 mg $kg^{-1}$ body weight, injected intraperitoneally) 90 min before the TMR–dextran infusion at the cisterna magna of young adult *Prox1*–GFP mice. As previously described[73], mean arterial blood pressure did not change after injection of L-NAME in mice anaesthetized with urethane. Mice pretreated with L-NAME or PBS received 20 sessions of mechanical stimulation on one side of the head and neck. Sham controls received no stimulation.

To quantify fluorescent tracers in CSF after mechanical stimulation in adult *Prox1*–GFP mice, TMR–dextran was first infused into the lateral ventricle, as previously described[16,23], and then the facial and neck skin was stimulated. CSF was collected through the cisterna magna 30 min after the initial infusion. A small hole was drilled at the medial–lateral axis 1.5 mm and anterior–posterior axis −1.0 mm relative to the bregma after exposing the skull on a stereotaxic frame to perform intracerebroventricular infusion. A 33-gauge NanoFil needle (World Precision Instruments) connected to a PE-20 catheter was inserted to a depth of 2 mm. One microlitre of PBS containing TMR–dextran (10 kDa, 50 mg $ml^{-1}$; D1816, Invitrogen) was infused into the lateral ventricle at 1 µl over 1 min using a microsyringe (88000, Hamilton) and a micro-infusion pump (Fusion 100, Chemyx Inc). After infusion, the NanoFil needle was left in place for 5 min to prevent backflow and then slowly removed. The hole was sealed with a mixture of resin and superglue. After the infusion, the mice were placed in the supine position, and mechanical stimulation was applied for 10 min to the ipsilateral side of the intracerebroventricular infusion. Ten minutes after the end of mechanical stimulation, CSF was collected through the cisterna magna. To collect CSF, the meninges were exposed using the same methods as for the cisterna magna infusion, and the 33-gauge NanoFil needle connected to a PE-20 catheter was inserted into the SAS. Using a micro-infusion pump (Fusion 200x, Chemyx Inc.), CSF was withdrawn at a rate of 1 µl $min^{-1}$ for 2 min. Collected CSF was diluted in 200 µl PBS, and the fluorescence intensity of 100 µl of the mixed solution was measured with a stereo zoom microscope (AxioZoom V16, ZEN 2.3 (blue) v2.3.64.0, Carl Zeiss) with a Plan-Neofluar Z ×1.0 objective lens and Cy3 filter (Carl Zeiss). Stereo microscopic measurements of TMR–dextran in CSF were calibrated from a standard curve made from serial dilutions (Supplementary Fig. 19).

### Tissue preparation and immunohistochemistry

Whole mounts of the periorbital region, nasal mucosa, hard palate, cribriform plate region and dorsal meninges of *Prox1*–GFP mice were prepared 20 min, 30 min, 60 min or 4 weeks after intracisternal infusion of TMR–dextran, QDot 705, FluoSpheres or AAV9-VEGF-C. The head and neck were removed at the C2 vertebral level immediately after vascular perfusion of ice-cold PBS followed by 2% paraformaldehyde (PFA) fixative through left ventricle. Blood and fixative exited through a puncture in the right atrium. Then, the mandible was removed to expose the hard and soft palate. After cutting the gingiva with a microscissor, the hard palate was removed by grabbing the soft palate with fine forceps under a surgical microscope. The hard palate was incubated in 2% PFA for 2 h at 4 °C. Then, the head was cut in half along the sagittal plane with a blade. After the overlying skin and muscle were removed, the nasal mucosa was carefully detached from the skull and lateral nasal wall, incubated in 0.5 M EDTA solution for 48 h at 4 °C, and prepared as previously described[50]. The periorbital area tissue was removed from the remaining half-cut head. The zygomatic arch was removed to avoid damage to associated soft tissue. The eye lens, vitreous body and retina were removed, and the soft tissue of the periorbital area was

carefully separated from surrounding small bone. The nasal mucosa and periorbital area tissue were incubated in 2% PFA for 2 h at 4 °C. The dorsal meninges was processed without detachment from the skull during immunofluorescence staining. The dorsal part of skull was fixed with 2% PFA for 2 h at 4 °C and decalcified with 0.5 M EDTA solution for 12 h at 4 °C. Tissues of mice infused with QDot 705 were removed for imaging 20 min after intracisternal infusion without previous perfusion of PBS or 2% PFA.

For the whole-mount preparation of scLVs and superficial cervical lymph nodes, mice were perfused with ice-cold PBS and 2% PFA, and cervical lymphatics and lymph nodes were removed with surrounding tissue, pinned with insect pins to prevent tangling, and post-fixed in 2% PFA for 2 h at 4 °C. The tissues were washed with PBS and incubated in CUBIC-L solution (T3740, TCI) with daily change for 3 days at 37 °C. After clearing and PBS washing, tissues were stained for immunofluorescence and imaging.

Monkeys were perfused through the vasculature with ice-cold PBS and 4% PFA. The submandibular, parotid and retropharyngeal lymph nodes were removed, further fixed with 2% PFA for 12 h at 4 °C, dehydrated with 30% sucrose at 4 °C, and washed in PBS. After 48 h, lymph nodes were embedded and frozen in frozen section medium (Leica) and cut into 10-µm sections using a Cryocut Microtome (Leica). The head specimens were fixed with 4% PFA for 2 h and 2% PFA for 24 h at 4 °C. The lower mandibles were removed and the hard palate was collected. The hard palate was imaged using a fluorescence stereo zoom microscope (AxioZoom V16, ZEN 2.3 (blue) v2.3.64.0, Carl Zeiss) with a Plan-Neofluar Z ×1.0 objective lens with HE-GFP or Cy3 filter (Carl Zeiss).

Tissues from mice and monkeys were incubated in 5% normal donkey serum (017-000-121, Jackson ImmunoResearch) for 1 h at room temperature and then incubated with primary antibodies (1:400) dissolved in 5% normal donkey serum at 4 °C for 12 h. After washing in PBS, they were incubated with secondary antibodies (1:1,000) dissolved in 5% normal donkey serum at 4 °C for 12 h. Specimens that had been cleared were incubated with donkey serum for 24 h at room temperature and fluorophore-conjugated primary antibodies at 1:200 dilution at room temperature for 5 days. After PBS washing, the specimens were immersed in a refractive index matching solution (D-PROTOSS)[74].

Primary antibodies used were: anti-mouse LYVE1 (rabbit polyclonal; 11-034, Angiobio); anti-mouse VEGFR3 (goat polyclonal; AF743, R&D Systems); anti-mouse αSMA-Cy3 (mouse monoclonal, clone 1A4; C6198, Sigma); anti-mouse laminin α5 (rabbit polyclonal; EWL004, kerafast); anti-mouse CD31 (hamster monoclonal, clone 2H8; MAB1398Z, Merck); anti-mouse tyrosine hydroxylase (rabbit polyclonal; AB152, Merck); anti-mouse vesicular acetylcholine transporter (VAChT, also known as solute carrier family 18 (vesicular acetylcholine), member 3, Slc18a3, goat polyclonal; ABN100, Merck); anti-monkey LYVE1 (rabbit polyclonal; DP3500, OriGene); anti-mouse eNOS antibody (rabbit polyclonal; ab5589, Abcam); anti-mouse phospho-eNOS antibody (rabbit polyclonal; 9571, Cell Signaling); anti-mouse FOXP2 antibody (goat polyclonal; ab1307, Abcam); anti-mouse ER-TR7 antibody (rat monoclonal, clone ER-TR7; sc-73355, Santa Cruz Biotechnology); anti-mouse Col1a1 (rabbit monoclonal, clone E8F4L; 72026, Cell Signaling); and anti-mouse PDGFRα (goat polyclonal; AF1062, R&D Systems). Secondary antibodies were: Alexa Fluor 488-conjugated, 594-conjugated and 647-conjugated anti-rabbit (711-545-152, 711-585-152 and 711-605-152, respectively), anti-goat (705-585-147), anti-hamster (127-605-160) and anti-rat (712-605-153; all Jackson ImmunoResearch) in the blocking buffer for overnight at 4 °C. The manufacturers validated the species and applications of all the antibodies used in this study.

### RNA in situ hybridization

RNA in situ hybridization for *Nos3* and *Postn* mRNA in scLV whole mounts from *Prox1*–GFP mice was performed using the RNAscope kit (323280, ACDBio) with target probes to *Nos3* (443061-C2, ACDBio) and *Postn* (418581-C2, ACDBio), according to the manufacturer's specifications. scLVs were fixed with 2% PFA overnight at 4 °C and then permeabilized by incubation in a mixture of 0.1% Tween 20 in PBS and 1% bovine serum albumin (BSA). Target retrieval was omitted to preserve the *Prox1*–GFP signal. The samples were imaged and analysed as described in 'Imaging and morphometric analysis'.

### Imaging and morphometric analysis

Immunofluorescent images were acquired with an LSM800 or LSM880 confocal microscope (Carl Zeiss). ZEN 2.3 (blue) v2.3.69.1010 and ZEN 2.1 SP3 (black) v14.0.4.201 software (Carl Zeiss) was used for image acquisition and processing. Confocal images of tissue whole mounts and sections were projected at maximum intensity of tiled or single *z*-stack images through the entire thickness of tissues. All images had a resolution of 512 × 512 or 1,024 × 1,024 pixels and were obtained with an air objectives Plan-Apochromat ×10/0.45 numerical aperture (NA) M27, Plan-Apochromat 20x/0.8 NA M27 or a water immersion objective LD C-Apochromat ×40/1.1 NA Corr M27 with multichannel scanning in the frame. Specimens that underwent tissue clearing and decalcification were imaged with a light-sheet fluorescence microscope (Lighsheet 7, Carl Zeiss) with an EC Plan-Neofluar ×5/0.16 lens.

Morphometric measurements were made with ImageJ software (NIH) or Zen software (Carl Zeiss) on maximum-intensity-projected confocal images. $VEGFR3^+$ lymphatic area, LYVE1 signal intensity, lymphatic vessel diameter and number of lymphatic valves were measured on the submucosal side of the hard palate at the two ROIs: ROI-1 (greater palatine nerve area, 850 µm × 650 µm), ROI-2 (near the CSF outflow area, 450 µm vs 450 µm). The $VEGFR3^+$ area in ROI-1 and ROI-2 was measured using the Weka trainable segmentation of ImageJ plugin[75]. The diameter of lymphatics and number of lymphatic valves were counted with ImageJ. Signal intensities of LYVE1 were measured in the submucosal side of the hard palate in the region (ROI-1 and ROI-2) defined by the aforementioned boundaries. The $VEGFR3^+$ lymphatic area and lymphatic vessel diameter in the nasal mucosa were measured in ROI-1 and ROI-2 measuring 330 µm × 330 µm. In specimens from *Prox1*–GFP mice, the area of GFP fluorescence of lymphatics and lymphatic diameter were measured in meningeal lymphatics on the transverse sinus and extracranial lymphatics in the nasal mucosa and submucosal side of the hard palate using the Weka trainable segmentation of ImageJ plugin[75]. The diameter of *Prox1*–GFP lymphatics was measured with ImageJ. Measurements were made at ROIs: ROI-1 (respiratory mucosa, 700 µm × 700 µm), ROI-2 (inferior nasal mucosa, 700 µm × 700 µm) and ROI-3 (submucosal side of the hard palate near the incisive foramen, 450 µm × 450 µm). The diameter, number of lymphatic valves and length of lymphangions in scLVs were measured with ImageJ. $\alpha SMA^+$ smooth muscle coverage per lymphangion was measured in at least three lymphangions of each scLVs using the Weka trainable segmentation of the ImageJ plugin[75]. The *Nos3* and *Postn* mRNA signal was measured with ImageJ by counting the number of spots in random regions (159 µm × 159 µm) that included lymphangions of scLV. Type 1 collagen expression was measured by average fluorescence intensity in random regions (830 µm × 830 µm) that included the scLV and facial vein.

Intravital images were aligned with an Image Stabilizer of the ImageJ plugin[76]. Then, a perpendicular line was drawn to obtain intensity profiles for 1–6 min using a custom ImageJ macro. For each intensity profile, the full-width half-maximum was extracted to measure the diameter of scLVs with a custom MATLAB (R2023b, MathWorks) code. The diameter of these lymphatics was used to calculate the amplitude of spontaneous contraction and relaxation, frequency, ejection fraction and fractional pump flow for 1 min as previously described[37]. To determine whether spontaneous contractions and relaxations were synchronized within each lymphangion, cross-correlations of diameter changes were calculated at five locations, spaced 40 µm apart, using a custom MATLAB code.

### Ex vivo studies of pressurized scLVs

Mice were anaesthetized by intraperitoneal injection of a ketamine and xylazine mixture and laid in a supine position on a heated pad. A proximal-to-distal incision was made in the skin from the neck to the sternum. A 0.5–1.5-mm long segment of scLVs on both sides was removed with fine forceps and microscissors and transferred to a dish containing Krebs solution with 0.5% BSA. The lymphatics were then pinned with short segments of 40-µm stainless steel wire onto a Sylgard-coated dissection chamber filled with Krebs-BSA buffer at room temperature. Surrounding adipose and connective tissues were removed by microdissection. An isolated lymphatic was then transferred to a 3-ml observation chamber on the stage of a Zeiss inverted microscope, cannulated, and pressurized to 1 $cmH_2O$ using two glass micropipettes (50–60 µm outside diameter). With the vessel pressurized, the segment was cleared of remaining connective and adipose tissue.

Polyethylene tubing was attached to the back of each glass micropipette and connected to a computerized pressure controller, with independent control of inflow and outflow pressures. To minimize diameter-tracking artefacts associated with longitudinal bowing at higher intraluminal pressures, input and output pressures were briefly increased to 10 $cmH_2O$ at the beginning of each experiment, and the vessel segment was stretched axially to remove any longitudinal slack. Following this procedure, each lymphatic was equilibrated at 37 °C at a pressure of 1 $cmH_2O$. Constant exchange of Krebs buffer was maintained at a peristaltic pump rate of 0.5 ml $min^{-1}$. Within 30 min after the temperature stabilized, scLVs began to exhibit spontaneous contractions. Custom LabView programs (National Instruments Inc.) acquired real-time analogue data and digital video through an A-D interface (National Instruments Inc.) and detected the inner diameter of the vessel[37]. Videos of the contractile activity of lymphatics were recorded for further analyses under brightfield illumination at 30 fps using a firewire camera (Basler, Graftek Imaging).

### Ex vivo assessment of lymphatic responses

To assess physiological responses of scLV segments to pressure changes, intraluminal pressure was lowered from 1 to 0.5 $cmH_2O$, then raised to 1, 2, 3, 5, 8 and 10 $cmH_2O$, while the internal diameter was recorded for 1–2 min at each pressure. Both the input and the output pressures were maintained at equal levels, so there was no imposed pressure gradient for forwards flow. After the pressure was returned to 1 $cmH_2O$ for 5 min, phenylephrine was added to the bath in cumulative concentrations, while the diameter was recorded for 1–2 min at each concentration. Once a maximum tone was reached (typically 40–50% of the passive diameter), diethylamine-NONOate sodium salt hydrate (sodium NONOate, Merck) was applied in cumulative concentrations, and the diameter was measured at each concentration. At the end of each experiment, the lymphatic was equilibrated by perfusion with calcium-free Krebs buffer containing 3 mM EGTA for 30 min, and passive diameters were measured at each intraluminal pressure.

### Droplet-based scRNA-seq

After anaesthesia, *Prox1*–GFP adult mice ($n = 3$ males and $n = 3$ females at 12 weeks of age) and aged mice ($n = 3$ males and $n = 3$ females at 93 weeks of age) were perfused with ice-cold PBS. scLVs near the submandibular lymph node and surrounding tissue were removed and pooled in DMEM/F12 medium (Gibco). The tissues were cut into small pieces and incubated in dissociation buffer containing 2 mg $ml^{-1}$ of collagenase II (Worthington), 1 mg $ml^{-1}$ of dispase (Gibco) and 0.2 mg $ml^{-1}$ DNase I (Gibco) at 37 °C for 30 min with gentle pipetting up and down every 10 min. Dissociated tissue was then filtered through a 70-µm strainer, and an equal volume of PBS containing 10% FBS was added to stop digestion. The cells were centrifuged for 10 min at 300*g* and resuspended in PBS containing 2% FBS. The resuspended cells were incubated with anti-PDGFRα antibody-conjugated Microbead Kit (103-101-502, Miltenyi Biotec) on ice for 15 min to separate $PDGFR\alpha^+$ cells from $PDGFR\alpha^-$ cells using magnetic columns (130-042-401, Miltenyi Biotec). Then, immune cells and dead cells were removed by FACS (FACSAria Fusion, Beckton Dickinson) after staining with anti-mouse CD45 antibody (103147, clone 30-F11, BioLegend) and DAPI (564907, Sigma-Aldrich) at 4 °C for 20 min. Subsequently, $PDGFR\alpha^+$ cells and $PDGFR\alpha^-$ cells were mixed in a 2:8 ratio to enrich $PDGFR\alpha^-$ cells population to more than 15%.

The cells were then centrifuged for 10 min at 300*g*, resuspended in 2% FBS in PBS, and processed using Chromium Next GEM Single Cell 3p RNA library kit v3.1 (10X Genomics) following the manufacturer's protocol. The cells were mixed with reverse transcription reagent mix and reverse transcription primer, loaded to 10X chips and separated into gel beads in emulsion, where transcripts from individual cells were uniquely barcoded. Barcoded transcripts were reverse transcribed and amplified to generate cDNA libraries. Size selection of the initial cDNA libraries was performed using SPRI beads (Beckman Coulter). After fragmentation and adaptor ligation, libraries were amplified with sample index primers. Following another round of double-sided size selection, the qualities of the final libraries were checked by Agilent Bioanalyzer High Sensitivity Chip. The Illumina Novaseq6000 platform sequenced libraries that passed the final quality control.

### Pre-processing of scRNA-seq data

For droplet-based scRNA-seq, sequenced libraries were demultiplexed and aligned to the mouse reference genome GRCm39 (mm10), with the eGFP sequence added to the reference, using Cell Ranger (v8.0.1). Raw expression matrices were constructed using Read10X function in the 'R' package Seurat (v5.0.3). Before clustering analysis, low-quality cells detected with fewer than 1,000 genes and putative dead cells with high mitochondrial percentage (more than 10% of reads mapped to mitochondrial genes) were discarded. Cells detected with more than 6,000 genes were also considered doublets and removed. For gene-based quality control, genes detected in fewer than three cells were removed from the raw expression matrix. After quality control of unwanted cells and genes, expression matrices were normalized column-wise, dividing the unique molecular identifier (UMI) counts of each gene by the sum of UMI counts for a given cell. Then, scale factor 10,000 was multiplied, and $\log_2$ transformed to yield log counts per million equivalent values.

### Clustering analysis

Clustering and downstream analyses were performed by the 'R' package Seurat (v5.0.3). First, the 2,000 most variable genes for each dataset were identified by the FindVariableFeatures function with options: selection.method = 'vst'. For initial dimensionality reduction, principal component analysis was performed. The top 20 principal components were selected for further downstream analysis, such as uniform manifold approximation and projection for two-dimensional visualization and shared nearest neighbour graph for neighbour detection and cluster identification using the Louvain algorithm. After initial clustering, the small number of contaminating cells and doublet cells were excluded. After removal of the cells, the remaining cells were dimensionally reduced and clustered again, as described above. For the identification of differentially expressed genes across clusters, the FindMarkers function in Seurat was used with the following options: test.use = 'MAST', min.pct = 0.3 and logfc.threshold = 0.3. In merging adult and aged mouse datasets, no batch correction method was used, as no batch effect was observed for clustering.

### Statistical analysis

Sample sizes were chosen on the basis of standard power calculations (with $\alpha = 0.05$ and power of 0.8) and no statistical methods were used to predetermine sample size. Experiments were randomized,

and investigators were blinded to allocation during experiments and outcome assessment. Data were tested for normality using the Shapiro–Wilk and Kolmogorov–Smirnov one-sample test. Parametric or non-parametric statistical tests were used, depending on the data distribution. The statistical significance of differences was determined by two-tailed Student's *t*-test, two-tailed Welch's *t*-test, Brown–Forsythe ANOVA test, two-way ANOVA test, two-way repeated measure ANOVA test, Kruskal–Wallis test, or two-tailed Mann–Whitney *U*-test, two-tailed Tukey's multiple comparison test, two-tailed Sidak's multiple comparison test, two-tailed Dunn's multiple comparison test, two-tailed Dunnett's T3 comparison test, two-tailed model-based analysis of single cell transcriptomics with Bonferroni post-hoc test, and one-tailed Fisher's exact test with false discovery rate correction using the Benjamini–Hochberg method. Statistical analyses were performed using Prism 10 (GraphPad Software, v10.2.3). All data are expressed as mean ± s.e.m. Statistical significance was set at $P < 0.05$.

### Reporting summary

Further information on research design is available in the Nature Portfolio Reporting Summary linked to this article.

## Data availability

The scRNA-seq data of this study are available in the NCBI's Gene Expression Omnibus under accession GSM8493731 (adult mice) and GSM8493732 (aged mice). Source data are provided with this paper.

## Code availability

The MATLAB code for analysing in vivo physiological properties of the scLV, the Arduino code for data analysis of the force-regulated mechanostimulator, the LabVIEW code for data analysis of the force-regulated mechanostimulator, the MATLAB code for data analysis of the force-regulated mechanostimulator and the scRNA-seq codes[77] are available at https://doi.org/10.5281/zenodo.15172410. The LabVIEW program used for pressure and diameter data collection of isolated lymphatic vessels[78] is available at https://doi.org/10.5281/zenodo.8286107. The LabVIEW program used for diameter tracking of isolated lymphatic vessels[79] is available at https://doi.org/10.5281/zenodo.8286119.


70. Weatherall, D. *The Use of Non-Human Primates in Research* (Academy of Medical Sciences, 2006).
71. Polomska, A. K. & Proulx, S. T. Imaging technology of the lymphatic system. *Adv. Drug Deliv. Rev.* **170**, 294–311 (2021).
72. Li, C. X., Patel, S., Auerbach, E. J. & Zhang, X. Dose-dependent effect of isoflurane on regional cerebral blood flow in anesthetized macaque monkeys. *Neurosci. Lett.* **541**, 58–62 (2013).
73. Moore, P. K., Oluyomi, A. O., Babbedge, R. C., Wallace, P. & Hart, S. L. L-NG-nitro arginine methyl ester exhibits antinociceptive activity in the mouse. *Br. J. Pharmacol.* **102**, 198–202 (1991).
74. Ku, T. et al. Elasticizing tissues for reversible shape transformation and accelerated molecular labeling. *Nat. Methods* **17**, 609–613 (2020).
75. Arganda-Carreras, I. et al. Trainable Weka segmentation: a machine learning tool for microscopy pixel classification. *Bioinformatics* **33**, 2424–2426 (2017).
76. Li, K. The image stabilizer plugin for ImageJ. *CMU* http://www.cs.cmu.edu/~kangli/code/Image_Stabilizer.html (2008).
77. Jin, H. scLV code and supplementary data. *Zenodo* https://doi.org/10.5281/zenodo.15172410 (2025).
78. Davis, M. J. Pressure acquisition and control program for quantitative assessment of lymphatic vessel function (version v1). *Zenodo* https://doi.org/10.5281/zenodo.8286108 (2023).
79. Davis, M. J. Diameter tracking program for quantitative assessment of lymphatic vessel contractions. *Zenodo* https://doi.org/10.5281/zenodo.8286120 (2023).



**Acknowledgements** We thank Y.-K. Hong for the *Prox1*–GFP mice. This study was supported by the Institute of Basic Science and funded by the Ministry of Science and ICT, Republic of Korea (IBS-R025-D1-2015) to G.Y.K., and the National Heart, Lung, and Blood Institute grants R01 HL-122578 to M.J.D. and R01 HL143896, R01 HL059157 and R01 HL127402 to D.M.M. from the US National Institutes of Health.


**Author contributions** H.J., J.-H.Y., D.M.M. and G.Y.K. conceived and designed the study. H.J., J.-H.Y. and S.P.H. performed most of the experiments and generated the figures. Y.S.H. and H.-S.P. made the force-regulated mechanostimulator. H.J., J.-H.Y., M.J.D., D.M.M. and G.Y.K. wrote the manuscript with contributions from S.P.H. and M.J.Y. under the supervision of M.J.D., D.M.M. and G.Y.K. H.J., J.-H.Y., S.P.H., M.J.Y., J.C., H. J. Kang, S.E.B., C.J., J.J., M.J.D., D.M.M. and G.Y.K. analysed and interpreted the data and generated the figures. H.J. and J.-H.Y. performed scRNA-seq with contributions from M.J.Y. H.J., J.-H.Y. and M.J.Y. analysed the scRNA-seq datasets. H. J. Kim and M.J.D. performed and analysed the results of experiments using ex vivo-isolated scLVs. H.J., J.-H.Y., S.P.H., C.J. and M.J.Y. actively discussed the experiments and the results under the supervision of M.J.D., D.M.M. and G.Y.K. J.S., J.W., K.S.L., C.-Y.J. and Y.L. prepared and analysed the primate tissue samples. J.J. oversaw the care of mice. G.Y.K. supervised and directed the project.

**Competing interests** The authors declare no competing interests.

**Additional information**


**Supplementary information** The online version contains supplementary material available at https://doi.org/10.1038/s41586-025-09052-5.



**Correspondence and requests for materials** should be addressed to Gou Young Koh.



**Peer review information** *Nature* thanks the anonymous reviewers for their contribution to the peer review of this work. Peer reviewer reports are available.



**Reprints and permissions information** is available at http://www.nature.com/reprints.

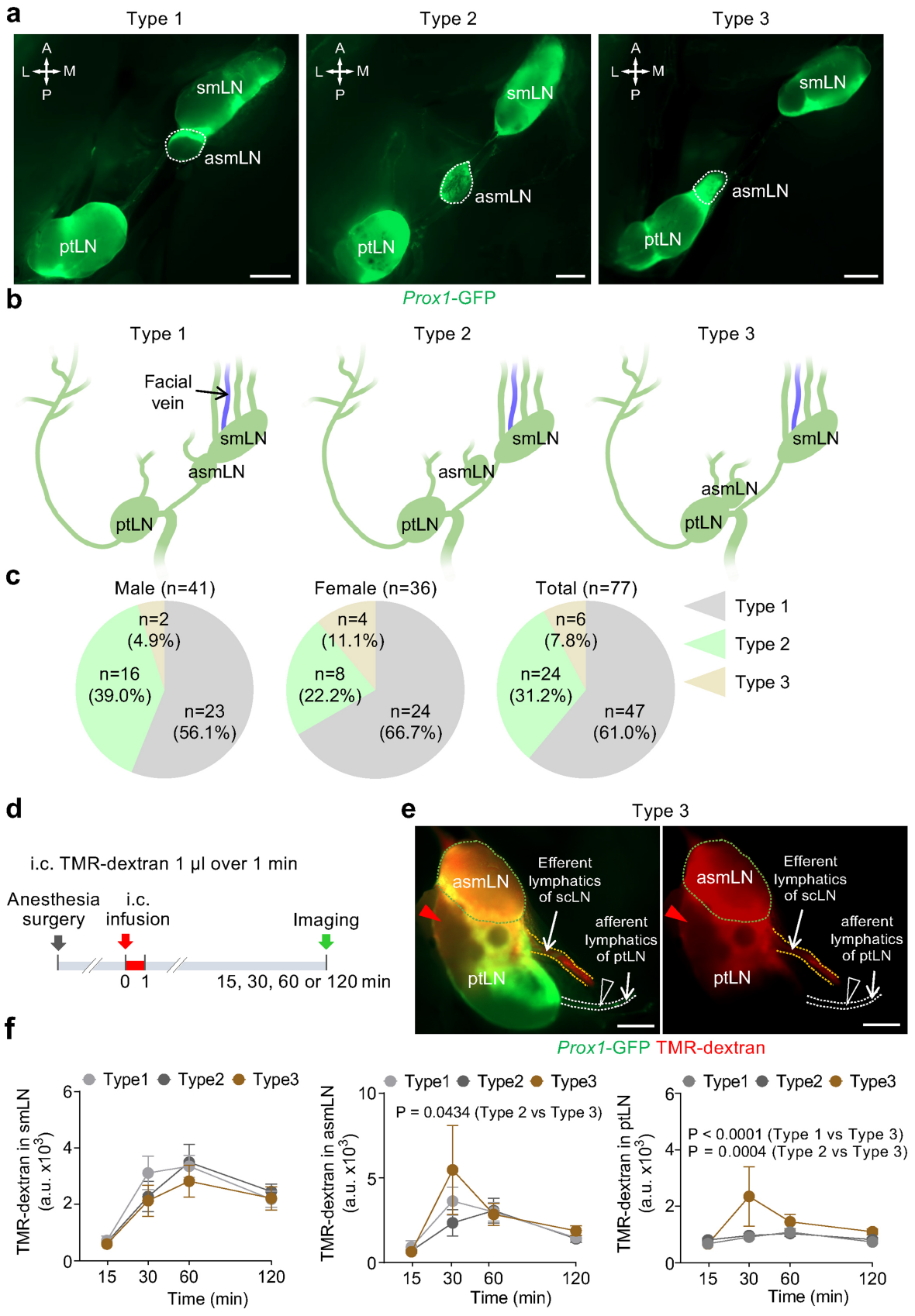


**Extended Data Fig. 1** | See next page for caption.

**Extended Data Fig. 1 | Variability in relative positions of superficial cervical lymph nodes. a-c**, Fluorescence images and drawings of the three types of superficial cervical lymph nodes defined by the relationship of the accessory submandibular lymph node (asmLN, white dashed line) to neighboring lymph nodes in *Prox1*-GFP mice (**a**,**b**). Type 1, asmLN is fused with the submandibular lymph node (smLN). Type 2, asmLN is separated from both smLN and the parotid lymph node (ptLN). Type 3, asmLN is fused with ptLN. Anatomical positions are indicated in the top left corner (**a**): A, anterior; P, posterior; M, medial; L, lateral. Scale bars, 1 mm. Drawings illustrate the relationship of asmLN to other lymph nodes (**b**). Pie charts showing the percentage of the three types of asmLN in male ($n = 41$), female ($n = 36$), and all ($n = 77$) mice (**c**). **d-f**, Sequence of intracisternal (i.c.) infusion of 1.0 µl TMR-dextran over 1 min into *Prox1*-GFP mice followed 15, 30, 60, or 120 min later by measurement of TMR-dextran fluorescence in superficial cervical lymph nodes (**d**). Fluorescence images representative of $n = 7$ mice showing TMR-dextran distribution in asmLN (green dashed line) and ptLN components of a Type 3 superficial cervical lymph node at 30 min after intracisternal infusion (**e**). TMR-dextran fluorescence in (i) asmLN and the adjacent region of ptLN (red arrowheads) and in (ii) efferent lymphatics (orange dashed lines) but not in (iii) afferent lymphatics of ptLN (blank arrowheads) at 30 min after intracisternal infusion (**e**). Scale bars, 500 µm. Measurements of temporal changes in TMR-dextran fluorescence in Type 1, Type 2, and Type 3 superficial cervical lymph nodes after intracisternal infusion (**f**). Each dot represents the mean value of superficial cervical lymph nodes on one side of $n = 3$-5 mice for 15 min, $n = 7$-19 mice for 30 min, $n = 10$-15 mice for 60 min, and $n = 6$-17 mice for 120 min. Error bars indicate mean ± s.e.m. a.u., arbitrary unit. *P* values calculated by two-way ANOVA followed by Tukey's multiple comparison test.

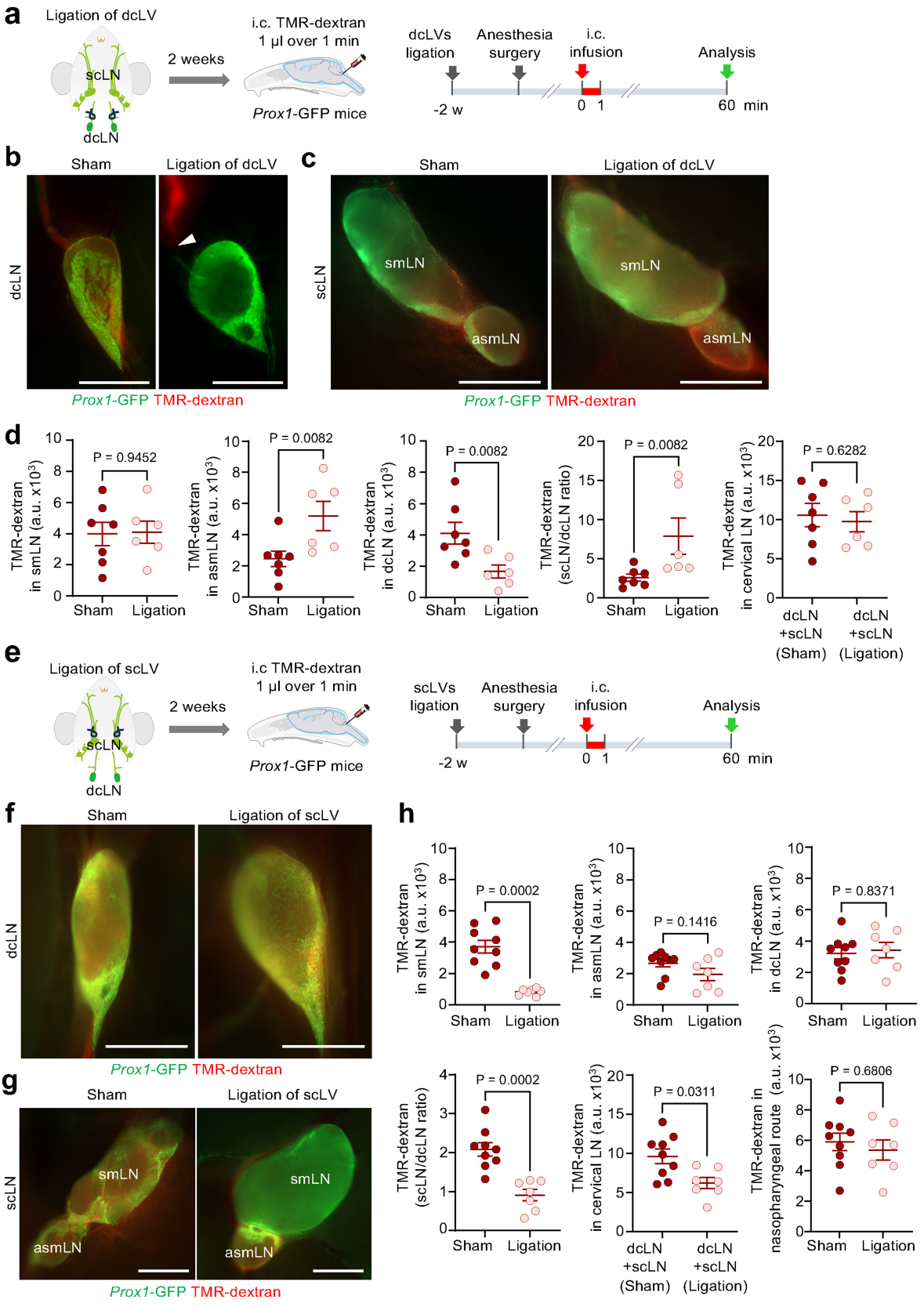


**Extended Data Fig. 2** | See next page for caption.

**Extended Data Fig. 2 | Compensatory redistribution of CSF drainage after ligation of either deep or superficial cervical lymphatics. a**, Sequence for intracisternal (i.c.) infusion of 1 µl TMR-dextran over 1 min into *Prox1*-GFP mice 2 wk after ligation of deep cervical lymphatics (dcLV) on both sides. The fluorescence intensity of the deep cervical (dcLN) and superficial cervical lymph nodes (scLN) was measured at 60 min after TMR-dextran infusion. **b,c**, Fluorescence images of dcLN, submandibular lymph node (smLN, left) and accessory submandibular lymph nodes (asmLN, right) after ligation of the deep cervical lymphatics (dcLV). TMR-dextran accumulated in the dcLN in the sham group but not in the ligation group. However, TMR-dextran fluorescence in the asmLN is stronger in the ligation group than in the sham group. Scale bars, 1 mm. Representative of $n = 6$-7 mice from three independent experiments. **d**, Comparison of TMR-dextran signal intensity in smLN, asmLN, dcLN, scLN/dcLN ratio, and cervical LN. Compensation in CSF drainage among cervical lymph nodes at 2 wk after ligation of deep cervical lymphatics (dcLV) shown by similar CSF drainage to cervical lymph nodes (sum of TMR-dextran fluorescence intensity for superficial and deep cervical lymph nodes) without ligation (sham, left) and with ligation (right) and increased ratio of TMR-dextran fluorescence in superficial to deep cervical lymph nodes with ligation. Each dot is the value for one mouse. Sham ($n = 7$ mice), dcLV ligation ($n = 6$ mice) from three independent experiments. Error bars indicate mean ± s.e.m. a.u., arbitrary unit. *P* values calculated by two-tailed Mann-Whitney *U*-test. **e**, Sequence for intracisternal (i.c.) infusion of 1 µl TMR-dextran over 1 min into *Prox1*-GFP mice at 2 weeks after ligation of superficial cervical lymphatics (scLV) on both sides. The fluorescence intensity of the deep cervical (dcLN) and superficial cervical lymph nodes (scLN) was measured at 60 min after TMR-dextran infusion. **f,g**, Strong TMR-dextran fluorescence (red) in a deep cervical lymph node (dcLN, **f**) and accessory submandibular lymph node (asmLN, **g**), with or without (sham) ligation of scLV. However, red fluorescence is evident in a submandibular node (smLN) in the sham but not after scLV ligation (**g**). Scale bars, 1 mm. Representative images of $n = 7$-9 mice from three independent experiments. **h**, Measurements of TMR-dextran fluorescence in smLN, asmLN, and dcLN with or without scLV ligation. Also shown are corresponding calculated values for the ratio of superficial to deep lymph nodes (scLN/dcLN), sum of deep and superficial cervical lymph nodes (dcLN + scLN), and nodes downstream of the nasopharyngeal lymphatic drainage route (asmLN + dcLN, as shown in Fig. 1). ScLV ligation resulted a large reduction in TMR-dextran in smLN (and corresponding reduction in dcLN + scLN) but no reduction in asmcLV or dcLN due to continued patency of the nasopharyngeal route. Each dot is the value for one mouse. Sham ($n = 9$ mice) and scLV ligation ($n = 7$ mice) from three independent experiments. Error bars indicate mean ± s.e.m. a.u., arbitrary unit. *P* values calculated by two-tailed Mann-Whitney *U*-test.

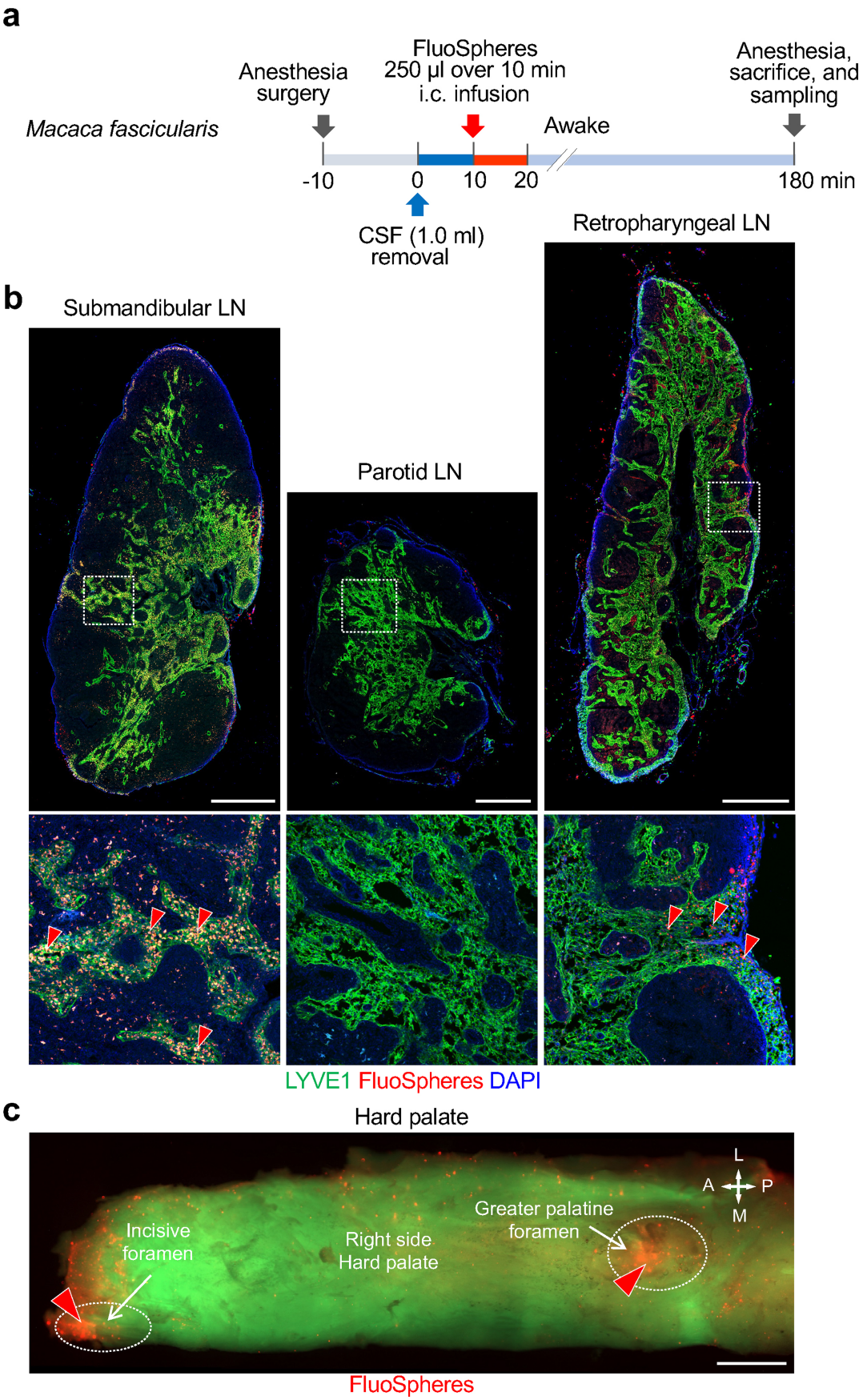


**Extended Data Fig. 3** | See next page for caption.

**Extended Data Fig. 3 | FluoSpheres distribution in cervical lymph nodes and hard palate of monkeys after infusion into cisterna magna. a**, Sequence of intracisternal (i.c.) infusion of FluoSpheres into *Macaca fascicularis* monkeys at 2.5 ml over 10 min followed by measurement of FluoSpheres in cervical lymph nodes and hard palate at 180 min. Before infusion, 1 ml of CSF was removed at the cisterna magna over 10 min. Anesthesia was administered until the end of the infusion and then readministered at 180 min. **b**, Immunofluorescence images showing the distribution of FluoSpheres (red) and LYVE1$^+$ vessels in submandibular, parotid, and retropharyngeal lymph nodes (LN). White dashed line boxes mark regions enlarged in panels below. Red arrowheads mark regions with abundant FluoSpheres in lymph node medullary sinusoids. Scale bars, 1 mm. Representative of $n = 2$ monkeys from two independent experiments. **c**, Fluorescence image showing the distribution of FluoSpheres (red) in the right-side of the hard palate of a *Macaca fascicularis* monkey. FluoSpheres (red arrowheads) are abundant near the incisive and greater palatine foramina (white dashed ellipses) in the hard palate. Scale bar, 5 mm. Representative of $n = 2$ monkeys from two independent experiments. Anatomical positions are indicated in the top right corner: A, anterior; P, posterior; M, medial; L, lateral.

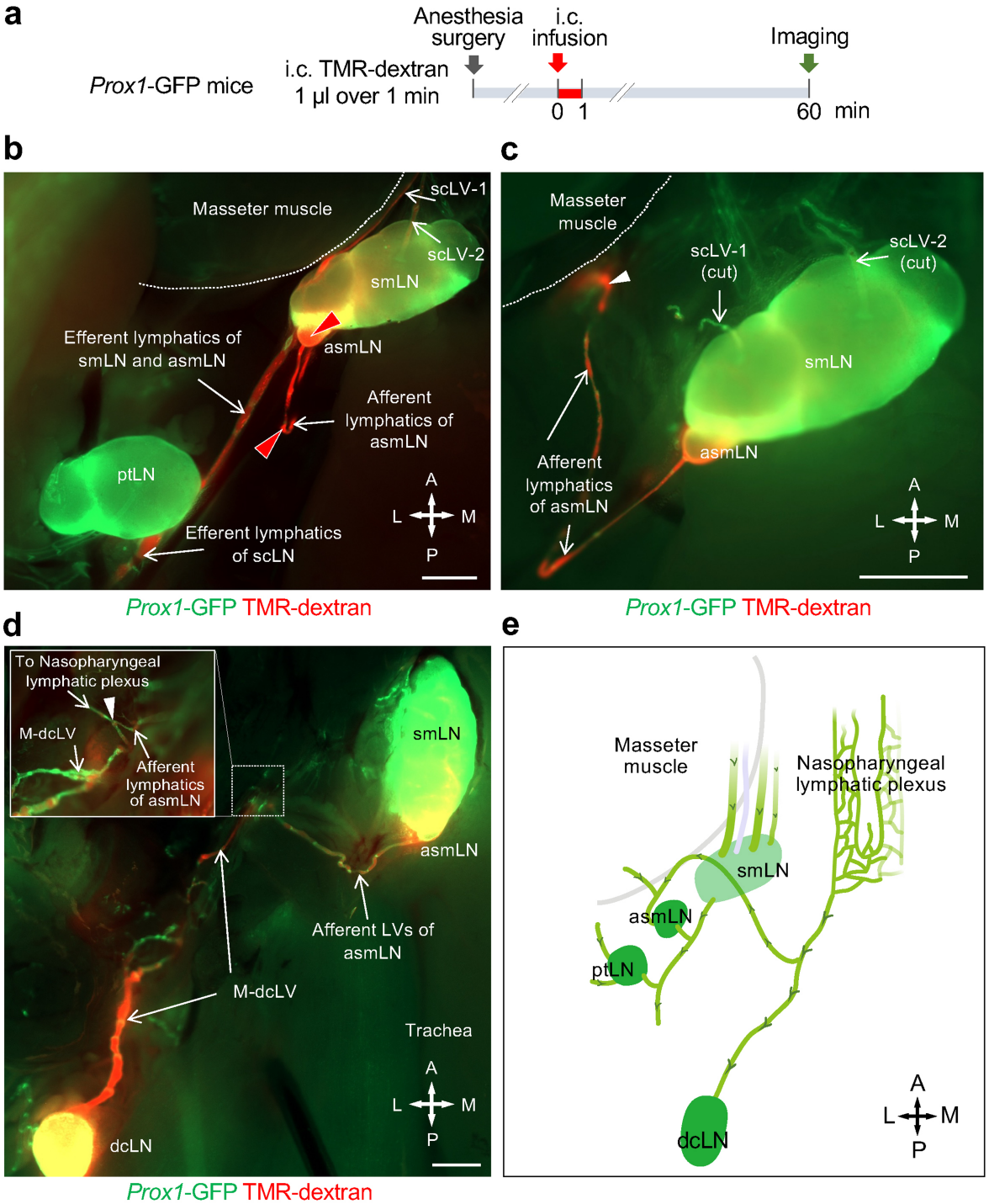


**Extended Data Fig. 4 | Lymphatic connection of nasopharyngeal lymphatic plexus to accessory submandibular lymph node. a**, Sequence of intracisternal (i.c.) infusion of 1.0 µl TMR-dextran over 1 min into *Prox1*-GFP mice followed by imaging of TMR-dextran in superficial cervical lymphatics and lymph nodes 60 min later. **b**,**c**, Fluorescence image of *Prox1*-GFP mouse showing TMR-dextran (red) in superficial cervical lymphatics scLV-1 and scLV-2, submandibular (smLN) and accessory submandibular (asmLN) lymph nodes, and efferent lymphatics from these lymph nodes but not in the parotid lymph node (ptLN) (**b**). Lymphatics near the masseter muscle (white arrowhead) en route to asmLN (**c**). White dashed lines mark the border of the masseter muscle. Scale bars, 1 mm. Representative of $n = 4$ mice from four independent experiments. **d**, Fluorescence image showing the connections of medial deep cervical lymphatics (M-dcLV) and lymphatics that drain into the accessary submandibular lymph node (asmLN). White dashed line boxes marks the connecting point (white arrowhead) and the enlargement of this region. TMR-dextran fluorescence (red) is strong in M-dcLV and afferent lymphatics of asmLN and in the deep cervical lymph node (dcLN) and asmLN. Scale bars, 1 mm. Representative of $n = 4$ mice from four independent experiments. **e**, Drawing summarizing the lymphatic connections of the nasopharyngeal lymphatic plexus and the downstream accessory submandibular (asmLN) and deep cervical (dcLN) lymph nodes. The submandibular (smLN) and parotid (ptLN) lymph nodes are not downstream of the nasopharyngeal lymphatic plexus. Anatomical positions are indicated in the bottom right corner: A, anterior; P, posterior; M, medial; L, lateral.

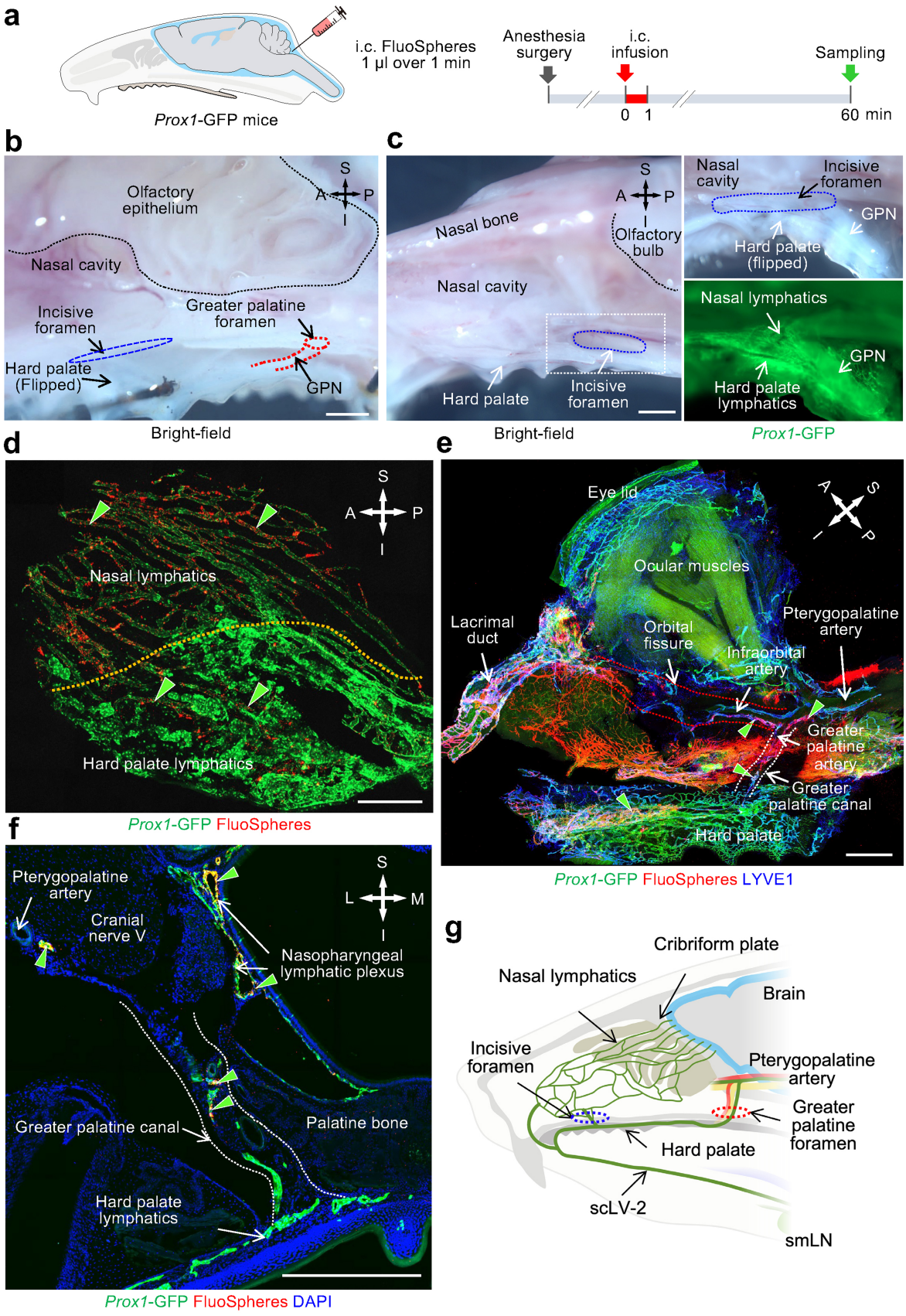


**Extended Data Fig. 5** | See next page for caption.

**Extended Data Fig. 5 | CSF drainage through two lymphatic routes to hard palate lymphatics en route to the submandibular lymph node. a**, Sequence of intracisternal (i.c.) infusion of 1.0 µl FluoSpheres over 1 min into *Prox1*-GFP mice followed by imaging of FluoSphere distribution in the nasal cavity and hard palate 60 min later. **b**, Brightfield microscopic image showing the anatomical location of the incisive foramen (blue dashed elliptical circle), greater palatine foramen (red dashed circle), and greater palatine nerve (GPN, red dashed lines). The black dashed line marks the border of the olfactory epithelium. Scale bar, 1 mm. Representative of $n = 3$ mice from three independent experiments. **c**, Brightfield, fluorescence, and immunofluorescence images of whole mounts showing connections between lymphatics in the nasal cavity and hard palate through the incisive foramen. Brightfield image showing the anatomical location of the incisive foramen (blue dashed elliptical circle). White dashed line box is enlarged in brightfield and fluorescence images in the right two panels that show connections between lymphatics in the nasal mucosa and hard palate through the incisive foramen. The black dashed line marks the border of the intracranial olfactory bulb. Scale bar, 1 mm. Representative of $n = 4$ mice from three independent experiments. **d**, Immunofluorescence image showing FluoSpheres (red) within lymphatics in the nasal mucosa and hard palate (green arrowheads). The orange dashed line marks the boundary between lymphatics in the nasal mucosa and hard palate. Scale bar, 200 µm. Representative of $n = 4$ mice from three independent experiments. **e**, Immunofluorescence image of whole mount showing FluoSpheres (red) and lymphatics (*Prox1*-GFP, green; LYVE1, blue) in the periorbital area and hard palate. FluoSphere fluorescence is strong in lymphatics along the pterygopalatine artery, infraorbital artery in the orbital fissure, greater palatine artery in the greater palatine canal, and hard palate (green arrowheads). Red dashed lines mark the lymphatic pathway from the orbital fissure to periorbital lymphatics. White dashed lines mark the lymphatic pathway from descending branch of pterygopalatine artery through the greater palatine canal to the hard palate plexus. Scale bar, 1 mm. Representative of $n = 4$ mice from three independent experiments. **f**, Immunofluorescence image of coronal section of the greater palatine canal showing FluoSpheres (red) in lymphatics (green) along the pterygopalatine artery, in the greater palatine canal, and in the nasopharyngeal lymphatic plexus (green arrowheads). The white dashed lines mark the lymphatic pathway from the greater palatine canal to the hard palate. Scale bar, 500 µm. Representative of $n = 4$ mice from three independent experiments. **g**, Drawing of two lymphatic routes for CSF to reach the hard palate lymphatic plexus, superficial cervical lymphatic scLV-2, and submandibular lymph node (smLN): (1) Meningeal lymphatics that cross the cribriform plate join nasal lymphatics and then traverse the incisive foramen to join the hard palate plexus. (2) Meningeal lymphatics along the pterygopalatine artery travel with the greater palatine artery through the greater palatine canal and join the hard palate lymphatic plexus. Lymphatics in the hard palate plexus carry CSF to scLV-2 en route to the submandibular lymph node. Anatomical positions are indicated in the top right corner: S, superior; I, inferior; A, anterior; P, posterior; M, medial; L, lateral.

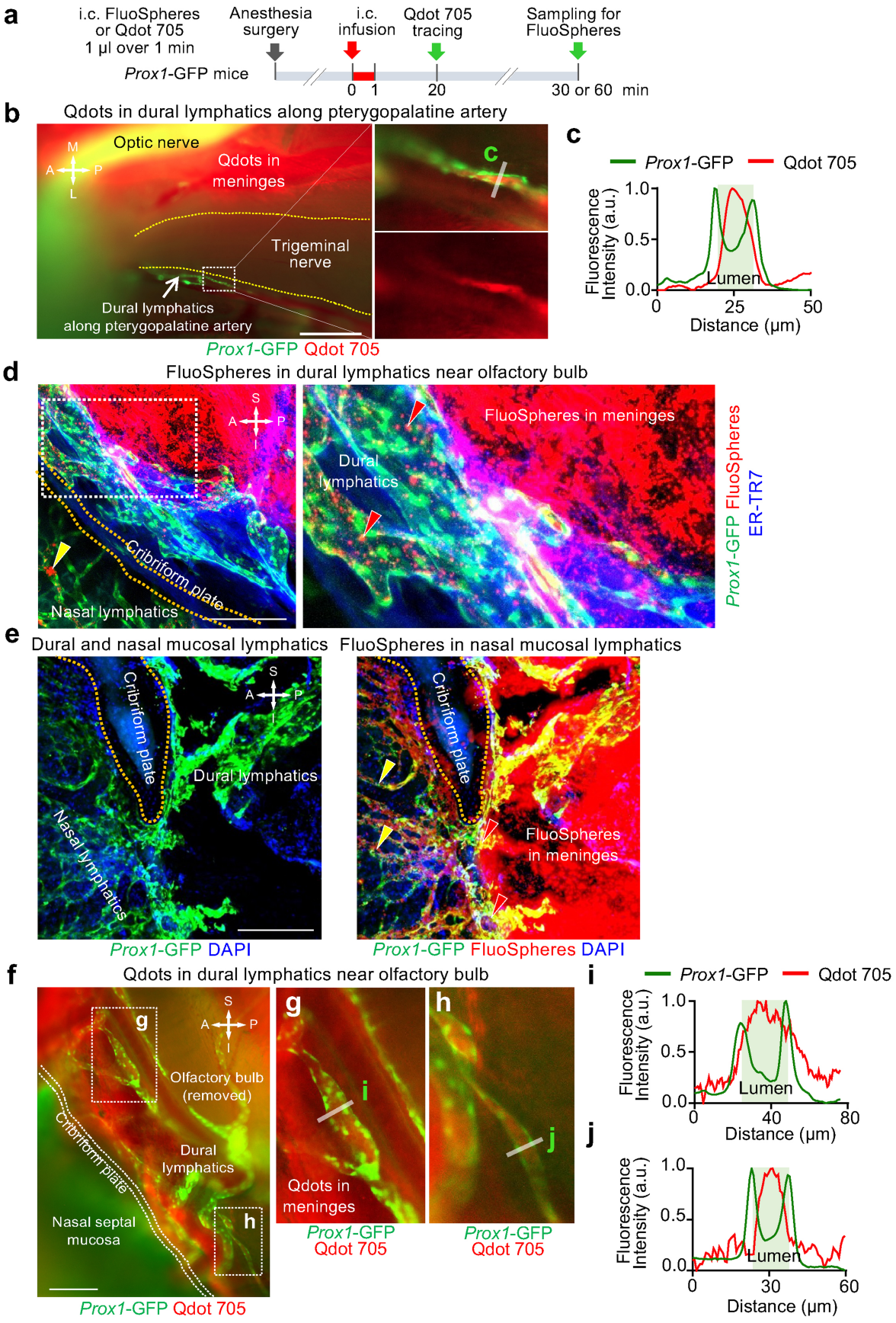


**Extended Data Fig. 6** | See next page for caption.

**Extended Data Fig. 6 | Dural lymphatics containing tracers after infusion into the CSF. a**, Sequence of intracisternal (i.c.) infusion of 1.0 µl FluoSpheres or Qdot 705 over 1 min into *Prox1*-GFP mice followed by imaging of the tracer distribution in dural lymphatics near pterygopalatine artery or cribriform plate 20, 30 or 60 min later. **b**,**c**, Fluorescence images of Qdot 705 in dural lymphatics along pterygopalatine artery (**b**). Trigeminal nerve is outlined by yellow dashed line. Region of dashed line box is enlarged in right two panels, upper showing *Prox1*-GFP and Qdot 705 and lower showing only Qdot 705. Fluorescence intensity profiles of *Prox1*-GFP and Qdot 705 in the dural lymphatic (gray bar in **b**) is shown in **c**. Scale bar, 500 µm. Representative of $n = 3$ mice from three independent experiments. **d,e**, Confocal microscopic images of whole mounts showing a sagittal view of lymphatics near the cribriform plate (yellow dashed line). Dashed line box in **d-left** is enlarged in **d-right**. Panel **e** shows a region near **d** without (**e-left**) and with (**e-right**) the red channel (FluoSpheres). After intracisternal infusion, FluoSpheres (red) are located in dural lymphatics (red arrowheads), nasal mucosal lymphatics (yellow arrowheads), and trapped in the meninges (probably arachnoid layer) bordering the SAS. Staining of meninges by anti-mouse fibroblast antibody ER-TR7 (blue). Scale bars, 200 µm. Representative of $n = 6$ mice from three independent experiments. **f-j**, Fluorescence images showing Qdot 705 in dural lymphatics near the cribriform plate (white dashed lines). Regions in **f** marked by dashed line boxes are enlarged in right two panels (**g** and **h**). Fluorescence intensity profiles of *Prox1*-GFP and Qdot 705 (**i** and **j**) in dural lymphatics (gray bars in **g** and **h**). Scale bar, 1 mm. Representative of $n = 3$ mice from three independent experiments. Anatomical positions are indicated in the top right or left corner: S, superior; I, inferior; A, anterior; P, posterior; M, medial; L, lateral.

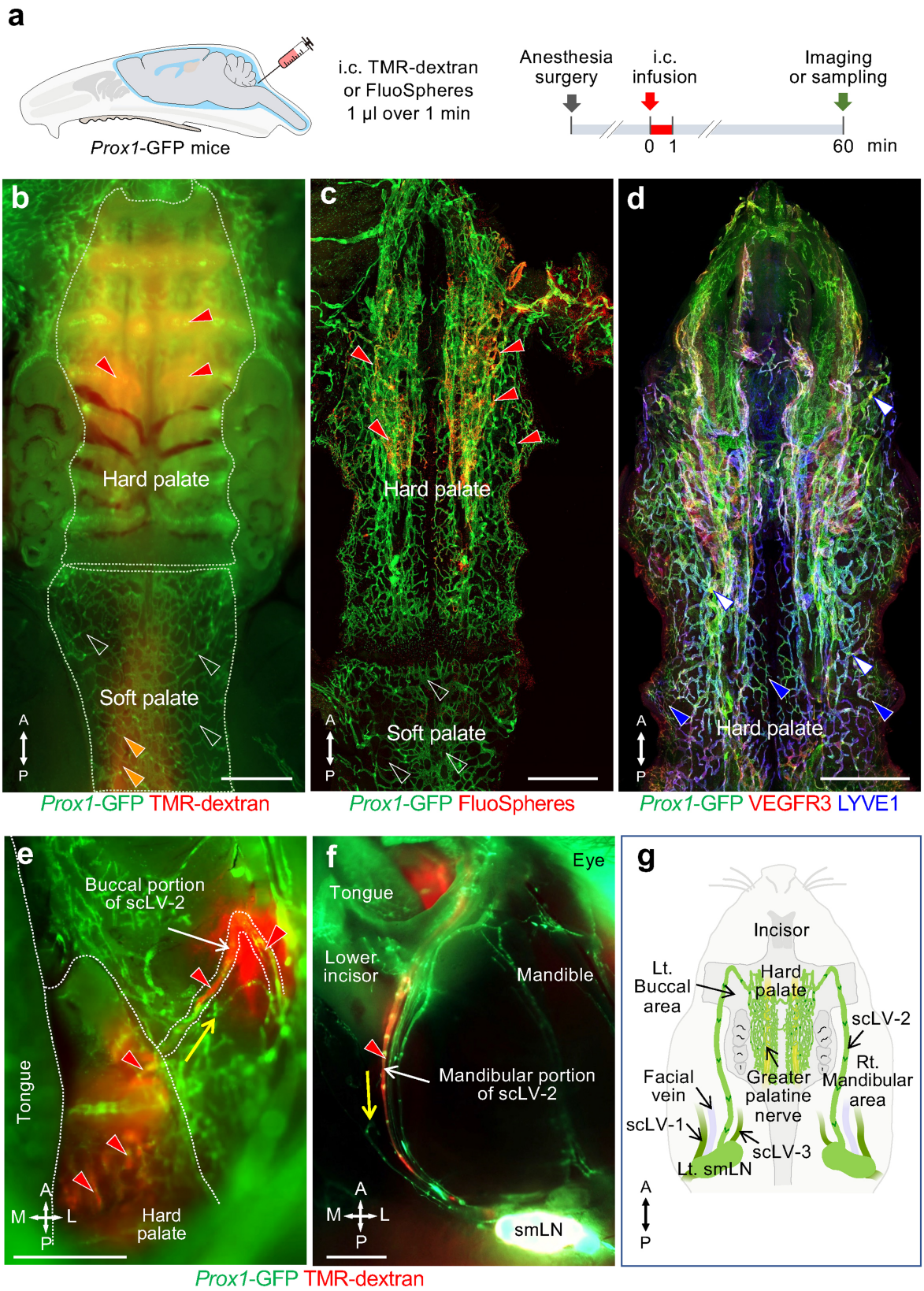


**Extended Data Fig. 7** | See next page for caption.

**Extended Data Fig. 7 | CSF drainage through the hard palate lymphatic plexus to the submandibular lymph node. a**, Sequence of intracisternal (i.c.) infusion of 1.0 µl TMR-dextran or FluoSpheres over 1 min into *Prox1*-GFP mice followed by analysis of the distribution of the tracer in the hard palate lymphatic plexus at 60 min. **b**-**d**, Fluorescence images showing the distribution of TMR-dextran or FluoSpheres (red) in whole mounts of the hard palate and soft palate of *Prox1*-GFP mice (**b**,**c**). White dashed lines mark border between hard palate and soft palate (**b**). Tracer fluorescence (red) is strong in hard palate lymphatic plexus (red arrowheads) but not in soft palate lymphatic plexus (**b**,**c** white empty arrowheads). Orange arrowheads mark the faint TMR-dextran fluorescence in the nasopharyngeal lymphatic plexus (**b**). Hard palate lymphatic plexus of *Prox1*-GFP mouse stained for VEGFR3 (red) and LYVE1 (blue) (**d**). Lymphatic valves (**d**, white arrowheads). Initial lymphatics (**d**, blue arrowheads) are distributed in the medial and lateral sides of hard palate. Scale bars, 1 mm. Representative of $n = 5$ mice from three independent experiments. **e**,**f**, Images showing TMR-dextran fluorescence (red arrowheads) in the buccal (**e**) and mandibular (**f**) portions of superficial cervical lymphatic scLV-2 between the hard palate lymphatic plexus and submandibular lymph node. White dashed lines (**e**) outline border of hard palate, tongue, and buccal portion of scLV-2. Yellow arrows mark the direction of CSF outflow. Scale bars, 1 mm. Representative of $n = 5$ mice from three independent experiments. **g**, Drawing of downstream connection of hard palate plexus to submandibular lymph node (smLN) through buccal and mandibular portions of scLV-2 for CSF drainage. Locations of scLV-1 and scLV-3 are shown for comparison. Left (Lt.), Right (Rt.). Anatomical positions are indicated in the bottom left corner: A, anterior; P, posterior; M, medial; L, lateral.

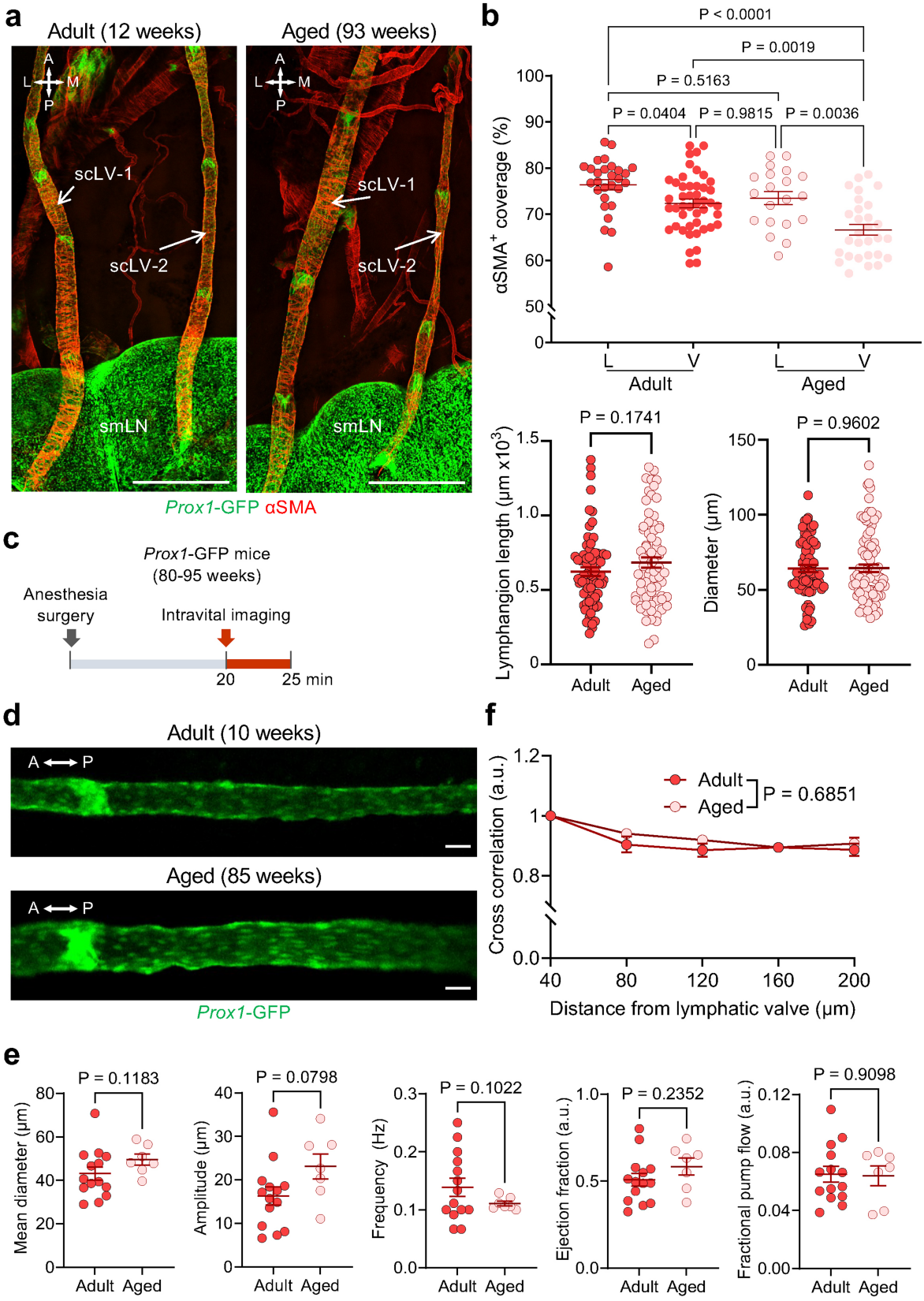


**Extended Data Fig. 8** | See next page for caption.

**Extended Data Fig. 8 | Ageing-related changes in smooth muscle coverage and functional properties of superficial cervical lymphatics in vivo.** **a**, Immunofluorescence images showing smooth muscle coverage in superficial cervical lymphatics (scLV) of aged *Prox1*-GFP mice (93 weeks) and in younger adults (12 weeks). α-smooth muscle actin (αSMA), Submandibular lymph node (smLN). Scale bars, 500 μm. Representative of $n$ = 12-13 mice from three independent experiments. **b**, Measurements showing less circular smooth muscle coverage (α-smooth muscle actin, αSMA) in the peri-valvular region (V) of superficial cervical lymphatics in aged *Prox1*-GFP mice (80–95 weeks) than in younger adults (10–12 weeks) but no difference in coverage of the middle of lymphangions (L) (upper). Similarities of lymphangion length and diameter at the two ages are also shown (lower). Each dot is the value for one lymphangion. $n$ = 13 (adult), $n$ = 12 (aged) mice per group from four independent experiments. Error bars indicate mean ± s.e.m. $P$ values calculated by two-tailed unpaired t test with Welch's correction or Brown-Forsythe ANOVA test followed by Dunnett's T3 multiple comparison test. **c**, Sequence of surgical exposure and intravital imaging of superficial cervical lymphatics scLV-1 from adult (10–12 weeks) and aged (80–95 weeks) *Prox1*-GFP mice. Intravital imaging began after a 20-min stabilization period and lasted 5 min. **d**, Intravital images of superficial cervical lymphatic scLV-1 of adult (10 weeks) and aged (85 weeks) *Prox1*-GFP mice. Scale bars, 20 μm. Representative of $n$ = 7-14 mice from four independent experiments. **e**, Measurements showing no age-related difference in mean diameter, contraction amplitude, frequency of spontaneous contraction, ejection fraction, or fractional pump flow of scLV-1 from aged *Prox1*-GFP mice (80–95 weeks) and younger adults (10–12 weeks). Each dot is the value for one mouse. $n$ = 14 (adult), $n$ = 7 (aged) mice of both sexes per group from four independent experiments. Error bars indicate mean ± s.e.m. a.u., arbitrary unit. $P$ values calculated by two-tailed unpaired t test with Welch's correction. **f**, Measurements of synchronization of spontaneous contractions and relaxations within a lymphangion assessed by cross-correlation of changes in diameter at five locations in superficial cervical lymphatics scLV-1 spaced 40 μm to 200 μm away from a valve in aged (80–95 weeks) and younger adult (10–12 weeks) *Prox1*-GFP mice. Each dot is the value for one mouse and $n$ = 8 (adult), $n$ = 7 (aged) mice for both sexes from three independent experiments. Error bars indicate mean ± s.e.m. $P$ values calculated by two-way ANOVA test. The $P$ value represents the significance of the interaction between cross-correlation and the measurement location. Anatomical positions are indicated in the top left corner: A, anterior; P, posterior; M, medial; L, lateral.

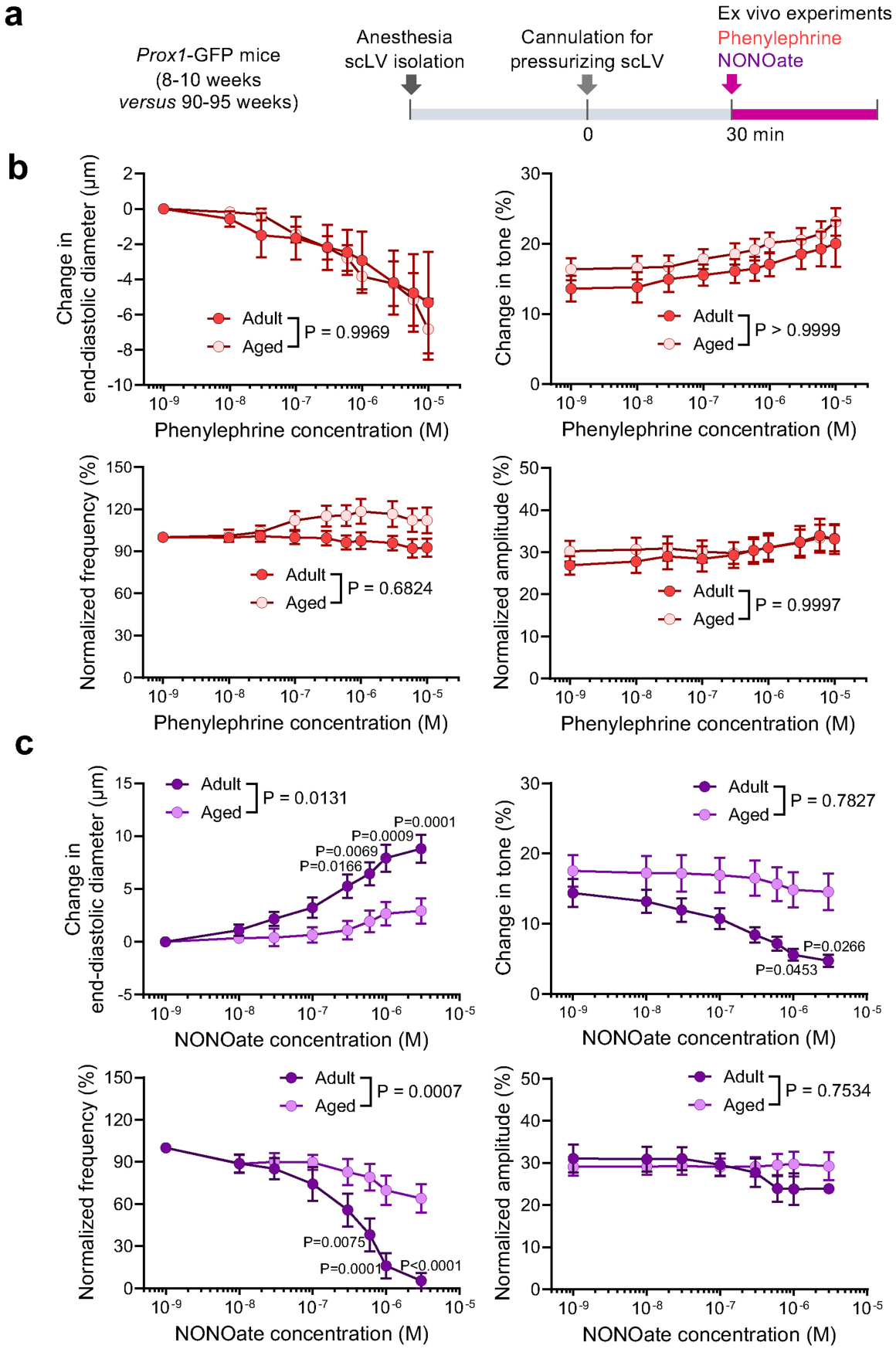


**Extended Data Fig. 9** | See next page for caption.

**Extended Data Fig. 9 | Ageing-related reduction in response of isolated superficial cervical lymphatics to NONOate but not to phenylephrine.** **a**, Sequence of experiments of superficial cervical lymphatics scLV-1 or scLV-2 removed from *Prox1*-GFP mice at age 8–10 weeks (adult) and 90–95 weeks (aged), cannulated, pressurized, and then exposed ex vivo to phenylephrine or NONOate. **b**, Comparison of response to phenylephrine measured by changes in end-diastolic diameter, tone, normalized frequency, and amplitude of scLV-1 and scLV-2 after removal from adult (8–10 weeks, $n = 9$) and aged (90–95 weeks, $n = 14$) *Prox1*-GFP mice. No significant age-related differences were found. Each dot is the value for one mouse of either sex from three independent experiments. Error bars indicate mean ± s.e.m. *P* values calculated by two-way ANOVA test followed by two-tailed Sidak's multiple comparison test. The *P* values represent the significance of the interaction between phenylephrine concentration and scLV from adult or aged mice. **c**, Comparison of response to NONOate reflected by changes in end-diastolic diameter, tone, normalized frequency, and amplitude of scLV-1 and scLV-2 from adult (8–10 weeks, $n = 9$) and aged (90–95 weeks, $n = 14$) *Prox1*-GFP mice. Ageing-related differences in concentration-dependent NONOate-induced end-diastolic diameter and normalized frequency were significant. Each dot is the value for one mouse of either sex from three independent experiments. Error bars indicate mean ± s.e.m. *P* values calculated by two-way ANOVA test followed by two-tailed Sidak's multiple comparison test. The *P* values represent the significance of the interaction between NONOate concentration and scLV from adult or aged mice.

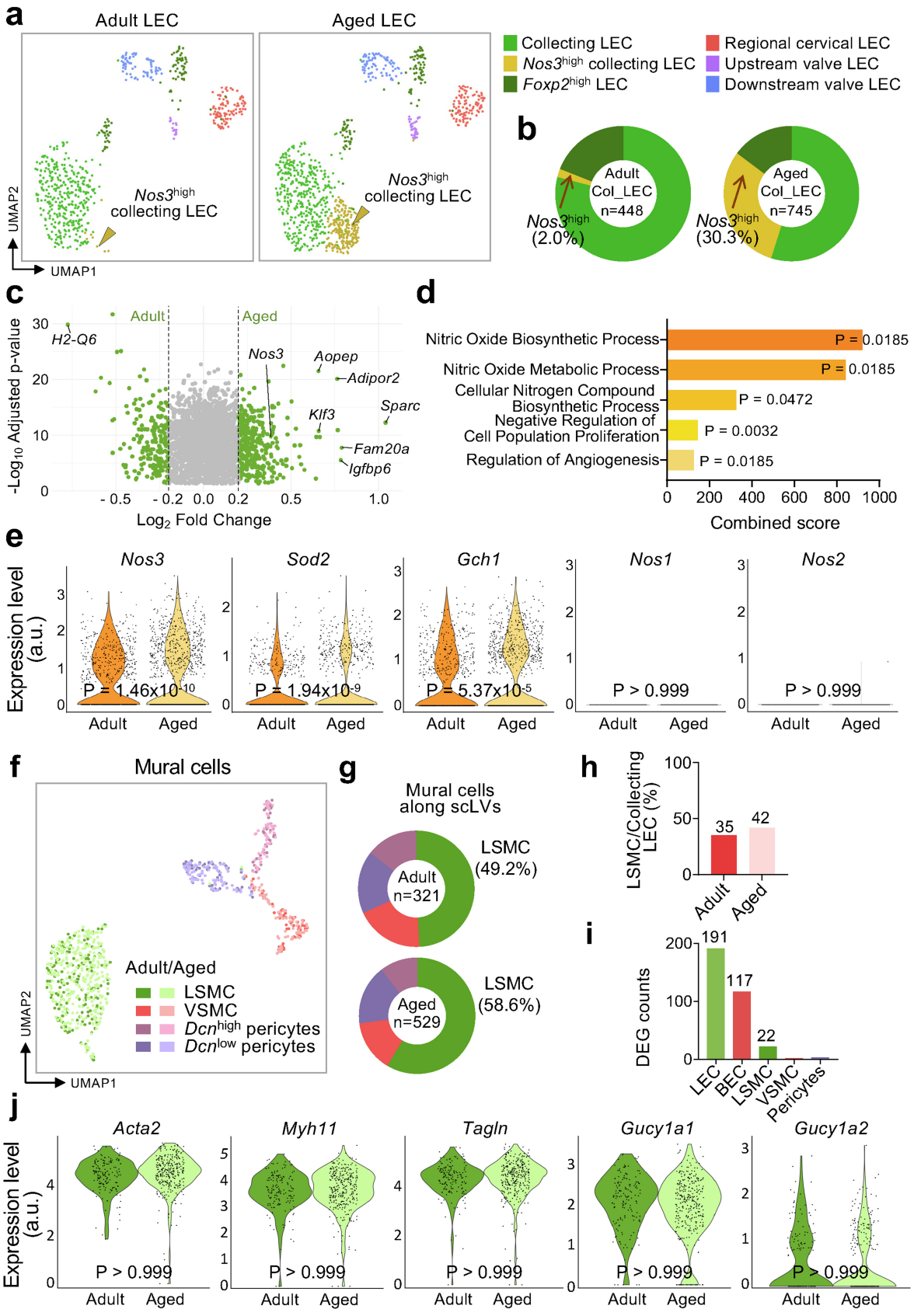


**Extended Data Fig. 10** | See next page for caption.

**Extended Data Fig. 10 | Ageing-related transcriptomic changes in superficial cervical lymphatics. a**, Uniform manifold approximation and projection (UMAP) plot of single-cell gene expression (scRNA-seq) showing six subclusters of lymphatic endothelial cells (LEC) isolated from superficial cervical lymphatics scLV-1 and scLV2 proximal to and around submandibular lymph nodes of adult (12 weeks) and aged (93 weeks) mice. Gold arrowheads mark the *Nos3*$^{high}$ collecting LEC subcluster that is greatly increased in aged mice. **b**, Pie charts showing the 15-fold enlargement of the *Nos3*$^{high}$ LEC subcluster in collecting LEC from aged mice (745 cells) compared collecting LEC from adult mice (448 cells). The other LEC subclusters do not show this change. Values based on scRNA-seq gene expression analysis of scLV-1 and scLV2 in **a**. **c**, Volcano plot showing 2,624 differentially expressed genes between adult and aged LECs. Positive values of Log2 fold change indicate genes upregulated in aged LECs, while negative values indicate genes with higher expression in adult LECs. Gray dots indicate genes with Log2 fold change absolute values less than 0.2, while green dots indicate genes with absolute values greater than 0.2. *P* values calculated by two-tailed MAST with Bonferroni post hoc test. **d**, Bar graphs showing five terms from Gene Ontology (GO) analysis of *Nos3*$^{high}$ collecting LEC indicating the largest enrichment of nitric oxide-related gene functions. GO enrichment was assessed using Enrichr. *P* values calculated using one-tailed Fisher's exact test, with FDR correction using the Benjamini-Hochberg method. Complete dataset for the GO term analysis is presented in Supplementary Table 2. **e**, Violin plots showing greater expression of *Nos3*, *Sod2*, and *Gch1* genes in LEC of aged mice but no detected expression of *Nos1* and *Nos2* genes in LEC of either younger adults or aged mice. *P* values calculated by two-tailed MAST with Bonferroni post hoc test. **f-i**, Uniform manifold approximation and projection (UMAP) plot of gene expression in mural cells from superficial cervical lymphatics showing four subclusters that are similar in younger adult (12 weeks, n = 321 cells analyzed) and aged (93 weeks, n = 529 cells analyzed) mice (**f**). Pie charts showing similar proportions of lymphatic smooth muscle cells (LSMC), vascular smooth muscle cells (VSMC), *Dcn*$^{high}$ pericytes, and *Dcn*$^{low}$ pericytes in younger adults and aged mice (**g**). Bar graph comparing the percentage of LSMC relative to the number of collecting lymphatic endothelial cells (*Apoe*$^{+}$*Eng*$^{+}$*Bgn*$^{+}$) from younger adult and aged mice (**h**). Number of differentially expressed genes between aged mice and younger adults in lymphatic endothelial cells (LEC), blood endothelial cells (BEC), LSMC, VSMC, and pericytes (**i**). **j**, Violin plots showing the absence of ageing-related gene expression differences in lymphatic smooth muscle cells of three smooth muscle markers (*Acta2*, *Myh11*, *Tagln*) and two downstream guanylate cyclases (*Gucy1a1*, *Gucy1a2*) of the nitric oxide pathway. *P* values calculated by two-tailed MAST with Bonferroni post hoc test.

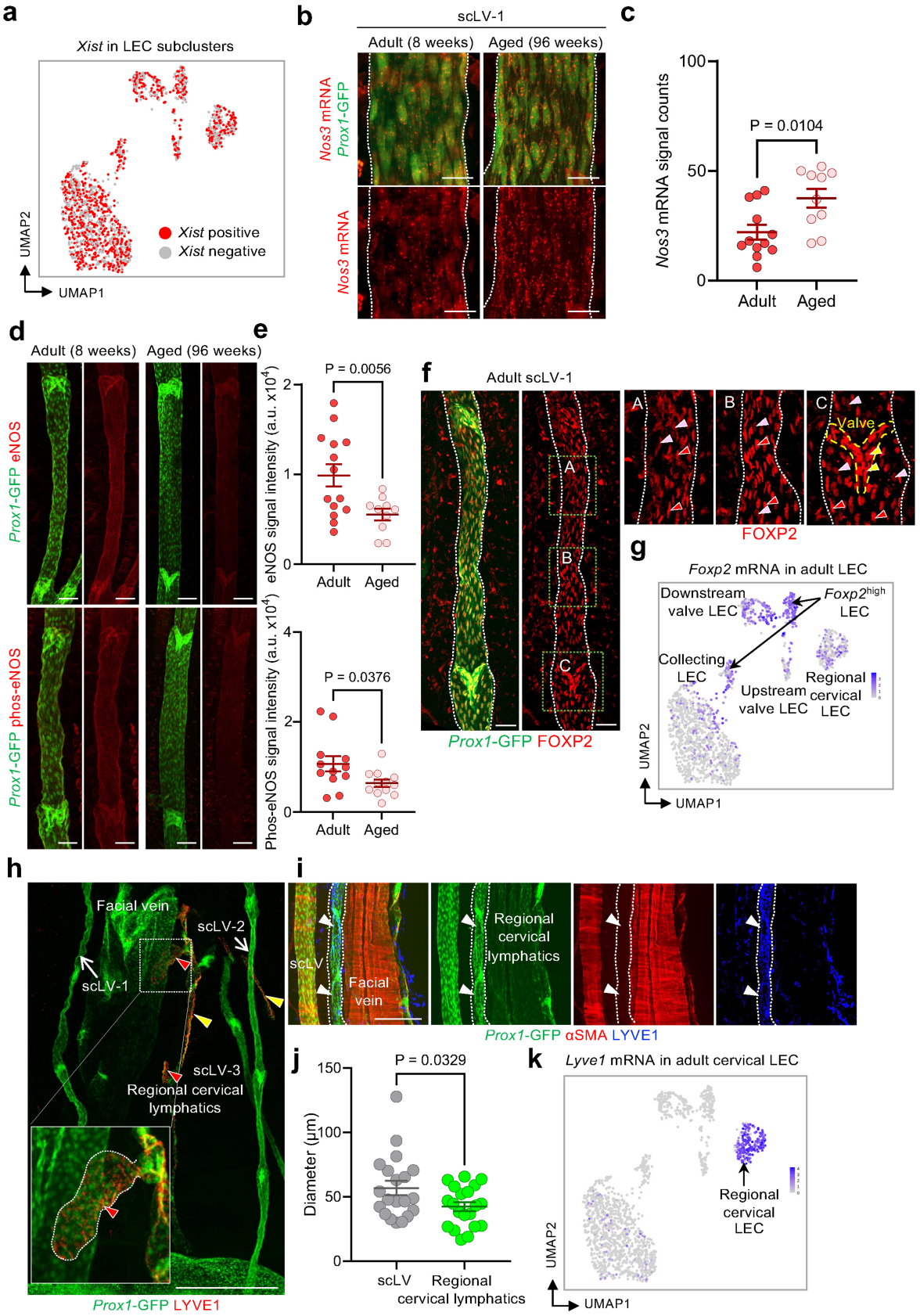


**Extended Data Fig. 11** | See next page for caption.

**Extended Data Fig. 11 | Validation of scRNA-seq data with RNA *in-situ* hybridization and immunohistochemical staining of LEC clusters.** **a**, Uniform manifold approximation and projection (UMAP) plot showing expression of *Xist*, a female-specific non-coding RNA, in LEC clusters from 3 male and 3 female *Prox1*-GFP mice shown in Extended Data Fig. 10a. Equal distributions of *Xist* positive and *Xist* negative cells are consistent with the sample being representative. **b,c**, Representative RNA *in-situ* hybridization images and signal counts comparing *Nos3* mRNA expression in superficial cervical lymphatics scLV-1 (white dashed lines) in whole mounts from adult (8 weeks) and aged (96 weeks) *Prox1*-GFP mice. Scale bars, 20 μm. In **c**, each dot is the value for one side of scLV-1 from one mouse. $n = 6$ mice (adult) and $n = 5$ mice (aged) from three independent experiments. Error bars indicate mean ± s.e.m. *P* values calculated by two-tailed Welch's t-test. **d,e**, Confocal microscopic images and measurements of immunofluorescence staining for eNOS and phosphorylated-eNOS (phos-eNOS) in superficial cervical lymphatics scLV-1 in tissue whole mounts from adult (8 weeks) and aged (96 weeks) *Prox1*-GFP mice. Scale bars, 100 μm. Each dot is the value for one side of scLV-1 from one mouse. $n = 7$ (adult, eNOS), $n = 6$ (adult, Phos-eNOS) mice and $n = 5$ (aged, eNOS), $n = 6$ (aged, Phos-eNOS) mice from three independent experiments. Error bars indicate mean ± s.e.m. *P* values calculated by two-tailed Welch's t-test. **f,g**, Confocal microscopic images of immunofluorescence staining (**f**) and uniform manifold approximation and projection (UMAP) plot (**g**) of FOXP2 expression in superficial cervical lymphatics scLV-1 (white dashed lines) in tissue whole mounts from adult (8 weeks) *Prox1*-GFP mice. Green dashed line boxes in **f** mark regions enlarged in the right three panels. Diverse features of FOXP2 expression in LEC are marked by colored arrowheads: red (*Foxp2*$^{high}$ LEC), pink (*Foxp2*$^{low}$ LEC), and yellow (*Foxp2*$^{high}$ LEC in valve). Scale bars, 50 μm. Representative of $n = 3$ mice from three independent experiments. FOXP2 immunofluorescence was variably strong in luminal LEC but consistently strong in valve LEC (**f**), which fits with the UMAP plot that shows two separate *Foxp2*$^{high}$ LEC clusters (**g**). **h-k**, Immunofluorescence images of whole mounts showing staining for *Prox1*-GFP and LYVE1 in initial lymphatics (with blunt ends, red arrowheads) and pre-collecting lymphatics (with valves, yellow arrowheads) of regional cervical lymphatics (**h**). White dashed line box marks the region enlarged in the left lower corner. Scale bar, 500 μm. Representative of $n = 3$ mice from three independent experiments. Immunofluorescence images of whole mounts showing *Prox1*-GFP in all lymphatics but not in a facial vein; αSMA staining of smooth muscle in a collecting lymphatic and facial vein but not in a pre-collecting lymphatic; and LYVE1 staining in a pre-collecting lymphatic (white arrowheads and dashed line outline) but not in the other vessels (**i**). Scale bar, 200 μm. Representative of $n = 3$ mice from three independent experiments. Dot plot graph showing superficial cervical collecting lymphatics that are larger in diameter than pre-collecting lymphatics in adult *Prox1*-GFP mice (**j**). Each dot is the value for one lymphangion from one side of cervical lymphatics. $n = 6$ mice from three independent experiments. Error bars indicate mean ± s.e.m. a.u., arbitrary unit. *P* values calculated by two-tailed Welch's t-test. The immunofluorescence staining (**h,i**) fits with the strong *Lyve1* mRNA expression restricted to the regional cervical (initial and pre-collecting) LEC cluster in the uniform manifold approximation and projection (UMAP) plot (**k**).

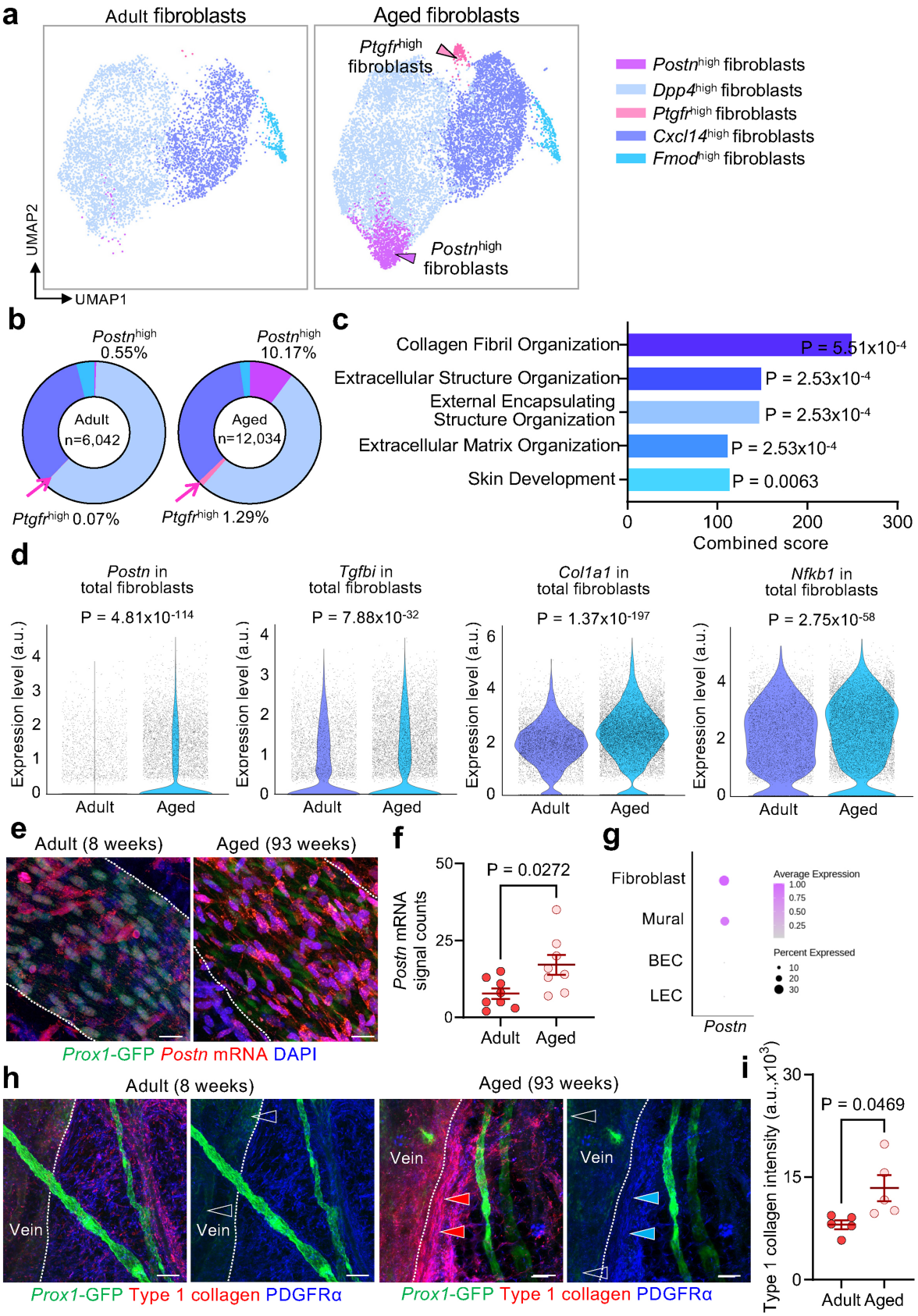


**Extended Data Fig. 12** | See next page for caption.

**Extended Data Fig. 12 | Differential effects of ageing on gene expression in five fibroblast subclusters associated with superficial cervical lymphatics.** **a**, Uniform manifold approximation and projection (UMAP) plots of single-cell gene expression (scRNA-seq) analysis identified five subclusters of fibroblasts in tissues around superficial cervical lymphatics from six adult (12 weeks) and six aged (93 weeks) *Prox1*-GFP mice. Arrowheads in plot of fibroblasts from aged mice mark subclusters that were rare in younger adult mice: magenta arrowhead marks the *Postn*$^{high}$ fibroblast subcluster, and pink arrowhead marks the *Ptgfr*$^{high}$ fibroblast subcluster. The total number of fibroblasts analyzed is 6,042 in adult mice and 12,034 in aged mice. **b**, Pie charts of the five fibroblast subclusters showing that *Postn*$^{high}$ (magenta) and *Ptgfr*$^{high}$ (pink) fibroblasts around superficial cervical lymphatics of aged mice were both 18 times the corresponding proportion in younger adults, but the other three fibroblast subclusters were similarly abundant at both ages. **c**, Gene ontology analysis of gene expression of fibroblasts around superior cervical lymphatics showing five gene ontology terms related to fibrosis that were significantly enriched in aged mice: collagen fibril organization, extracellular structure organization, external encapsulating structure organization, extracellular matrix organization, skin development. GO enrichment was assessed using Enrichr. *P* values calculated using one-tailed Fisher's exact test, with FDR correction using the Benjamini-Hochberg method. Complete dataset for the GO term analysis is presented in Supplementary Table 3. **d**, Violin plots showing four examples of fibrosis- or inflammation-related genes in fibroblasts around superficial cervical lymphatics that had significantly greater expression in aged mice than in younger adults: *Postn* (periostin, osteoblast-specific factor 2), *Tgfbi* (transforming growth factor, beta-induced), *Col1a1* (skin, tendon, bone collagen, type I, alpha-1 chain), and *Nfkb1* (nuclear factor kappa-B, subunit 1). *P* values calculated by two-tailed MAST with Bonferroni post hoc test. **e-g**, Images comparing RNA *in-situ* hybridization of *Postn* mRNA expression in whole mounts of superficial cervical lymphatics (white dashed lines) in *Prox1*-GFP mice at age 8 weeks and 93 weeks and corresponding measurements (**e,f**). In the younger adult specimen, *Prox1*-GFP nuclei (green) are prominent, but in the aged adult specimen, fibroblasts with strong expression of *postn* mRNA (magenta) and DAPI-stained (blue) nuclei are distributed around the superficial cervical lymphatics (**e**). Scale bars, 20 μm. The dot plot (**g**) shows the relative expression levels of *postn* mRNA in fibroblasts, mural cells, and endothelial cells of blood vessels (BEC) and lymphatics (LEC), based on scRNA-seq data in Supplementary Fig. 14. Each dot (**f**) is the value for one scLV from $n = 4$ mice (younger adult) and $n = 4$ mice (aged) examined in three independent experiments. Error bars indicate mean ± s.e.m. *P* values calculated by two-tailed Welch's t-test. **h,i**, Type 1 collagen immunofluorescence around the superficial cervical lymphatics and adjacent vein in whole mounts from adult (8 weeks) and aged (93 weeks) *Prox1*-GFP mice and corresponding measurements. Type 1 collagen staining (red arrowheads) is strongest in fibroblasts near the vein in the aged mouse but is less near the lymphatics and elsewhere (**h**). Veins (left of white dashed lines) are distinguished by the weak signal (blank arrowheads) of *Prox1*-GFP fluorescence. PDGFRα$^{+}$ fibroblasts (blue). Scale bars, 100 μm. Measurements document greater type 1 collagen staining in the aged mice (**i**). Each dot is the value for one scLV. $n = 5$ mice (adult) and $n = 5$ mice (aged) from three independent experiments. Error bars indicate mean ± s.e.m. *P* values calculated by two-tailed Welch's t-test.

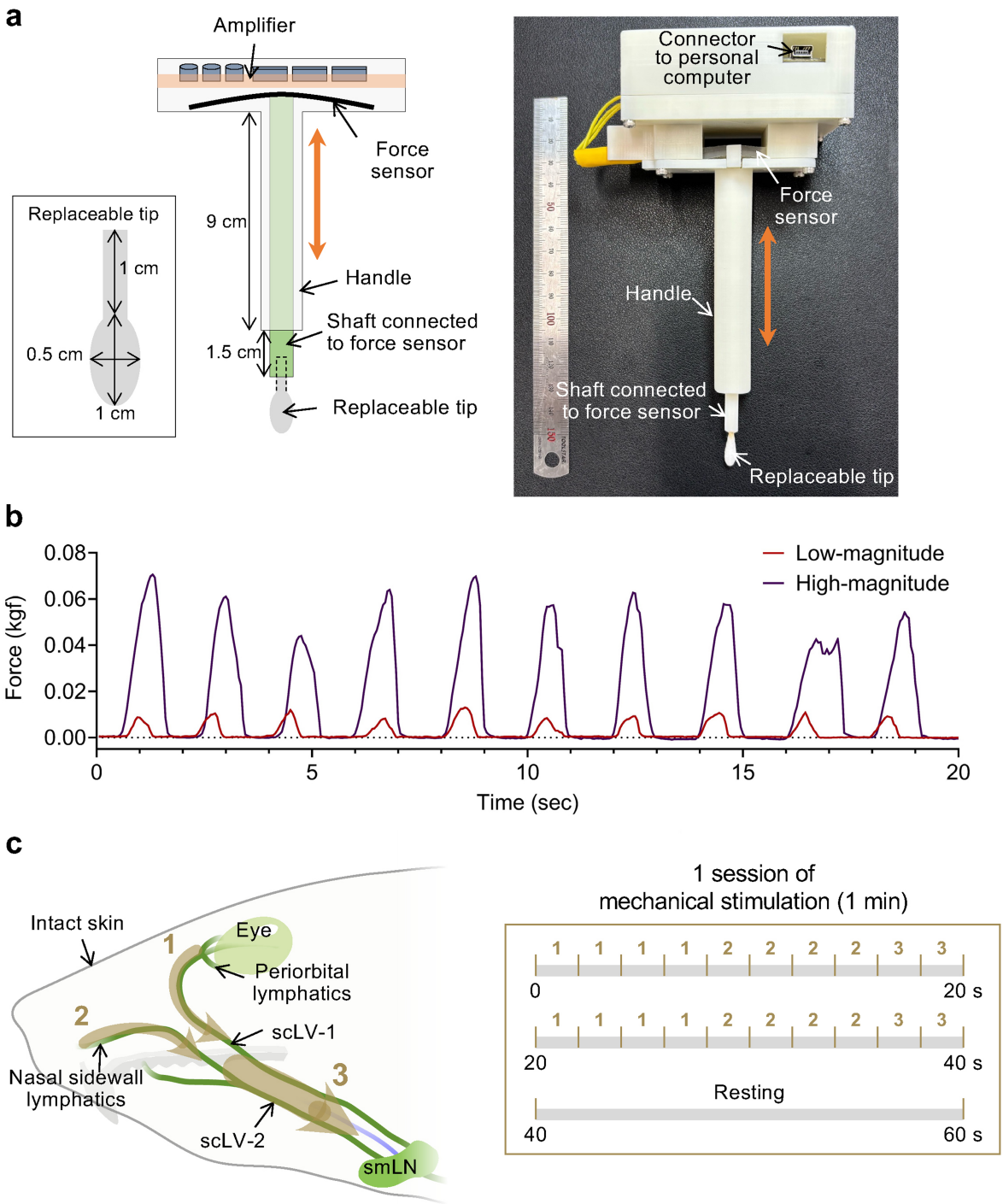


**Extended Data Fig. 13 | Features and use of mechanical stimulator for increasing CSF drainage through superficial cervical lymphatics. a**, Drawing and photograph of the precision force-regulated mechano-stimulator consisting of an amplifier, force sensor, handle, shaft connecting the tip to the force sensor, and replaceable tip. The replaceable tip was an oval-shaped cotton ball, with a major axis of 1 cm and minor axis of 0.5 cm, that was attached to a 1-cm long rod securely connected to the shaft. The length of the handle was 9 cm. The force sensor made of silicone and conductive fabric was connected to the replaceable tip through the shaft. The measured force was transmitted to an amplifier connected to a personal computer. **b**, Graphs comparing low-magnitude (0.01-0.02 kgf) and high-magnitude (0.04-0.08 kgf) forces generated by the mechanical stimulator every 2 s over 20 s. **c**, Drawing (left) showing the three stimulation paths (numbered brown dashed arrows) in three regions of intact skin of mice along the course of superficial cervical lymphatics scLV-1 and scLV-2 to promote CSF flow toward the submandibular lymph node (smLN). Region 1 was from the periorbital area to the mandible. Region 2 was from the nasal sidewall to the mandible. Region 3 was along the paths of scLV-1 and scLV-2 to the submandibular lymph node. Each 1-min session of mechanical stimulation consisted of two sequences of 10 two-second strokes each, with a 20-sec rest period after the two sequences. Each sequence included four two-second strokes in Region 1, four in Region 2, and two in Region 3 (right).

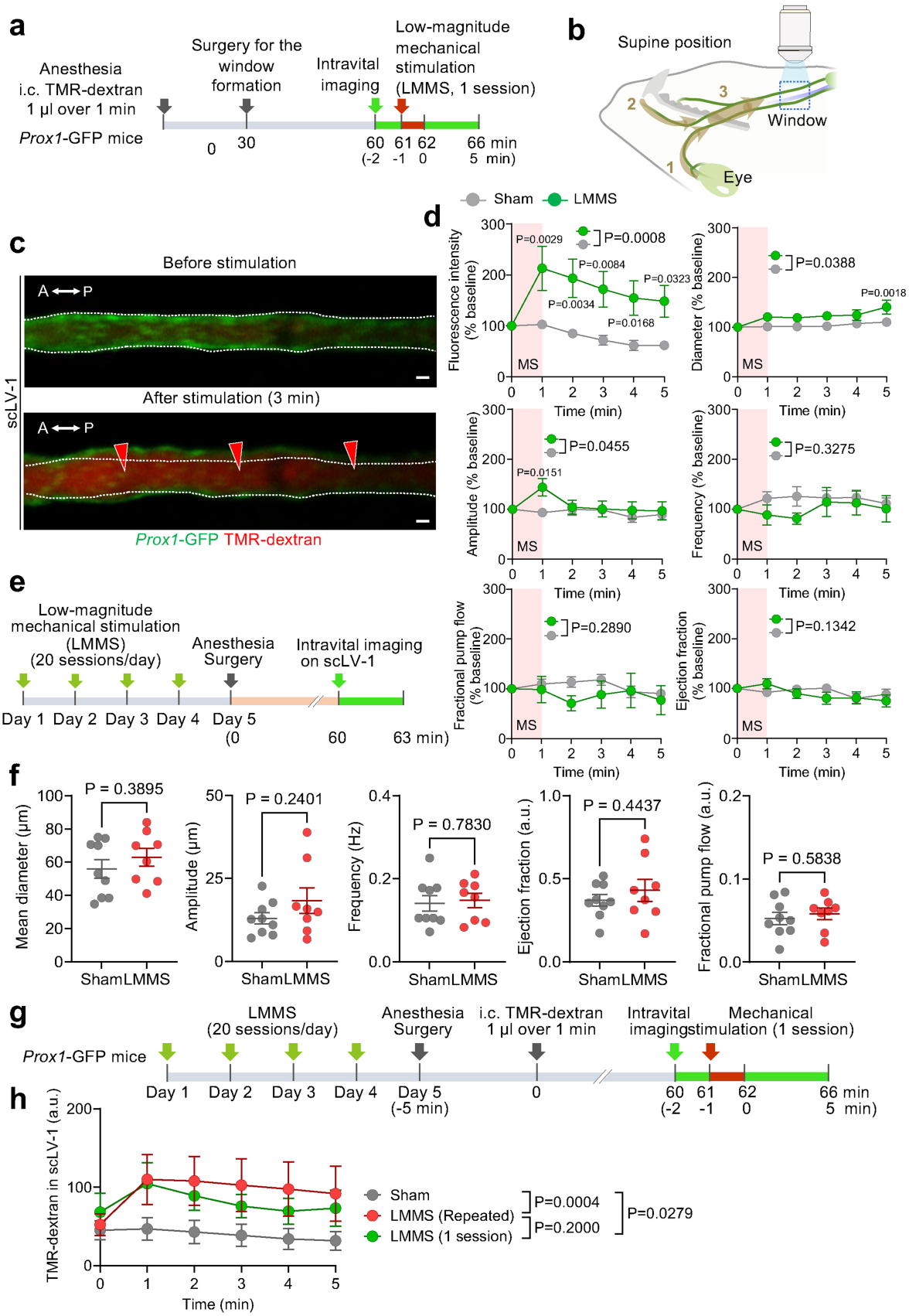


**Extended Data Fig. 14** | See next page for caption.

**Extended Data Fig. 14 | Low-magnitude mechanical stimulation increases CSF outflow through superficial cervical lymphatics with sustained efficacy after 4 daily sessions. a**, Sequence of surgical exposure of superficial cervical lymphatics scLV-1 in *Prox1*-GFP mice, a 20-min stabilization period, and intravital imaging during and 5 min after 1-min of low-magnitude mechanical stimulation (LMMS) of the face and neck as in Extended Data Fig. 13. Measurements were made at 1-min intervals for 5 min after stimulation. **b**, Drawing showing the relative locations of region 3 of LMMS of scLV-1 and scLV-2 and the downstream window for intravital imaging (blue dashed box). **c**, Intravital images of scLV-1 of *Prox1*-GFP mouse downstream before and after one session of LMMS. White dashed lines outline the vessel border before LMMS. Red arrowheads mark regions of TMR-dextran fluorescence. Scale bars, 20 μm. Anatomical positions are indicated in the top left corner: A, anterior; P, posterior. **d**, Measurements of temporal changes in TMR-dextran fluorescence, as an index of CSF outflow, and five parameters of spontaneous contraction of scLV-1 at the onset and 1-5 min after a 1-min session of LMMS (MS). At 1-min, TMR-dextran values are more than double the onset and continue to be significantly greater throughout the 5-min monitoring period. Other values show a small increase in scLV-1 mean diameter and transient increase in amplitude of spontaneous contractions but no significant change in ejection fraction, contraction frequency, or fractional pump flow. All values are expressed as % of mean baseline fluorescence before LMMS. Each dot is the mean value for $n = 9$ (sham), $n = 7$ (LMMS) mice of both sexes from three independent experiments. Error bars indicate s.e.m. *P* values calculated by two-way repeated-measures ANOVA followed by Sidak's multiple comparison test. **e**, Sequence of repeated low-magnitude mechanical stimulation (LMMS, 20 sessions/day) for 4 days followed on day 5 by surgical exposure and intravital imaging of superficial cervical lymphatic scLV-1 in adult (8–12 weeks) *Prox1*-GFP mice. Intravital imaging began after a 30-min stabilization period and lasted 3 min. **f**, Measurements show no difference between the sham and stimulated group in values for mean diameter, spontaneous contraction amplitude, ejection fraction, frequency, or fractional pump flow in scLV-1. Each dot is the value for one mouse. $n = 9$ (sham), $n = 8$ (LMMS) mice per group in three independent experiments. Error bars indicate mean ± s.e.m. a.u., arbitrary unit. Intravital imaging values were averaged over 3 min for each mouse. *P* values calculated by two-tailed Welch's t test. **g**, Sequence of repeated LMMS (20 sessions/day) for 4 days followed by surgical exposure, intracisternal infusion of TMR-dextran, intravital imaging of scLV-1, low-magnitude mechanical stimulation (1 session) in adult *Prox1*-GFP mice, and measurement of TMR-dextran fluorescence in scLV-1 within the imaging window. Intravital imaging began after a 30-min stabilization period and lasted 5 min after LMMS (1 session) or sham. **h**, Comparison of three conditions showing significantly greater TMR-dextran fluorescence in scLV-1 in the repeated stimulation group than in the sham group. The magnitude of TMR-dextran fluorescence in the scLV-1 after repeated stimulation over 4 days did not differ from corresponding values after one stimulation session (data from Extended Data Fig. 14d). Each dot is the value for $n = 9$ (sham), $n = 7$ (1 session LMMS or repeated LMMS) mice of both sexes from three independent experiments. Error bars indicate mean ± s.e.m. a.u., arbitrary unit. *P* values calculated by two-way repeated-measures ANOVA.

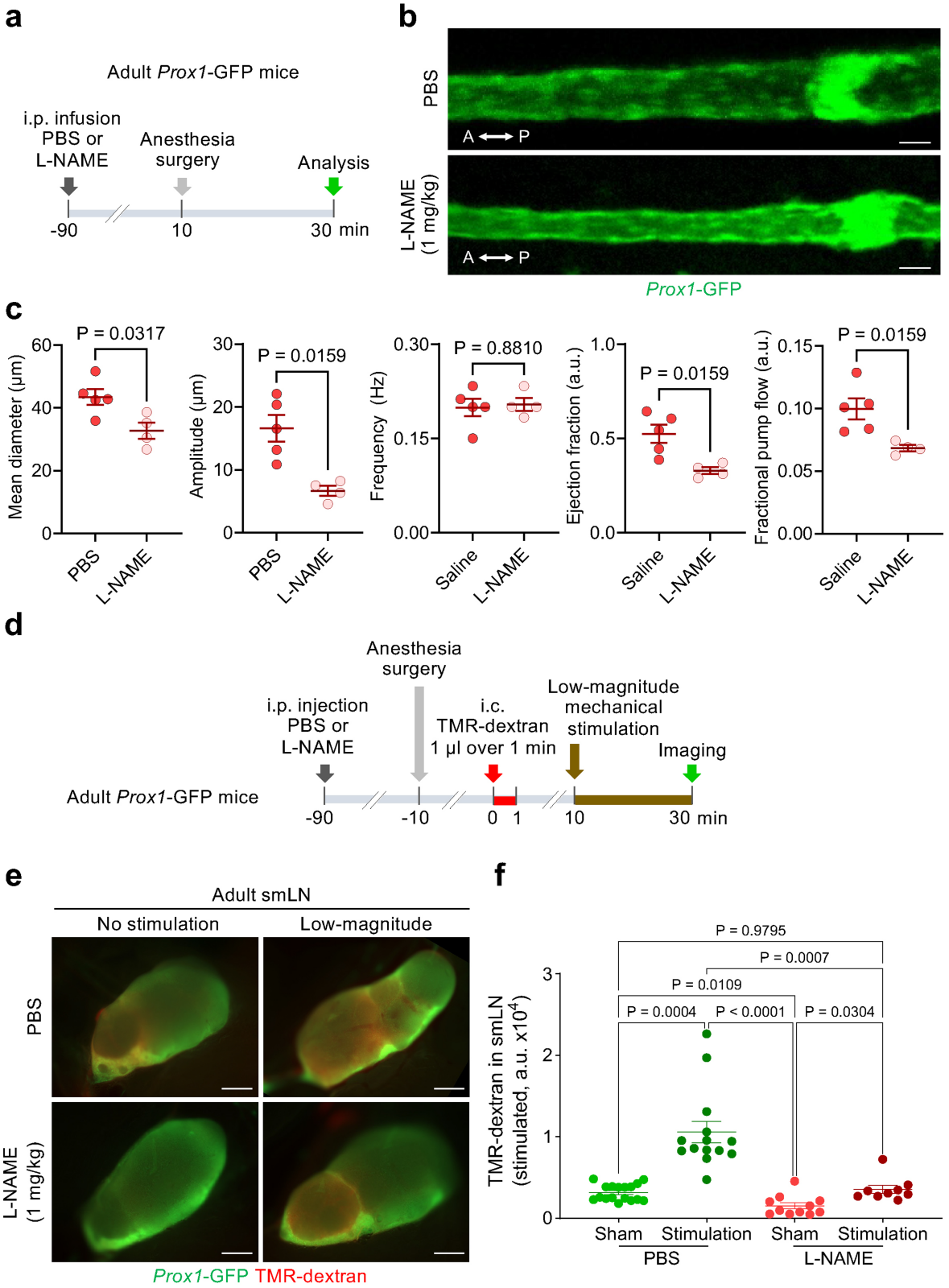


**Extended Data Fig. 15** | See next page for caption.

**Extended Data Fig. 15 | Nitric oxide signaling contribution to increased CSF drainage by mechanical stimulation. a**, Sequence of intraperitoneal (i.p.) injection of PBS or L-NAME (1 mg/kg body weight) followed 120 min later by intravital imaging and measurements of superficial cervical lymphatic vessel scLV-1 of *Prox1*-GFP mice (8–12 weeks old). **b**, Intravital image showing scLV-1 of *Prox1*-GFP mouse at 120 min after treatment with PBS or L-NAME. Basal tone (smaller diameter) was greater after L-NAME. Scale bars, 30 µm. A, anterior; P, posterior anatomical position. Representative of $n = 4$-5 mice from three independent experiments. **c**, Comparison of effect of PBS or L-NAME on scLV-1 mean diameter, amplitude, frequency, ejection fraction, and fractional pump flow. Each dot is the value for one mouse. $n = 5$ (PBS), $n = 4$ (L-NAME) mice of both sexes per group from three independent experiments. Error bars indicate mean ± s.e.m. a.u., arbitrary unit. *P* values calculated by two-tailed Mann-Whitney *U*-test. **d**, Sequence of PBS or L-NAME injected intraperitoneally (i.p.) followed 90 min later by intracisternal (i.c.) infusion of 1.0 µl TMR-dextran over 1 min into adult *Prox1*-GFP mice followed by measurement of TMR-dextran fluorescence in the submandibular lymph node 30 min later. Low-magnitude mechanical stimulation was applied for 20 min beginning 10 min after the intracisternal infusion. **e**,**f**, Fluorescence images and measurements of TMR-dextran fluorescence in the submandibular lymph node 30 min after the intracisternal infusion and mechanical stimulation shown in **d**. Scale bars, 500 µm. Fluorescence in lymph node of PBS controls compared to L-NAME treatment without stimulation (sham) or after 20 low-magnitude stimulation sessions over 20 min beginning 10 min after TMR-dextran infusion. Each dot is the value for one mouse. $n = 17$ (PBS, sham), $n = 14$ (PBS, stimulated), $n = 11$ (L-NAME, sham), $n = 9$ (L-NAME, stimulated) mice per group from four independent experiments. Error bars indicate mean ± s.e.m. a.u., arbitrary unit. *P* values calculated by Brown-Forsythe ANOVA test followed by Dunnett's T3 multiple comparison test.

nature portfolio

Corresponding author(s): Gou Young Koh

Last updated by author(s): Apr 14, 2025

# Reporting Summary

Nature Portfolio wishes to improve the reproducibility of the work that we publish. This form provides structure for consistency and transparency in reporting. For further information on Nature Portfolio policies, see our Editorial Policies and the Editorial Policy Checklist.

## Statistics

For all statistical analyses, confirm that the following items are present in the figure legend, table legend, main text, or Methods section.

| n/a | Confirmed |
|---|---|
| ☐ | ☒ The exact sample size (*n*) for each experimental group/condition, given as a discrete number and unit of measurement |
| ☐ | ☒ A statement on whether measurements were taken from distinct samples or whether the same sample was measured repeatedly |
| ☐ | ☒ The statistical test(s) used AND whether they are one- or two-sided<br>*Only common tests should be described solely by name; describe more complex techniques in the Methods section.* |
| ☐ | ☒ A description of all covariates tested |
| ☐ | ☒ A description of any assumptions or corrections, such as tests of normality and adjustment for multiple comparisons |
| ☐ | ☒ A full description of the statistical parameters including central tendency (e.g. means) or other basic estimates (e.g. regression coefficient) AND variation (e.g. standard deviation) or associated estimates of uncertainty (e.g. confidence intervals) |
| ☐ | ☒ For null hypothesis testing, the test statistic (e.g. *F*, *t*, *r*) with confidence intervals, effect sizes, degrees of freedom and *P* value noted<br>*Give P values as exact values whenever suitable.* |
| ☒ | ☐ For Bayesian analysis, information on the choice of priors and Markov chain Monte Carlo settings |
| ☒ | ☐ For hierarchical and complex designs, identification of the appropriate level for tests and full reporting of outcomes |
| ☒ | ☐ Estimates of effect sizes (e.g. Cohen's *d*, Pearson's *r*), indicating how they were calculated |

*Our web collection on statistics for biologists contains articles on many of the points above.*

## Software and code

Policy information about availability of computer code

| | |
|---|---|
| Data collection | The following softwares were used for data collection:<br>ZEN 2.1 SP3 (black) ver.14.0.4.201 (Carl Zeiss) - LSM 880<br>ZEN 2.3 (blue) ver 2.3.69.1010 (Carl Zeiss) - LSM 800<br>ZEN 2.3 (blue) ver 2.3.64.0 (Carl Zeiss) - AxioZoom V16<br>Labview ver 2017 (National Instruments Inc.)<br>IVIM Engine 3.10.10 (IVIM) - IVIM-CM3 |
| Data analysis | The following softwares were used for data analysis:<br>ZEN 2.1 SP3 (black) ver.14.0.4.201 (Carl Zeiss) - LSM 880<br>ZEN 2.3 (blue) ver 2.3.69.1010 (Carl Zeiss) - LSM 800<br>ZEN 2.3 (blue) ver 2.3.64.0 (Carl Zeiss) - AxioZoom V16<br>ImageJ software 1.54g (NIH)<br>MATLAB (R2023b, MathWorks)<br>Graphpad Prism10 (GraphPad Software, version 10.2.3)<br>Cell Ranger (version 8.0.1)<br>R: The R Project for Statistical Computing<br>R: package 'Seurat' (version 5.0.3)<br><br>Code availability: The source codes for the current study are available at Zenodo (https://doi.org/10.5281/zenodo.15172410) |

For manuscripts utilizing custom algorithms or software that are central to the research but not yet described in published literature, software must be made available to editors and reviewers. We strongly encourage code deposition in a community repository (e.g. GitHub). See the Nature Portfolio guidelines for submitting code & software for further information.

## Data

Policy information about availability of data

All manuscripts must include a data availability statement. This statement should provide the following information, where applicable:

- Accession codes, unique identifiers, or web links for publicly available datasets
- A description of any restrictions on data availability
- For clinical datasets or third party data, please ensure that the statement adheres to our policy

The scRNA-seq data of this study are available in the NCBI's Gene Expression Omnibus under accession GSM8493731 (adult mice) and GSM8493732 (aged mice). All other data supporting the findings in this study are available within the paper and its Supplementary Information. Source data are provided with this paper.

## Research involving human participants, their data, or biological material

Policy information about studies with human participants or human data. See also policy information about sex, gender (identity/presentation), and sexual orientation and race, ethnicity and racism.

| | |
|---|---|
| Reporting on sex and gender | Not applicable |
| Reporting on race, ethnicity, or other socially relevant groupings | Not applicable |
| Population characteristics | Not applicable |
| Recruitment | Not applicable |
| Ethics oversight | Not applicable |

Note that full information on the approval of the study protocol must also be provided in the manuscript.

# Field-specific reporting

Please select the one below that is the best fit for your research. If you are not sure, read the appropriate sections before making your selection.

☒ Life sciences ☐ Behavioural & social sciences ☐ Ecological, evolutionary & environmental sciences

For a reference copy of the document with all sections, see nature.com/documents/nr-reporting-summary-flat.pdf

# Life sciences study design

All studies must disclose on these points even when the disclosure is negative.

| | |
|---|---|
| Sample size | Sample size were chosen on the basis of standard power (with α = 0.05 and power of 0.8) performed for similar experiments and no statistical methods were used to predetermine sample size as previously published (Ahn et al., Nature (2019); Yoon et al., Nature (2024)). |
| Data exclusions | No samples were excluded from the analysis. |
| Replication | Experiments were replicated at least once for all analyses and number of reproductions of each experimental findings is described in each figure legend. All attempts at experimental replication were successful. |
| Randomization | Mice were housed in groups of up to 5 per cage, with random assignment to experimental groups. To ensure randomization, we selected animals from different cages within the same experimental group. All experimental variables were controlled, eliminating potential covariates. |
| Blinding | The investigators were blinded during the experiments and quantifications. |

# Reporting for specific materials, systems and methods

We require information from authors about some types of materials, experimental systems and methods used in many studies. Here, indicate whether each material, system or method listed is relevant to your study. If you are not sure if a list item applies to your research, read the appropriate section before selecting a response.

## Materials & experimental systems

| n/a | Involved in the study |
|---|---|
| ☐ | ☒ Antibodies |
| ☒ | ☐ Eukaryotic cell lines |
| ☒ | ☐ Palaeontology and archaeology |
| ☐ | ☒ Animals and other organisms |
| ☒ | ☐ Clinical data |
| ☒ | ☐ Dual use research of concern |
| ☒ | ☐ Plants |

## Methods

| n/a | Involved in the study |
|---|---|
| ☒ | ☐ ChIP-seq |
| ☒ | ☐ Flow cytometry |
| ☒ | ☐ MRI-based neuroimaging |

# Antibodies

Antibodies used

Primary antibodies used were: anti-mouse LYVE1 (rabbit polyclonal, 11-034, Angiobio); anti-mouse VEGFR3 (goat polyclonal, AF743, R&D Systems); anti-mouse αSMA-Cy3 (mouse monoclonal, clone 1A4, C6198, Sigma); anti-mouse laminin α5 (rabbit polyclonal, EWL004, kerafast); anti-mouse CD31 (hamster monoclonal, clone 2H8, MAB1398Z, Merck); anti-mouse tyrosine hydroxylase (rabbit polyclonal, AB152, Merck); anti-mouse vesicular acetylcholine transporter (VAChT, also known as solute carrier family 18 (vesicular acetylcholine), member 3, Slc18a3, goat polyclonal, ABN100, Merck); anti-monkey LYVE1 (rabbit polyclonal, DP3500, OriGene); anti-mouse eNOS antibody (rabbit polyclonal, ab5589, Abcam); anti-mouse phospho-eNOS antibody (rabbit polyclonal, 9571, Cell Signaling); anti-mouse FOXP2 antibody (goat polyclonal, ab1307, Abcam); anti-mouse ER-TR7 antibody (rat monoclonal, clone ER-TR7, sc-73355, Santa Cruz Biotechnology); anti-mouse Col1a1 (rabbit monoclonal, clone E8F4L, 72026, Cell Signaling); anti-mouse PDGFRα (goat polyclonal, AF1062, R&D Systems); anti-mouse CD45 antibody (Rat monoclonal, clone 30-F11, 103147, BioLegend) and DAPI (564907, Sigma-Aldrich).

The following secondary antibodies were used: Alexa Fluor™ 488-, 594- and 647- conjugated anti-rabbit (711-545-152, 711-585-152, 711-605-152), anti-goat (705-585-147), anti-hamster (127-605-160), anti-rat (712-605-153) secondary antibodies (Jackson ImmunoResearch). Nuclei were stained with DAPI (H-1200, Vector).

Primary antibodies were diluted at 1:200 (for immunostaining of cleared sample and cell sorting) or 1:400 (for immunostaining) and secondary antibodies were diluted at 1:1000 for all the immunostainings or lymphatic endothelial cell sorting.

Validation

All the antibodies were validated for the species (mouse or monkey) and applications (immunostaining or cell sorting) by the correspondent manufacturer, which is described in the manufacturer's website. Furthermore, all antibodies were assessed in similar experiments published previously (Ahn et al., Nature (2019); Yoon et al., Nature (2024)). Complete details regarding antibody usage are provided within the manuscript.

# Animals and other research organisms

Policy information about studies involving animals; ARRIVE guidelines recommended for reporting animal research, and Sex and Gender in Research

Laboratory animals

Prox1-GFP mice (FVB background, 8 to 12-week-old for adult, 80 to 105 week-old for aged, Choi et al., Blood, 2011; provided by Dr. Young-Kwon Hong, University of Southern California) were transferred, established, and bred in SPF animal facilities at KAIST under a 12 h-12 h light-dark cycle at 23-24 °C and 40-60 % humidity. Adult (8 to 12-week-old) and aged (80 to 95-week-old) C57BL/6J mice were purchased from JAX (USA) or the Animal Center of Aging Science of Korea Basic Science Istitute. The head and neck portions of the primate (Macaca fascicularis, 7-14 years old) were obtained from the National Primate Center of KRIBB.

Wild animals

The study did not involve wild animals.

Reporting on sex

In this study, we randomized both genders were selected and used because gender was not a major criteria serve the purpose of this study.

Field-collected samples

The study did not involve samples collected from the field.

Ethics oversight

All animal care and experimental procedures were approved by Institutional Animal Care and Use Committees of the Korea Advanced Institute of Science and Technology (KAIST) (KA2024-122-v1) and the University of Missouri (9797) for the mice and the Korea Research Institute of Bioscience and Biotechnology (KRIBB-AEC-24079) for the primates.

Note that full information on the approval of the study protocol must also be provided in the manuscript.